NUMERICAL MODELLING OF MULTIPHASE DIESEL FUEL PROPERTIES USING THE PC-SAFT EQUATION OF STATE AND ITS EFFECT ON NOZZLE FLOW AND CAVITATION UNDER EXTREME PRESSURISATION

Thesis submitted for the fulfilment of the requirements for the Degree of Doctor of Philosophy

by

Alvaro Vidal Roncero

CITY
UNIVERSITY OF LONDON
EST 1894

School of Mathematics, Computer Science & Engineering City, University of London
July, 2020

To all my bedrocks

Abstract

The present work investigates the influence of properties variation of Diesel fuel in the range of injection pressures from 60MPa to 450MPa on nozzle flow and cavitation. The PC-SAFT equation of state is utilised to derive physical property predictions of a grade no.2 Diesel emissions-certification fuel. Four candidate multicomponent Diesel surrogates are modelled. Density, viscosity and volatility predictions are compared to experimental data from several other Diesel fuels and against Peng Robinson. PC-SAFT calculations are performed using different sources for the pure component parameters, namely LC and GC methods. An eight-component surrogate yields the best match for Diesel properties with a combined mean absolute deviation of 7.1% from experimental data found in the literature for conditions up to 373 K and 500 MPa. The vapour-liquid equilibrium of this surrogate is then calculated with a novel algorithm, which uses as independent variables the mixture composition, density and temperature. This algorithm is based on unconstrained minimisation of the Helmholtz Free energy via a combination of the successive substitution iteration and Newton-Raphson minimisation. The reliability of two different methods presented in the existing literature is assessed for 7 different cases. The properties of the eight-component surrogate are derived and put onto tables to be used in simulations. These simulations are performed on a tapered heavy-duty Diesel engine injector at a nominal fully-open needle valve lift of 350μm. Two approaches have been followed: (i) a barotropic evolution and (ii) the inclusion of wall friction-induced thermal effects. Results indicate a significant increase in the mean vapour pressure of the fuel and an unprecedented decrease of cavitation volume inside the fuel injector with increasing injection pressure. This has been attributed to the shift of the pressure drop from the feed to the back pressure inside the injection hole orifice as fuel discharges. The study links friction-induced thermal effects to the preferential cavitation of the fuel components. Lighter fuel components are found to cavitate to a greater extent than heavier ones, independently of the initial fuel composition. Moreover, the final vapour cloud composition was found to differ with injection pressure, as the components within vaporise at their respective rhythm according to their molecular structure and global pressure/temperature conditions.

Present contribution

The novelty of the thesis can be summarised in the following points:

- **Modelling of Diesel fuel with complex thermodynamic and thermophysical models**

The properties of Diesel surrogates are modelled using the state-of-the-art PC-SAFT EoS, which only needs 3 parameters per non-associating component. Parameters not found in the literature were estimated with correlations and group contribution methods. The predictions for density, viscosity and volatility are validated against experiments and compared with the widely used Peng Robinson EoS. Results allowed to show the high accuracy of PC-SAFT predicting a complex multicomponent mixture such as Diesel and its superiority against simpler cubic equations of state.

- **Predicting vapour-liquid equilibrium using temperature, density and composition as inputs**

Pressure and temperature have been widely used as inputs for VLE calculations, for which PC-SAFT algorithms exist. However, these algorithms fail if the phase change occurs at constant pressure and temperature. This is the case for the Diesel surrogates at certain conditions. Thus, in this work an algorithm using density, temperature and composition for VLE calculations is coupled with PC-SAFT for the first time.

- **In nozzle flow and cavitation simulations at extreme pressure injections**

In nozzle flow simulations are performed at injection pressures up to 450MPa for the first time. For these simulations, an 8-component Diesel surrogate is accurately modelled with the PC-SAFT EoS, making use of the developed VLE algorithm to predict its vaporisation. As thermal conductivity and heat capacity are modelled with PC-SAFT as well, the heating and cooling of the fuel can be properly predicted, as well as the effect on the flow from significant changes in viscosity due to extreme pressurisation.

- **Preferential vaporisation**

During the in-nozzle simulations, flow separation appears at the orifice entrance due to great velocities developing and geometry changes, decreasing the pressure. As a result, the fuel cavitates and, with it, the components found therein. Thus, the composition of the vapour cloud can be calculated thank to the VLE algorithm.

- **Major findings**
    - In-nozzle cavitation volume fraction decreases with the injection pressure, at extreme injection pressures.
    - The composition of the fuel vapour shows that the lighter components are found vaporised in a significantly greater amount than the heavy ones.
    - Vapour mass flow rate and the net evaporation and condensation per meter of the orifice length increase with the injection pressure.
    - The results obtained by the PC-SAFT EoS to model Diesel shows the highest degree of agreement with experimental values in comparison with the results obtained applying the method developed at NIST and with Peng Robinson.
    - PC-SAFT is shown to be significantly slower than Peng Robinson during VLE calculations. This difference in computational time grows with the number of components.

Acknowledgements

Firstly, I would like to thank Prof. Manolis Gavaises and Dr. Phoevos Koukouvinis for their continuous advice and help throughout this project. Also, Prof. McHugh for his inspiring comments during my first publication in the group. Thanks to Dr. Lorenzo Botto, who made choose this path and showed me the wonders of research.

Nothing would be done without my colleagues in the group, I owe them my day-by-day motivation and overall happiness. I would also like to thank my colleagues in the IPPAD project for their wonderful company and interesting and funny conversations.

Thanks to my old and new friends, who would always ask “so you haven’t stopped studying yet?”, their support and encouragement was paramount.

Finally, thanks to my family who always were there for me and helped me in the best way possible.

This project has received funding from the European Union Horizon-2020 Research and Innovation Programme with grant Agreement No 675528.

London, September 2020

Álvaro Vidal Roncero

Declaration

I hereby declare that the content of this dissertation is original and has not been submitted in whole or in part for consideration for any other degree or qualification in this, or any other university. This dissertation is my own work, except where specific reference is made to a joint effort in the text and acknowledged accordingly. I grant powers of discretion to the Director of Library Services to allow the thesis to be copied in whole or in part without further reference to me. This permission covers only single copies made for study purposes, subject to normal conditions of acknowledgement.

Contents

List of Figures

Figure 2.13. Isotherms for surrogate V1 calculated with the GC-PC-SAFT method compared to experimental data for Diesel fuels 1 through 6.

Scheme 3.1. General diagram for multiphase calculations

Figure 3.1. Pressure field for all cases studied in the paper, the black curve draws the saturation line. The colour scale is unique for every figure.

Figure 3.2. Vapor volume fraction field for all cases studied in the paper, the black curve draws the saturation line. The colour scale is the same on every figure.

Figure 3.3. Flash iterations field for all cases studied in the paper, the black curve draws the saturation line. The colour scale is unique for every figure.

Figure 3.4. Flash iterations needed for Cases 5 and 6 at 300K using Peng-Robinson and PC-SAFT as Equations of State at 300K.

Figure 3.6: Predicted vapor-liquid equilibrium compared with experimental data for (a) Case 2, (b) Case 4 and (c) the Y8 mixture [37].

Figure 4.1. Simulated geometry, one fifth of the complete injector nozzle. Characteristic volumes are colourised, and the boundary conditions are indicated.

Figure 4.2. Thermodynamic and thermophysical data following an isentropic expansion of the Diesel surrogate. Three cases are shown depending on the reference temperature at 5MPa: (i) 324K for the barotropic method used in this work, (ii) 384K as the maximum temperature reached in the liquid-vapor equilibrium phase for P_{inj}=180MPa considering thermal effects, and (iii) 484K as the maximum temperature reached in the liquid-vapor equilibrium phase for P_{inj}=450MPa considering thermal effects.

Figure 4.3. Predicted time-averaged vorticity, in logarithmic scale, on different slices at the sac volume and orifice for three injection pressures. Thermal effects are considered.

Figure 4.4. Predicted time-averaged density on different slices at the sac volume and orifice for three injection pressures. Thermal effects are considered. The isosurface for vapour volume fraction of 50% is included, which shows two coherent structures separated at the midplane for (b) and (c).

Figure 4.5. Predicted time-averaged dynamic viscosity on different slices at the sac volume and orifice for three injection pressures. Thermal effects are considered.

Figure 4.6. Mass flow rate at the orifice exit for both barotropic and thermal case.

Figure 4.7. Predicted time-averaged temperature change with respect to the injection temperature, defined as $\left(T - T_{inj}\right)/T_{inj} * 100$, when thermal effects are considered. The injection temperature for each case is shown in Table 3. A solid thick black line is plotted in the longitudinal slice where $T = T_{inj}$, thus all points inside this isoline show cooling and those outside show heating. Results are shown on different slices at the sac volume and orifice for three injection pressures.

Figure 4.8. Variation in temperature for the liquid, vapor and vapor-liquid equilibrium (VLE) phases, when thermal effects are considered, versus the square root of pressure difference. As a reference, both the injection temperature and the reference temperature used in the barotropic approach are included.

Figure 4.9. Predicted time-averaged density-temperature values over the whole computational domain for three different injection pressures. Thermal effects are considered. The saturation curve for the multicomponent Diesel surrogate (solid line) and the isentropic approach (dashed line) are indicated. Colour of the symbols distinguishes the zone in the injector they correspond to.

Figure 4.10. Predicted single-time instance of logarithm of pressure versus density values over the whole computational domain for three injection pressures, when thermal effects are considered; the curve for the barotropic evolution (dashed line) is indicated. The colour of the symbols shows their value of the vapor volume fraction within different ranges.

Figure 4.11. Saturation pressure versus the square root of the pressure difference, found for every injection pressure when thermal effects are considered.

Figure 4.12. Predicted time-averaged pressure on a longitudinal slice of the injector. A solid black isoline at 5MPa, the back pressure, and the isosurface for 50% vapour volume fraction have been included. The colour map is in logarithmic scale and thermal effects are considered.

Figure 4.13. (a) Time-averaged vapor volume fraction inside the injector orifice versus the square root of the pressure difference between injection pressure and back pressure. The symbols show the results both for the barotropic approach and those for thermal effects being considered. (b) Orifice volume fraction histogram for different pressure ranges inside the orifice volume when thermal effects are considered.

Figure 4.14. Effect of boundary/simulation parameters on calculated vapour volume fraction as function of injection pressure

Figure 4.15. Time-averaged vapour mass flow rate along the orifice length for both (a) barotropic and (b) thermal cases, at all injection pressures. Two insets of the temperature distribution are added to the thermal case, corresponding to locations of high vapour mass flow rate at 450MPa. On the slices, an isoline showing the location of vapour is also included.

Figure 4.16. Slope of the vapour mass flow rate along the orifice length, showing locations of net evaporation (positive) and condensation (negative), for both barotropic and thermal cases. A dashed horizontal line is added at value 0, for reference.

Figure 4.17. Time-averaged vapour volume fraction inside the injector orifice versus the square root of the pressure difference between injection pressure and back pressure. All cases have the same cavitation number, CN=35. Thermal effects are considered.

Figure 4.18. Mass fraction of vaporised surrogate and representative components (the heaviest, lightest and two intermediate) as a function of specific volume for a 0D expansion of the fuel at 350K

Figure 4.19. Effect of the injection pressure on the partial vaporisation of a selection of Diesel surrogate components. Results are time-averaged and thermal effects are considered. Per case, the mass fraction used for the isosurfaces is obtained as that for trimethylbenzene which gives the same surface than the one for the mixture 50% vapor volume fraction.

Figure 4.20. Time-averaged predictions for the vaporised mass composition of the vapor cloud, in a stacked fashion, at all injection pressures. Thermal effects are considered.

List of tables

Nomenclature

English symbols

a	reduced molar Helmholtz free energy	k_{ij}	binary interaction parameter
A	molar Helmholtz free energy or viscosity parameter	m	number of segments
B	viscosity parameter	M	Mach number [-]
$\boldsymbol{B}$	Hessian submatrix	M_w	molar weight
C	Viscosity parameter or acoustic impedance	$\dot{m}$	Mass flow rate
$\boldsymbol{C}$	Hessian submatrix	n	number of moles
c	Speed of sound	N_{Av}	Avogadro's number
D	Viscosity parameter or Hessian submatrix	p	pressure
d	temp. dependent segment diameter	R	universal gas constant
$\boldsymbol{E}$	modified Cholesky diagonal matrix	s	entropy
E	Total energy	T	temperature
f	fugacity	t	Time
G_{ij}	viscosity binary interaction parameter	$\mathbf{u}$	Velocity
	site-site radial distribution function	$\tilde{\boldsymbol{u}}$	intermediate Cholesky vector
$\boldsymbol{g}$	gradient vector	V	volume

G	Gibbs free energy	x_i	Mole/mass fraction of component i
$\boldsymbol{H}$	Hessian matrix	X	generic viscosity parameter
h	Enthalpy	Z	compressibility factor
$\boldsymbol{I}$	identity matrix	z_i	Mole/mass fraction of component i in the feed
k_B	Boltzmann constant	$\boldsymbol{Z}$	reducing matrix
K	equilibrium constant		

Greek Symbols

A	transformed stability variables	λ	Thermal conductivity, step length
α_v	Volume vapour fraction	μ	viscosity or chemical potential
β	Molar vapour fraction	ρ	density
δ_{ij}	Kronecker delta	σ	segment diameter or standard deviation
ϵ	energy parameter	$\boldsymbol{\tau}$	Stress tensor
$\boldsymbol{\epsilon}$	variables vector	ψ	generic phase
η	packing fraction	ω	acentric factor
Θ	Mass vapour fraction	Ω	reduced collision integral or generic thermodynamic property

Superscripts

disp	dispersion term	*ig*	ideal gas
hc	hard-chain term	*res*	residual term
$*$	feed property or reduced property	*hs*	hard-sphere term
(k)	iteration number	$'$	trial phase
comp	compressible contribution to the interface pressure	*inc*	incompressible contribution to the interface pressure

Subscripts

a	attractive contribution	j	component *i* ot jth coordinate direction
b	Downstream conditions	*l*	Liquid
c	critical property	*max*	maximum
GC	group contribution parameter	*mix*	mixture property
Inj	At inlet conditions	*r*	repulsive contribution
i	component *i* or the *i*th data point or ith coordinate direction	*sat*	saturation
		v	Vapour

Abbreviations

%*AAD*	average absolute deviation
EoS	equation of state
GC-PC-SAFT	group contribution PC-SAFT

LC-PC-SAFT	literature and correlations PC-SAFT
PC-SAFT	perturbed chain statistical associating fluids theory
nc	number of components
GN	Grunberg-Nissan mixing rule
EM	empirical mixing rule
TPD	Tangent Plane Distance
VLE	Vapour-Liquid Equilibrium

1. Introduction

1.1 Background and motivation

The United Nations Environment Programme (UNEP) reported in November 2018 mentions that "pathways reflecting current nationally determined contributions imply global warming of about 3°C by 2100, with warming continuing afterwards" in its assessment of the Paris Agreement[9]. As the transport sector accounts for 23% of the total Greenhouse Global Emissions[10], attempts have been made to study and find a means to reduce them; Diesel surrogates[11], additives in Diesel and bio-Diesel blends[12], multiple injections per power cycle[13] increase in injection pressure[14]. Modern Diesel engines operate with upstream pressures of around 200MPa at full load, although the current trend is to increase them up to 300MPa, in accordance with the latest emission regulations. However, due to the micrometre scales of injectors, high injection pressures will irremediably cause very high fuel velocities which, combined with the sharp geometric changes in the injector passages, lead to significant pressure gradients and local depressurisation. If the pressure decreases beyond the fuel's saturation point, the fuel cavitates, which in turn is related to injector erosion and underperformance[15]. Despite this, cavitation can be beneficial when managed effectively, as the spray breakup in the combustion chamber is enhanced. This generates smaller droplets and consequently increases combustion efficiency[16]. The main observed effect of cavitation is on liquid jet atomisation[17-20]. One of the first studies on this relationship was that of Faeth et al.[21], where it was found that that primary break-up characteristics were dominated by the characteristics of the in-nozzle flow. Several follow-up studies have reported that cavitation enhances atomisation performance[22], increases the spray cone angle[23], and it is related to mass flux choke due to blocking of the free flow[24]. Moreover, understanding the impact of changes in pressure and temperature on fuel properties is vital for simulating various processes relevant to Diesel injection and combustion. Properties such as density, viscosity, speed of sound and bulk modulus affect the injection process and phase-changing phenomena within the fuel injector, which in turn, control atomisation, mixing, and soot emission levels[25-28].

1.2 Modelling Diesel Fuel

The modelling of Diesel fuel properties in the automotive and energy fields has become a major challenge[29-32] given the lack of experimental data for the wide range of operating conditions at elevated pressures and temperatures and given the lack of relevant, widely accepted modelling methods/correlations. As Diesel fuel is composed of hundreds of hydrocarbons, with unknown individual properties and interactions, research has focused on creating surrogate mixtures[33-35] to mimic the properties of Diesel fuel. Surrogate mixtures ideally consist of a rather small number of hydrocarbons that replicate selected properties of a particular Diesel[36]. Research with surrogate mixtures could improve the understanding and modelling of the relationships between fuel composition and engine combustion[37].

The modelling of nozzle-cavitation, internal nozzle deposit build-up, fuel atomisation, heating and vaporisation depends on the accuracy of estimated Diesel properties at relevant operating conditions. For example, recent studies[38] shows an up to 7% variation in the predicted mass flow rate through Diesel injectors when variable fuel properties are utilised. Similarly, considerable effects on nozzle flow and cavitation[39], fuel vaporisation[40] and near-nozzle spray distribution[41] have been demonstrated. The approaches taken by most studies modelling the thermodynamic and thermophysical properties of Diesel fuel are either based on collections of Diesel properties[42], hydrocarbon property databases in NIST (REFPROP[43]), calculated properties using commercially available software, e.g. ASPEN[44] or SUPERTRAPP[45], calculated properties using cubic equations of state (EoS), or a combination of all of these approaches[46]. However, there are limitations in each of these approaches. For example, the best collection of Diesel fuel properties[42] is limited to pressures and temperatures far from supercritical or saturated vapour conditions. The REFPROP database is defined for a very limited number of hydrocarbons. In addition, fluid property estimations with software relying on a cubic EoS are known to be inaccurate when calculated at high-temperature, high-pressure conditions (HTHP)[47, 48].

The first study investigates the performance of the Perturbed-Chain, Statistical Associating Fluid Theory (PC-SAFT)[49] equation of state (EoS) for modelling the properties of Diesel fuel and Diesel fuel surrogate mixtures over a wide range of pressure-temperature conditions. The PC-SAFT EoS requires three molecular-based parameters per component for fluid property calculations. In this study two approaches are used to obtain the pure component parameters. One approach utilizes parameters reported in the literature that were obtained by fitting vapour pressure and saturated liquid density data[50] or were calculated with correlations based on parameters reported for compounds in the same chemical family[7] (LC-PC-SAFT). The other approach utilizes a group contribution method based on the molecular structure of each component[51] in the fuel or fuel surrogate to calculate the three parameters (GC-PC-SAFT).

Several advantages accrue when using the PC-SAFT EoS compared to a cubic EoS to calculate fluid properties. The PC-SAFT EoS more accurately predicts derivative properties, reducing errors by a factor of up to eight[52, 53], as compared to predictions with a cubic EoS, such as the Peng-Robinson (PR) EoS[54] or Soave-Redlich-Kwong EoS[55]. Density predictions with the PC-SAFT EoS exhibit six times lower error for a widely used surrogate such as dodecane[56] and half the error of those made with improved cubic equations, such as volume-translated versions[57]. The PC-SAFT EoS provides satisfactory agreement between calculated and experimental properties of reservoir fluids[58], natural gas[59] and asphaltene phase behaviour[60, 61]. These studies suggest the PC-SAFT EoS should provide reasonable predictions of Diesel fuel properties at extreme engine operating pressures and temperatures.

1.3 Vapour Liquid Equilibrium Calculations

There is a wide body of research comparing the accuracy of PC-SAFT against other EoS in multiphase problem, not exclusively on vapor-liquid equilibrium. Arya et al.[62] and more recently Vieira de Melo et al.[63] compared the PC-SAFT and Cubic-Plus-Association[50] EoS for phase calculations of asphaltenes present in crude oils where although both EoS gave acceptable results, the authors drew different conclusions. Gong et al.[64] compared Peng Robinson and PC-SAFT EoS while modelling the VLE of mixed

refrigerants, with no clear advantage of using one EoS over another. Held et al.[65] modelled the solubility of sugar and sugar alcohols in ionic liquids, with reasonable accuracy. Peyvandi et al.[66] compared PC-SAFT, SAFT+CUBIC and PR EoS in the modelling of cryogenic fluids, with a clear disadvantage on the use of PR EoS. Economou et al.[67] investigated the VLE of gaseous mixtures related to carbon dioxide capture technologies using several EoS: SRK, PR, SAFT, and PC-SAFT EoS, among them PC-SAFT showed to be the most accurate when no binary interaction parameters (BIP) are used, although comparable accuracy was observed with a fitted BIP. However, most of the studies focus on the modelling of the phase equilibria as 'static' problems, without considering flowing systems, where the VLE problem is only part of the whole framework of Computational Fluid Dynamics simulations. Exceptions can be found on the latest work in Diesel sprays[68] or Diesel injections[69], however the fuel in these two cases is a single component or a pseudo-component and various techniques are used to work around the problem of density undefinition inside the saturation curve. Overall, there seems to be evidence to indicate that independent variables other than pressure and temperature are needed for complex computational fluid dynamics simulations.

The use of flash with density (or specific volume), temperature and composition is particularly useful whenever the pressure is unknown in an enclosed fluid and the phase change is a possibility. This happens in storage tanks design, during the capturing process of acid gases within oil reservoirs, or compositional reservoir simulations as there is no balance equation for pressure[70]. Also, in most real fluid equations of state, e.g. PC-SAFT or cubic EoS, the formulation is given depending naturally on density, or volume, temperature and composition, which also makes the choice of these variables for the VLE calculations the most straight-forward. However, the existing body of research has only employed pressure and temperature as independent variables for vapor-liquid equilibrium calculations (PT-VLE) with the PC-SAFT EoS. Moreover, this method shows its limitations when the phase change is at constant temperature and pressure, characteristic of single components. At constant pressure and temperature, the state of the substance is undetermined at saturation conditions. However, the volume (or density) changes provide the complete information. Lastly, this

undefinition is not restricted only to single components as it also appears in multicomponent mixtures for three phase systems[71] and those composed of similar components, as will be shown in the results section for a Diesel surrogate.

A seminal study in this area is the one of Michelsen[72], who proposed the use of volume and temperature as independent variables and the minimising the Helmholtz Free energy rather than the Gibbs free energy for the multiphase problem. In addition, for pressure-explicit EoS this approach would also avoid the need for an iterative process to find the density from pressure, as the pressure becomes then an output of the minimisation process. This approach was then implemented for the stability testing of hydrocarbon mixtures[73] using the SRK and the PR EoS with the tunnelling method[74]. Following work used the successive substitution iteration (SSI) method and the PR EoS for the flash problem[75]. Over the past decade, studies related to minimising the Helmholtz free energy have been focused on the Newton method[76]. Moreover, new frameworks have been published using variations of the independent variables or decoupling the pressure equality condition during the flash stage[77]. Recently, a framework using constrained minimisation has been also published Paterson et al.[78] in a generalized form for specifications based on state functions other than pressure and temperature. There have been works using density and temperature as independent variables for the calculation of the saturation curves of single components in PC-SAFT[79, 80]. However, to author's best knowledge, stability analysis and flash calculations using this equation of state have been restricted to temperature *T* and pressure *P* as independent variables[81].

Following the above limitation when pressure and temperature are used as independent variables, the novelty of this work is the provision and assessment of the necessary numerical framework using composition, density and temperature as input variables for the calculation of the vapor-liquid equilibrium within the structure of PC-SAFT, via the unconstrained minimisation of the Helmholtz Free energy.

In the second study, the minimum of the molar Helmholtz Free energy *A* is calculated, defined in terms of density ρ, temperature T and composition $\boldsymbol{z}$ as:

$$A(\boldsymbol{z},\rho,T) = \sum_{i=1}^{nc} z_i A_i^{id}(P(\boldsymbol{z},\rho,T),T) \; + \; A^{res}(\boldsymbol{z},\rho,T) \tag{1.1}$$

Where the superscripts id and res refer to the ideal, given by the fundamental gas relation, and residual contributions of the Helmholtz Free Energy, modelled by PC-SAFT, respectively. This optimisation problem is solved via a combination of the successive substitution iteration (SSI) and the Newton minimisation method with a two-step line-search procedure, and the positive definiteness of the Hessian is guaranteed by a modified Cholesky decomposition[82]. The algorithm consists of two stages: first, the mixture is assumed to be in a single phase state and its stability is assessed via the minimisation of the Tangent Plane Distance (TPD); in case the minimum of the TPD is found to be negative, the mixture is considered unstable and a second stage of flash, i.e. phase splitting, takes place consisting on the search for the global minimum of the Helmholtz Free Energy. As a result, the pressure of the fluid and the compositions of both the liquid and vapor phases are calculated, from which every other thermodynamic and thermophysical property can be calculated, i.e. internal energy, enthalpy, entropy, speed of sound, etc, using the PC-SAFT[49]. The reliability of two different methods for the flash stage, NVL [83] and lnK[77], are evaluated in terms of both iterations and computing time needed to reach convergence. Following the work of von Solmons et al in VLE calculations[84], this work also assesses the computational time needed for its completion. The robustness of the algorithm is then tested with a mixture of 50 components and several other examples often found in the literature in two-phase equilibrium calculations. Particular attention is paid to the case of a single component and a Diesel surrogate, known to reproduce the already highlighted incomplete density information when using pressure and temperature as independent variables. The overall accuracy of the VT-VLE algorithm combined with PC-SAFT is tested against experimental data for a selected number of examples.

1.4 Preferential cavitation and friction-induced heating of multi-component Diesel fuel surrogates up to 450MPa

Cavitation measurements in real-size injectors operating pressures beyond 200MPa[85] has not been possible up to now, due to transparent material constrains. Even for lower pressure conditions, only qualitative images have been obtained but not quantitative data for the cavitation volume fraction or the velocity field. There are published works for injection pressures up to 500MPa, but only spray formation results have been reported[86], but without information about the in-nozzle flow. Both volume of fluid method (VOF)[87, 88] and the homogeneous equilibrium model (HEM) have been used to simulate the presence of the second phase due to cavitation[89] and validated against relevant experiments at lower pressures[90]. Such models can be used to study the formation and transport of the vapour phase, the turbulent fluctuations in velocity and pressure and the effect of non-condensable gases[91].

It has been also possible to look into the effect of liquid and vapour compressibility on supercavitation formation[92]. More specifically, homogeneous mixture models (either barotropic or mass transfer) have been found to have very similar performance[93, 94] in the limit of large mass transfer rates of the former. Also, such models have been validated for predicting the 3D distribution of vapor fraction within the validation uncertainty (±7%, including both numerical and experimental uncertainties). Further validation has been obtained for the flow field distribution, cavitation frequency shedding and turbulent velocities in the same single-hole injector against high energy X-ray phase contrast imaging (XPCI) measurements for conditions covering a range of cavitation regimes (incipient, fully developed and vortex/string cavitation)[95, 96].

Additionally, validation against Laser Doppler Velocimetry (LDV) measurements has been also reported[93]; this study has also utilised the WALE LES model for turbulence, as it has been proved that can reproduce accurately the turbulent structures found in Diesel nozzles. These studies suggest this model is capable of capturing both incipient and developed cavitation turbulent features. For injection

pressures in the range of 180MPa, the same simulated injector geometry was previously validated for predicting cavitation erosion damage[2] utilising the barotropic model. Cavitation erosion predictions have been also validated recently against measurements in a fuel pump[97]. These studies give confidence that the barotropic model is performing relatively well for similar cases as those studied in this work.

Moreover, the high velocity gradients induce wall friction, generating an important source of heating. However, there are no experiments available that can be used for validation. Previous works have compared results against 0-D predictions of the mean fuel heating up as it discharges through the fuel injector up to 300MPa, with very good accuracy[38, 39]. Nonetheless, thermal effects are typically neglected, and the thermodynamic properties of the fuel are assumed constant and the flow within the fuel injector isothermal. This assumption is based on the short time scales of the cavitation process and the short residence time within the injector nozzle, which decreases the importance of heat transfer. However, as the pressures within the injector increase, significant changes to fuel thermodynamic and thermophysical properties are realised, which are critical in the formation of cavitation[98]. With regards to liquid density variation, a barotropic evolution of the liquid density as function of pressure is frequently utilised[99], if not assumed constant. A barotropic equation has been derived in past studies following Kolev's Diesel properties collection[100] or single component surrogates using the NIST Refprop[2] database. Such simplifications may lead to deviations in the discharge coefficient and fuel heating predictions with respect to the real fuel, particularly in cases of high pressure injections[39]. For the vapour phase, the usual assumption is the ideal gas behaviour. The simulations carried out in this work utilise properties derived by the 8-component surrogate modelled with PC-SAFT EoS, found to be a close match to a real Diesel fuel, even at high pressures.

As noted in the previous sections, real Diesel fuels are typically composed of hundreds of components, which cannot be addressed by the use of constant properties or a simplified equation of state (EoS). Composition effects in Diesel fuel are related to changes in the spray atomisation[101] and spray tip penetration[102], but the vaporisation of each component in the multicomponent fluid during

injection has not been addressed. There is only one related study in which the effect of non-condensable gas on the cavitation of a single component fuel during injection is analysed[103], modelled with a cubic EoS. Experiments of Diesel and biodiesel fuel mixtures have shown that the biodiesel content slows down the complete vaporisation due to its higher molar weight[104], which was also seen numerically at extreme temperatures[105]. Still, most studies regarding preferential vaporisation and transport based on the solution of the full Navier-Stokes equations are based on models for fuel droplets in a gaseous environment[106].

Two main assumptions related to the multiphase flow typical of Diesel injection simulations is the mechanical and thermodynamic equilibrium between the liquid and the vapour phases. With regards to the mechanical equilibrium assumption, the recent study using a two-fluid model has confirmed that differences between liquid and vapour velocities are less than 10% and only in localised locations of the flow[107]; they have been found not to affect the overall growth rate and production of vapour. The assumption of thermodynamic equilibrium is more significant. A metastable, i.e. non-thermodynamic equilibrium, state occurs when the pressure of the liquid drops below the saturation pressure and no vapour is formed, thus existing liquid tension, due to the rapid expansion of the liquid[108, 109]. In the literature, non-thermodynamic equilibrium models, such as mass transfer models, are widely used. These cavitation rate models are based on transport equations, such as the well-known Schnerr and Sauer[110], Singhal et al.[111] and Zwart et al.[112] models. Moreover, mass transfer models can tend towards equilibrium by using large mass transfer terms, i.e. increasing the evaporation/condensation coefficients[94, 113]. Apart from mass transfer models, in the literature there are models relying on the solution of the full Rayleigh-Plesset equation, commonly done in a Lagrangian reference frame, thus incorporating second order effects and the influence of surface tension. However, such models inherently assume a spherical bubble shape, the interaction between bubbles (break-up, coalescence) is not easy to describe and the coupling with the continuous phase (liquid) is difficult in areas of large void fractions[114].

Finally, the present work omits transient effects related to the motion of the needle valve[115], while it refers to only one injector geometry utilised with heavy-duty diesel engines featuring hole tapering. It has been reported in the literature that cavitation reduces the mixing uniformity within circular, sharp-edged orifices[116] while tapered nozzles reduce its appearance[117]. With regards to the needle valve motion, it is well documented in the literature that depending on the nozzle geometry and needle valve position, cavitation may appear to the bottom part of the injection hole as well as the needle seat area and inside the nozzle's sac volume at low needle lifts[118-120]. More recent studies have shown that the initial air/liquid distribution inside the nozzle volume prior to the start of injection are also complex, with large air bubbles been present[118, 120-122]; these are formed during the needle valve closure that induces back flow to the injector. However, such effects and flow regimes are not realised when the needle valve is at its nominal full lift position. At the same time, the needle remains still for a relatively large duration, typically more than 10 times longer compared to the opening/closing time.

1.5 Objectives

The objectives of this thesis can be summarized as follows:

- To model Diesel fuels with PC-SAFT, considering the multicomponent nature of these fuels.
- To compare the modelled properties with available experimental data.
- To couple the PC-SAFT model with a Vapour-Liquid Equilibrium algorithm using density, temperature and composition as inputs.
- To produce a Diesel fuel property database for its application on CFD simulations.
- To simulate Diesel fuel injections at extreme injection pressures.
- To study the effects of friction-induced heating at extreme injection pressures.
- To study the effects on cavitation and preferential vaporisation as the injection pressure increases.

1.6 Thesis outline

The main body of this thesis is divided in three sections:

- **Modelling of Diesel fuel properties through its surrogates using PC-SAFT**

The PC-SAFT equation of state is utilised to model the effect of pressure and temperature on the density, volatility and viscosity of four Diesel surrogates; these calculated properties are then compared to the properties of several Diesel fuels. PC-SAFT calculations are performed using different sources for the pure component parameters. Surrogate viscosity is calculated using the entropy scaling model with a new mixing rule for calculating mixture model parameters. The PC-SAFT results are compared to calculations using the Peng-Robinson equation of state; the greater performance of the PC-SAFT approach for calculating fluid properties is demonstrated.

- **Vapor-Liquid Equilibrium calculations at specified composition, density and temperature with the Perturbed Chain Statistical Associating Fluid Theory (PC-SAFT) Equation of State**

A vapour-liquid equilibrium algorithm is coupled with PC-SAFT, using as independent variables the mixture composition, density and temperature. This algorithm is based on unconstrained minimisation of the Helmholtz Free energy via a combination of the successive substitution iteration and Newton-Raphson minimisation. The algorithm consists of the typical two stages of stability and phase splitting. The reliability of two different methods presented in the existing literature is assessed for 7 different cases.

- **Numerical assessment of thermal effects and preferential cavitation of multi-component Diesel fuel surrogates up to 450MPa**

The aim of the third and last study is to investigate the in-nozzle flow and cavitation during a Diesel injection at injection pressures up to 450MPa using a realistic multicomponent Diesel surrogate. This surrogate is a mixture of eight components based on the composition of a grade no. 2-D S15 Diesel emissions certification fuel from Chevron-Phillips Chemical Co[1].

Two different methodologies have been utilised: one neglecting the thermal effects and one where the energy equation is solved considering thermal effects due to friction. To the best of the author's knowledge, this is the first study in the literature where the PC-SAFT is utilised in nozzle flow simulations addressing the preferential cavitation of the fuel components and their evolution at extreme injection pressures.

2. Modelling of Diesel fuel properties through its surrogates using PC-SAFT

On this section, The PC-SAFT equation of state is utilised to model the effect of pressure and temperature on the density, volatility and viscosity of four Diesel surrogates; these calculated properties are then compared to the properties of several Diesel fuels. PC-SAFT calculations are performed using different sources for the pure component parameters. Surrogate viscosity is calculated using the entropy scaling model with a new mixing rule for calculating mixture model parameters. The PC-SAFT results are compared to calculations using the Peng-Robinson equation of state; the greater performance of the PC-SAFT approach for calculating fluid properties is demonstrated.

2.1 Surrogates studied

Table 2.1**Table** lists the molecular weights, molar compositions, and normal boiling points of four Diesel surrogates reported by Mueller et al.[1], who refer to the surrogates as V0a, V0b, V1, and V2. The authors of this study group the surrogates into two broad "accuracy" types depending on how closely the composition matches that of a 2007 #2 ULSD certification fuel from Chevron-Phillips Chemical Co. V0a and V0b are labelled low-accuracy surrogates that only contain four and five components, respectively, and V1 and V2 are labelled high-accuracy surrogates that contain eight and nine components, respectively. V0a, with four components, is derived numerically for combustion and emissions simulations[123]. V0b, with five components, better mimics the heavy molecular weight end of the Diesel distillation curve. The authors report that the components in V1 are chosen to match fuel composition, ignition quality, volatility, and density of Diesel[33]. V2, the surrogate with the largest number of components, exhibits properties similar to real fuel composition, but it also has five new components with respect to those in surrogate V1. In the present study the PC-SAFT EoS is used to predict the thermodynamic (density and volatility) and transport (viscosity) properties of the four Diesel surrogate mixtures at 0.1 MPa to assess the performance of this EoS to match available

surrogate mixture properties. Unfortunately, there are no available experimental literature data for the high-pressure, high-temperature properties of the four surrogates. Therefore, predictions from both the LC-PC-SAFT and GC-PC-SAFT methods are then used to compare calculated surrogate properties to those experimentally reported for Diesel[1, 33], including high pressure densities and viscosities. The comparison of calculated surrogate mixture properties with experimental Diesel properties provides insight into the impact of the number and type of components needed for a surrogate mixture to mimic Diesel fluid properties.

	M_w	T_b	Surrogate mol %			
Compound	[*g*/*mol*]	[*K*]	V0a	V0b	V1	V2
n-hexadecane	226.4	560.0	27.8	-	2.7	-
n-octadecane	254.5	590.0	-	23.5	20.2	10.8
n-eicosane	282.5	617.0	-	-	-	0.8
heptamethylnonane	226.4	520.0	36.3	27.0	29.2	-
2-methylheptadecane	254.5	584.3	-	-	-	7.3
n-butylcyclohexane	140.3	456.2	-	-	5.1	19.1
triisopropylcyclohexane	210.4	523.2	-	-	-	11.0
trans-decalin	138.2	460.5	14.8	-	5.5	-
perhydrophenanthrene	192.3	546.9	-	-	-	6.0
1,2,4-trimethylbenzene	120.2	442.6	-	12.5	7.5	-
1,3,5-triisopropylbenzene	204.4	509.5	-	-	-	14.7
tetralin	132.2	480.9	-	20.9	15.4	16.4
1-methylnaphthalene	142.2	518.0	21.1	16.1	14.4	13.9

Table 2.1:Molar composition for the four Diesel fuel surrogates (V0a, V0b, V1, V2) [5]modelled here. Boiling points at 0.10MPa taken from the literature.

2.2 Numerical method

This work is supported by public funding of the European Commission. As such, the complete algorithm described in the following sections is available upon request.

2.2.1 PC-SAFT Equation of State

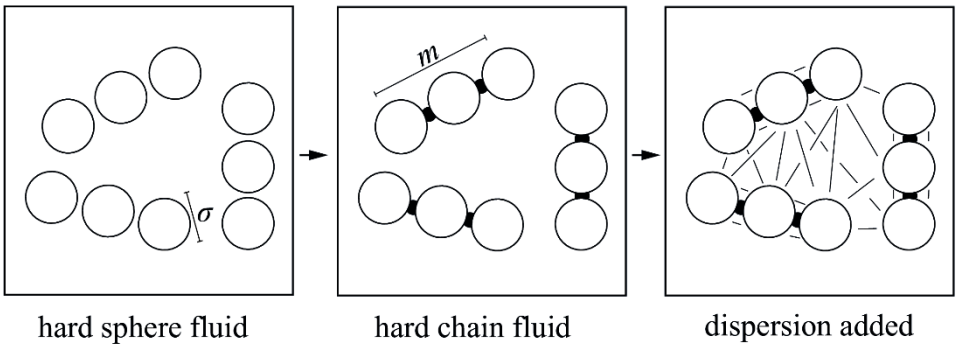

Figure 2.1: Schematic of three, non-associating molecules modelled with the PC-SAFT EoS. Each molecule is decomposed into spherical segments of diameter *σ*. The segments then form chains of length *m* that interact via dispersion forces.

The PC-SAFT EoS[49] is a theoretically derived model, based on perturbation theory[124-127], that splits the intermolecular potential energy of the fluid into a reference term accounting for repulsive interactions and a perturbation term accounting for attractive interactions. Figure 2.1 shows the modelling of molecules in PC-SAFT. The reference fluid is composed of spherical segments comprising a hard sphere fluid that then forms molecular chains to create the hard-chain fluid. The attractive interactions, perturbations to the reference system, are accounted for with the dispersion term. Intermolecular interaction terms accounting for segment self- or cross-associations are ignored in the form of the PC-SAFT EoS used here given the molecular structure of the surrogate Diesel compounds listed in Table 2.1. Hence, each component is characterized by three pure component parameters, which are a temperature-independent segment diameter, σ, a segment interaction energy, ϵ and a number of segments per molecule m.

The PC-SAFT EoS is derived as summations of the residual Helmholtz free energy, as shown in:

$$\frac{A^{res}}{RT} = a^{res} = a - a^{ig} = a^{hc} + a^{disp} \tag{2.1}$$

where *R* is the universal gas constant and *T* is the temperature. The hard-sphere contribution, a^{hs}, is embedded in the hard-chain term, a^{hc}, which for a mixture of nc components, is by.

$$a^{hc} = \overline{m}a^{hs} - \sum_{i}^{nc} x_i(m_i - 1)\ ln\, g_{ii}^{hs}(\sigma_{ii}) \tag{2.2}$$

where $\overline{m}$ is the number of segments for a multicomponent mixture,

$$\overline{m} = \sum_{i}^{nc} x_i\, m_i \tag{2.3}$$

and x_i is the mole fraction of every component i in the fluid. The hard sphere contribution is defined as

$$a^{hs} = \frac{1}{\zeta_0}\left[\frac{3\zeta_1\zeta_2}{(1-\zeta_3)} + \frac{\zeta_2^3}{\zeta_3(1-\zeta_3)^2} + \left(\frac{\zeta_2^3}{\zeta_3^2} - \zeta_0\right) ln\,(1-\zeta_3)\right] \tag{2.4}$$

where ζ_n are defined abbreviations and the term g_{ij}^{hs} in Equation (2.2) is the radial distribution function of the hard-sphere fluid.

$$g_{ij}^{hs} = \frac{1}{(1-\zeta_3)} + \left(\frac{d_i d_j}{d_i + d_j}\right)\frac{3\zeta_2}{(1-\zeta_3)^2} + \left(\frac{d_i d_j}{d_i + d_j}\right)^2 \frac{2\zeta_2^2}{(1-\zeta_3)^3} \tag{2.5}$$

where ζ_n is defined as:

$$\zeta_n = \frac{\pi}{6}\rho^* \sum_{i}^{nc} x_i\, m_i d_i^n \qquad n \in \{0,1,2,3\} \tag{2.6}$$

and ρ^* is the molecular density and d_i, the temperature-dependent segment diameter of component i is

$$d_i = \sigma_i\left[1 - 0.12\, exp\left(-3\frac{\epsilon_i}{k_B T}\right)\right] \tag{2.7}$$

where k_B is the Boltzmann constant. The dispersion term is defined as:

$$a^{disp} = -2\pi\rho I_1(\eta, \overline{m})\overline{m^2\epsilon\sigma^3} - \pi\rho\overline{m}C_1 I_2(\eta, \overline{m})\overline{m^2\epsilon^2\sigma^3} \tag{2.8}$$

where $\eta = \zeta_3$ is the reduced density, I_1 and I_2 are integrals approximated by simple power series in density, and C_1, an abbreviation for the compressibility factor Z, is given as:

$$C_1 = \left(1 + Z^{hc} + \rho\frac{\partial Z^{hc}}{\partial \rho}\right)^{-1} = \left(1 + \overline{m}\frac{8\eta - 2\eta^2}{(1-\eta)^4} + (1-\overline{m})\frac{20\eta - 27\eta^2 + 12\eta^3 - 2\eta^4}{[(1-\eta)(2-\eta)]^2}\right)^{-1} \quad (2.9)$$

The terms $\overline{m^2\epsilon\sigma^3}$ and $\overline{m^2\epsilon^2\sigma^3}$ are abbreviations which represent properties of the mixture:

$$\overline{m^2\epsilon\sigma^3} = \sum_i^{nc}\sum_j^{nc} x_i\, x_j m_i m_j \left(\frac{\epsilon_{ij}}{k_B T}\right)\sigma_{ij}^3 \quad (2.10)$$

$$\overline{m^2\epsilon^2\sigma^3} = \sum_i^{nc}\sum_j^{nc} x_i\, x_j m_i m_j \left(\frac{\epsilon_{ij}}{k_B T}\right)^2\sigma_{ij}^3 \quad (2.11)$$

To model the mixture parameters σ_{ij} and ϵ_{ij}, defined for every pair of unlike segments, a modified Berthelot-Lorentz combining rule[128] is used:

$$\sigma_{ij} = \frac{1}{2}(\sigma_i + \sigma_j) \quad (2.12)$$

$$\epsilon_{ij} = \sqrt{\epsilon_i\epsilon_j}(1 - k_{ij}) \quad (2.13)$$

where k_{ij}, the binary interaction parameter, is used to correct the segment-segment interactions between unlike chains. For the Diesel surrogate mixture compounds listed in Table 2.1, k_{ij} is expected to be a positive number less than ~0.150[129, 130]. However, in this study k_{ij} is set to zero for predictive calculations that only depend on pure component parameters.

Once the different contributions to the residual molar Helmholtz free energy have been defined, every other thermophysical property can be calculated by its derivatives, as the Helmholtz free energy is a thermodynamic potential. The properties studied in this paper are density, volatility and viscosity.

2.2.1.1 Method for Calculating Density

At a fixed system pressure *p*, the density of the fluid is adjusted until the calculated pressure equals the system pressure. More specifically, the iterative method uses the packing fraction η and calculates the pressure by the expression

$$p^{calc} = \left(1 + \eta\left[\left(\frac{\partial a^{hc}}{\partial \eta}\right)_{T,x_i} + \left(\frac{\partial a^{disp}}{\partial \eta}\right)_{T,x_i}\right]\right) k_B T \rho^* \, 10^{30} \tag{2.14}$$

Once the iterative method converges, the following expression is used to convert the packing fraction to density in SI units $[\mathrm{kg/m^3}]$:

$$\rho = \frac{6\eta}{\pi}\left(N_{Av}\sum_i^{nc} x_i \, m_i d_i^3\right)^{-1} \sum_i^{nc} x_i M_{w_i}\left(10^{-3}\frac{kg}{g}\right) 10^{30} \tag{2.15}$$

where N_{Av} is Avogadro's number and M_{w_i} is the molar weight in $[g/mol]$ of each component. Details on the derivatives of the residual molar Helmholtz free energy are found in the original PC-SAFT published work[49].

2.2.1.2 Method for Calculating Volatility

Volatility, i.e. the conditions governing the formation of vapour in a fluid, is essential to the understanding of bubble formation in injector nozzle flow, to the steps leading to cavitation phenomenon, and, importantly, to the vaporisation of the fuel prior to combustion. In contrast to the behaviour of a pure component, bubble formation within a mixture does not occur at a constant temperature and pressure, but rather each component comprising the Diesel fuel or surrogate mixture vaporises at a different rate dependent on the operating pressures and temperatures. For instance, 1,2,4-trimethylbenzene, the lightest component in several surrogate mixtures, has a boiling point at atmospheric pressure of 442.6 K, but at the same pressure the heaviest component, n-eicosane, boils at 616.9 K. For this study, the occurrence of a vapour bubble in the mixture is determined by minimizing the Gibbs Free Energy and applying the tangent plane criterion to find the most stable state(s) of the fluid system, according to a published algorithm[131] consisting of a stability

analysis followed by a phase equilibrium calculation. The stability criterion, i.e. whether the fluid exists as a single phase or as multiple phases, was first proposed by Baker et al.[132], who demonstrated that a fluid system remains a stable single phase for certain conditions of pressure, temperature and composition (here denoted $\boldsymbol{z}$) if the tangent plane to the Gibbs energy surface at composition $\boldsymbol{z}$ is never intersected by the Gibbs energy surface for any other composition $\boldsymbol{x}$. Michelsen[72] provides a mathematical algorithm defining the vertical distance $F(\boldsymbol{x}, T, p)$ from the molar Gibbs energy surface at the trial composition $\boldsymbol{x}$ to the Gibbs energy surface at composition $\boldsymbol{z}$, which in terms of the chemical potential μ_i for every component i is

$$F(\boldsymbol{x}, T, p) = \sum_{i}^{n_c} x_i\big(\mu_i(\boldsymbol{x}, T, p) - \mu(\boldsymbol{z}, T, p)\big) \geq 0 \qquad \forall \boldsymbol{x} \geq 0 \tag{2.16}$$

In the present study, Equation 2.16 is solved using the quasi-Newton BFGS minimization method[133]. If $F(\boldsymbol{x}, T, p)$ is negative at molar fraction $\boldsymbol{x}$, the fluid has split into two phases and the phase equilibrium calculation is then solved by searching for the global minimum of the molar Gibbs energy, G, of the system

$$Min\ G = \sum_{i}^{n_c} \sum_{\psi}^{2} n_i^{(\psi)} \mu_i^{(\psi)} \tag{2.17}$$

where $n_i^{(\psi)}$ is the molar number of component i in phase ψ to mole of feed. This minimation problem is also solved with the quasi-Newton BFGS minimization method.

2.2.1.3 Method for Calculating Viscosity

The recent work by Baled et al.[134] compares the performance of several viscosity models available for hydrocarbons. These authors report that empirical models, such as the Lohrenz-Bray-Clarke[135], are not recommended for high pressure viscosity calculations due to the lack of predictability of the parameters needed in the models. They further note that the semi-theoretical, correlative viscosity prediction methods, e.g. friction theory[136], free volume theory[137] or expanded fluid theory[138], provide satisfactory high pressure viscosity predictions, however these models all require some experimental

viscosity data to calculate model parameters. Other semi-theoretical models, popular in reservoir simulations, are the Chung-Ajlan-Lee-Starling[139] and the corresponding states Pedersen and Fredenslund[140] viscosity models, that, unfortunately, fail to provide reliable viscosity predictions at extreme operating conditions. Baled and co-workers recommend using the entropy scaling model of Lötgering-Lin and Gross[141] to calculate viscosity at wide ranges of pressures and temperatures since this model provides predictions in reasonable agreement with experimental data without a need for fitting parameters. As a consequence of the paucity of experimental data for some of the components used in this work, viscosity will be calculated using the entropy scaling model. These compounds include heptamethylnonane, n-butylcyclohexane, triisopropylcyclohexane and perhydrophenanthrene.

The entropy scaling viscosity model [142] allows transport properties, such as self-diffusion and dynamic viscosity, to be correlated to a power series of the reduced residual entropy, $s^{res}/\overline{m}$, and the universal gas constant, *R*. For a pure component, the reduced viscosity, μ^*, is obtained with the following expression

$$ln\,(\mu^*) = A_i + B_i\left(\frac{s^{res}}{\overline{m}R}\right) + C_i\left(\frac{s^{res}}{\overline{m}R}\right)^2 + D_i\left(\frac{s^{res}}{\overline{m}R}\right)^3 \tag{2.18}$$

where A_i, B_i, C_i, and D_i are viscosity parameters determined from a specific group contribution method reported by Lötgering-Lin and Gross[141]. The reduced viscosity is given by

$$\mu^* = \mu/\mu_{CE} \tag{2.19}$$

where μ_{CE} is the Chapman-Enskog (CE) reference viscosity given as

$$\mu_{CE} = \frac{5}{16}\,\frac{\sqrt{M_w k_B T/(m_{GC} N_A \pi)}}{\sigma_{GC}^2\,\Omega_{GC}^{(2,2)*}} \tag{2.20}$$

where m_{GC} and σ_{GC} refer to the GC parameters and $\Omega_{GC}^{(2,2)*}$ to the reduced collision integral[143].

It is important to recognize that Lötgering-Lin and Gross used the GC method of Sauer, et al.[144] when they developed the viscosity entropy scaling parameters needed for the CE reference viscosity and, therefore, these same GC parameters are used here to calculate the CE viscosity. The Sauer GC parameters differ from those of Tihic, et al.[51], which are used here for density, volatility, and residual entropy calculations. Tihic's GC parameters provide a better match of the PC-SAFT hexadecane (C16), octadecane (C18), eicosane (C20), and 2-methylheptadecane (2-methyl-C17) pure component parameters found from fitting this EoS to vapour pressure and saturated liquid density data. Rather than fit n-alkane data as a single chemical family, Sauer and co-workers determined n-alkane GC parameters by simultaneously fitting both normal and branched alkane data, which results in ~ 10% lower than expected ε/k values for C16, C18, C20, and 2-methyl-C17. Therefore, in the present study, LC and Tihic's GC-PC-SAFT parameters are used to calculate the residual entropy, Lötgering-Lin and Gross's GC parameters are used to calculate the constants in the entropy scaling equation, and Sauer's GC parameters are used to calculate the CE reference viscosity needed to calculate viscosity. Straightforward mixing rules [145] are used with the PC-SAFT EoS to calculate the fluid properties of the mixtures considered here.

Initial calculations are performed in two different ways to determine, μ_{mix}, the mixture viscosity. One approach uses the Grunberg-Nissan mixing rule[146], which requires values for the viscosity of each component in the mixture

$$ln\,\mu_{mix} = \sum_{i}^{nc} x_i\, ln(\mu_i) + \sum_{i}^{nc}\sum_{j}^{nc}\left(1-\delta_{ij}\right)x_i x_j G_{ij} \qquad (2.21)$$

where δ_{ij} is the Kronecker delta, set to 1 when *i=j* and to 0 in any other case. The interaction parameter G_{ij} in the Grunberg-Nissan equation is set to zero here to obtain predictives using only pure component parameters and, in fact, mixture viscosity data is not available to fit this parameter.

The second, computationally simpler approach, is to use a mixing rule to calculate A_{mix}, B_{mix}, C_{mix}, or D_{mix} needed to calculate μ^*. The mixing rule used here follows from the mixing rule shown as equation (4) in Novak[147].

$$Z_{mix} = \frac{\sum_i^{nc} x_i m_{i_{GC}} \sigma_{i_{GC}}^2 Z_i}{\sum_i^{nc} x_i m_{i_{GC}} \sigma_{i_{GC}}^2} \tag{2.22}$$

where Z_{mix} stands for A_{mix}, B_{mix}, C_{mix}, or D_{mix}, nc is the number of components in the mixture and x_i is the mole fraction of component i. For each component i, Sauer's GC method[144] is used to calculate $m_{i_{GC}}$, the number of segments, and $\sigma_{i_{GC}}$, the segment diameter. Z_i, which represents A_i, B_i, C_i, or D_i, is calculated using the Lottering-Lin and Gross GC approach for each component.

2.3 Results and discussion

Initially the PC-SAFT pure component parameters are calculated for the 13 compounds found in the four Diesel fuel surrogates[1], V0a, V0b, V1, and V2, listed in Table 2.1. Once the pure component parameters are determined, the LC-PC-SAFT and GC-PC-SAFT approach are used to calculate surrogate properties of density, volatility in terms of boiling temperature, and viscosity. These surrogate properties are then compared to available experimental data of the same surrogates[1] available at near ambient conditions and to the properties of six different Diesel fuels[1, 3] at temperatures from 298 to 373 K and pressures from 0.1 to 500 MPa. Unfortunately, there is no composition characterization information for five Diesel fuels[3]. Nevertheless, their origin (British), time of year (summer) and existing additives are known, as listed here:

- Fuel 1: British refinery #1 with no performance or handling additives.
- Fuel 2: British refinery #1 with both handling and performance additives.
- Fuel 3: British refinery #2 with both handling and performance additives.
- Fuel 4: British refinery #2 with 5% rape methyl ester.
- Fuel 5: A commercially available retail fuel.
- Fuel 6: A 2007 #2 summer ULSD certification fuel from Chevron-Phillips Chemical Company with detailed compositional analysis[1]

The numerical results are presented in bar graphs, tables, or are interpreted using the Average Absolute Deviation, AAD [%], defined as

$$AAD_{\Omega}[\%] = \frac{100}{N_p}\sum_{i}^{N_p}\left|\frac{\Omega_i^{exp} - \Omega_i^{calc}}{\Omega_i^{exp}}\right| \tag{2.23}$$

where Ω represents the density, boiling temperature, or viscosity and N_p is the number of compared experimental data points.

2.3.1 LC/GC-PC-SAFT parameter characterization

Parameter	n-Alkanes	Cyclo-Alkanes
m	$0.02569M_w + 0.8709$	$0.02254M_w + 0.6827$
$m\sigma^3$ (Å^3)	$1.7284M_w + 18.787$	$1.7115M_w + 1.9393$
$m\epsilon/k_B$ (K)	$6.8248M_w + 141.14$	$6.4962M_w + 154.53$
Parameter	Aromatics	Branched Alkanes
m	$0.02576M_w + 0.2588$	$0.02569M_w + 0.8709$
$m\sigma^3$ (Å^3)	$1.7539M_w - 21.324$	$(m\sigma^3)_0 / \left(1 + 0.86381\left(\frac{SG}{(SG)_0} - 1\right)\right)$
$m\epsilon/k_B$ (K)	$6.6756M_w + 172.40$	$6.8311M_w + 124.42$

Table 2.2: Correlations used for the three pure component parameters[148], depending on the hydrocarbon class, when their values were unavailable in the literature. For branched alkanes, the subscript 0 refers to the parameter values for the n-alkane with the same molecular weight as the branched alkane and SG refers to the specific gravity.

The GC-PC-SAFT pure compound parameters are calculated taking into account only the molecular structure[51]. In contrast, the LC-PC-SAFT parameters are found in the literature and were obtained by fitting experimental data or were calculated using correlations given in Table 2.2 for different chemical families[7], when the parameters were not available. The correlations in Table 2.2 are used to calculate the pure component parameters of 2,2,4,4,6,8,8-heptamethylnonane, 2-methylheptadecane, 1,3,5-triisopropylcyclohexane, perhydrophenanthrene, and 1,3,5-triisopropylbenzene. Table 2.3 presents the pure component parameters for all 13 components found in different amounts in the four Diesel fuel surrogates considered here.

Palette Compound Name	LC-PC-SAFT			GC-PC-SAFT		
	m	σ[Å]	$\epsilon/k_B[K]$	m_{gc}	σ_{gc}[Å]	$\epsilon_{gc}/k_B[K]$
n-hexadecane	6.6485	3.9552	254.70	6.669	3.944	253.59
n-octadecane	7.3271	3.9668	256.20	7.438	3.948	254.90
n-eicosane	7.9849	3.9869	257.75	8.207	3.952	255.96
heptamethylnonane	6.6883	3.9503	249.88	5.603	4.164	266.46
2-methylheptadecane	7.4090	3.9477	251.44	7.374	3.959	254.83
n-butylcyclohexane	3.6023	4.0637	285.97	3.682	4.036	282.41
1,3,5-triisopropylcyclohexane	5.4251	4.0562	280.40	4.959	4.177	297.48
trans-decalin	3.1578	4.1329	313.21	3.291	4.067	307.98
perhydrophenanthrene	5.0171	4.0410	279.81	4.211	3.851	337.52
1,2,4-trimethylbenzene	3.5204	3.7770	287.45	3.610	3.749	284.25
1,3,5-triisopropylbenzene	5.5241	3.9373	278.21	5.178	4.029	296.68
tetralin	3.3131	3.8750	325.07	3.088	3.996	337.46
1-methylnaphthalene	3.5975	3.8173	335.57	3.422	3.901	337.14

Table 2.3: LC-PC-SAFT and GC-PC-SAFT pure component parameters for the 13 compounds in the surrogate mixtures listed in Table 2.1.

The predictive capabilities of the GC and LC models are shown in Table 2.4 by listing the predicted boiling point at 0.1MPa for each palette component along with the absolute percent deviation from available data. The LC-PC-SAFT predicted boiling points for nine of the palette compounds are within ~ 0.5% of experimental values, while the predictions for heptamethylnonane, 1,3,5-triisopropylcyclohexane, perhydrophenantrene, and 1,3,5-triisopropylbenzene differ by 2-to-9% from experimentally reported values. The reason is not apparent for the larger discrepancy with these four compounds. The performance of the GC-PC-SAFT method is close to, but not quite as good as, that observed with the LC method. For eight palette compounds the error with the GC predicted boiling points are slightly greater than those using the LC method, although the maximum error in these cases is still less than 1.0%. The exceptions are the GC predicted boiling points for the other five palette

compounds with the boiling point for 1,3,5-triisopropylbenzene exhibiting a rather large 12.3%. With the exception of the predictions for a few of the palette compounds, both estimation techniques provide reasonable estimates of the normal boiling temperature without the need for experimental data.

	T_b	Prediction [K]		Error [%]	
Compound	[*K*]	LC	GC	LC	GC
n-hexadecane	560.0	560.0	559.5	0	0.09
n-octadecane	590.0	589.6	590.6	0.07	0.10
n-eicosane	617.0	618.0	620.0	0.16	0.49
heptamethylnonane	520.0	551.5	543.5	6.06	4.52
2-methylheptadecane	584.3	582.0	589.0	0.40	0.80
n-butylcyclohexane	456.2	454.3	453.3	0.42	0.64
1,3,5-triisopropylcyclohexane	523.2	557.0	566.0	6.46	8.18
trans-decalin	460.5	459.3	461.3	0.26	0.17
perhydrophenanthrene	546.9	534.0	569.0	2.36	4.04
1,2,4-trimethylbenzene	442.6	442.0	443.0	0.14	0.09
1,3,5-triisopropylbenzene	509.5	553.5	572.0	8.64	12.3
tetralin	480.9	480.0	481.0	0.19	0.02
1-methylnaphthalene	518.0	516.4	506.4	0.31	2.24

Table 2.4: Comparison between the experimental normal boiling temperatures, i.e. at 0.1MPa, and the prediction values calculated by LC- and GC-PC-SAFT EoS. The percent errors are equal to $100 \cdot \left|T_{b,calculated} - T_{b,experimental}\right| / T_{b,experimental} \cdot$

2.3.2 Density

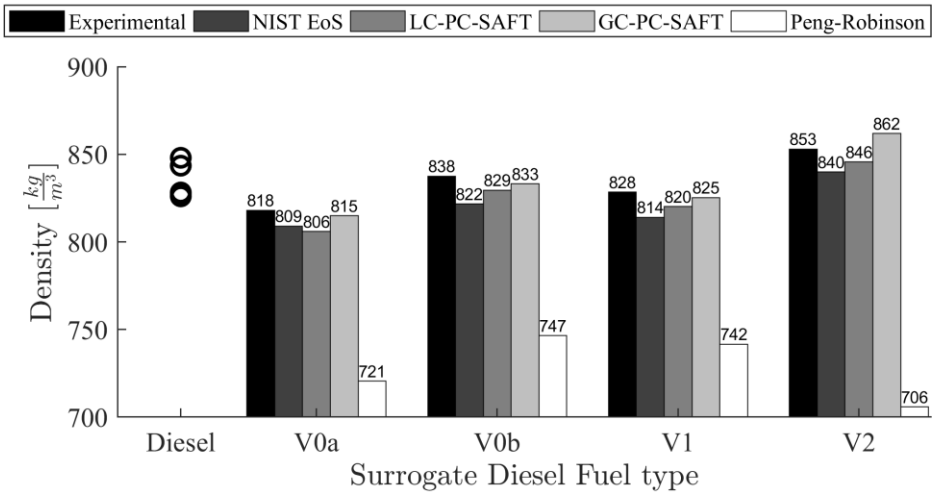

Figure 2.2: Comparison between experimentally measured surrogate densities at 293 K and 0.1 MPa [1] with predictions made with an EoS-based method developed at NIST[2], the two parameter sets of PC-SAFT and PR EoS. As a reference, the experimental densities of six Diesel fuels at 293K are shown as open circles[1, 3].

Figure 2.2 shows a comparison between the experimentally measured surrogate densities at 293K and 0.1 MPa with calculated densities using the EoS-based method developed at NIST[43], using the LC- and GC-PC-SAFT modelling methods, and using the widely known PR EoS. As a reference, the open circles in Figure 2.2 show the experimental densities for the six Diesel fuels [1, 3]. at the same condition. Note that the density of Diesel fuels falls into two distinct groups: fuels 1 through 4 originate from refineries and exhibit the lowest densities and fuels 5 and 6, retail and certification fuels, respectively, exhibit higher densities. Overall, the GC-PC-SAFT method gives the closest agreement to surrogate experimental densities, followed by the LC-PC-SAFT method, then the NIST EoS method and lastly, by a large margin, the PR EoS. Table 2.5 shows the PR EoS pure component parameters used for these calculations. The discrepancies between both PC-SAFT methods with the experimental data are due to the differences in the pure component and mixture parameters. Nevertheless, at this single temperature and pressure both PC-SAFT calculation methods are within 1.5% of experimental values, with the closest result of 0.37% for the density of V0a. These are strictly predictive calculations since

the binary interaction parameters shown in equation 2.13 are set to zero and, likewise, the binary interaction parameters used in the mixing rules with the PR EoS are also set to zero.

	Peng Robinson parameters			
Compound	$\mathrm{T_c}[\mathrm{K}]$	$p_\mathrm{c}[MPa]$	$\omega[-]$	$\mathrm{Z_c}\ [-]$
n-hexadecane	723.0	1.400	0.747	0.241
n-octadecane	747.0	1.290	0.800	0.247
n-eicosane	768.0	1.070	0.876	0.199
heptamethylnonane	693.0	1.570	0.548	0.245
2-methylheptadecane	739.3	1.159	0.727	0.196
n-butylcyclohexane	667.0	2.570	0.534	0.417
triisopropylcyclohexane	685.0	1.653	0.534	0.234
trans-decalin	687.0	3.200	0.274	0.269
perhydrophenanthrene	795.0	2.543	0.554	0.265
1,2,4-trimethylbenzene	649.1	3.200	0.274	0.269
1,3,5-triisopropylbenzene	706.0	1.743	0.554	0.235
tetralin	720.0	3.650	0.304	0.249
1-methylnaphthalene	772.0	3.600	0.348	0.259

Table 2.5: Properties of pure components within the surrogates for Peng-Robinson EoS. Taken from[8].

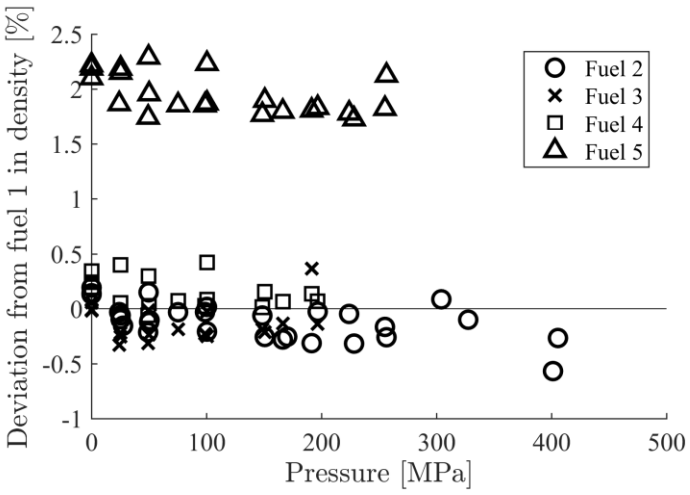

Figure 2.3: Deviation of the densities of fuels 2 through 5 with respect to the density of fuel 1. These comparisons cover a temperatures from 298 to 373K. The experimental densities exhibit an uncertainty of 0.2%[4]. The percent deviations are equal to $100 \cdot (\rho_{fuel\ i} - \rho_{fuel\ 1})/\rho_{fuel\ 1}$

Unfortunately, high pressure surrogate mixture densities are not available for comparison to the densities of the fuels. However, before comparing calculated and experimental high-pressure fuel densities, it is worthwhile comparing experimental densities of fuels 1 through 5 to ascertain which fuel densities can be grouped and which ones should be considered separately. Figure 2.3 shows the deviation of the experimental densities of fuels 2 through 5 with respect to the experimental density of fuel 1. The reported experimental uncertainty is 0.2% for all these five fuels. The densities of fuels 1 through 4 agree with one another to within 1.0% while the densities for fuel 5 consistently vary by ~2% regardless of the temperature. Therefore, fuels 1 through 4 will be considered collectively as a single group and fuel 5 will be considered on its own.

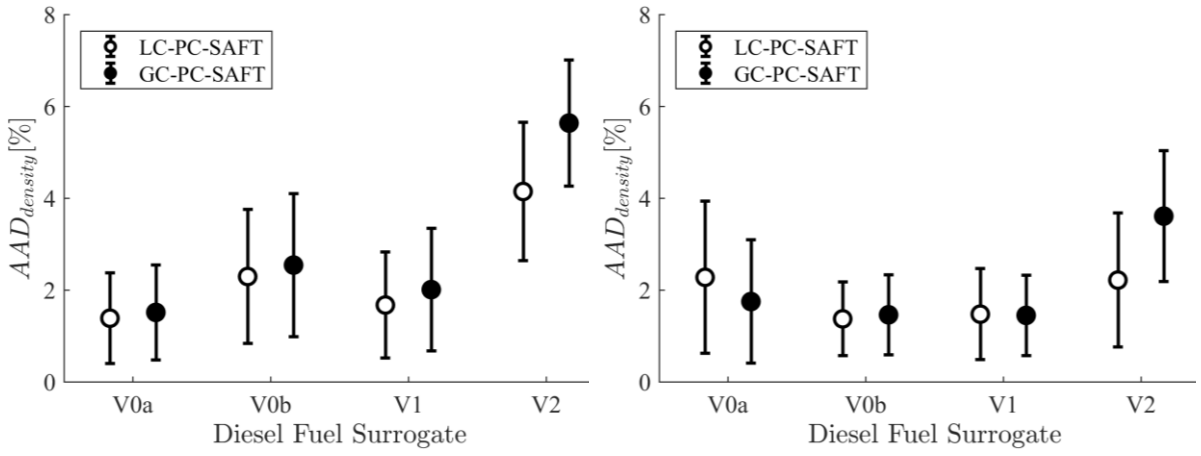

(a) Fuels 1 – 4 (b) Fuels 5

Figure 2.4: Average Absolute Deviation (AAD) showing the comparison of LC and GC-PC-SAFT predicted densities of the four surrogates with the fuel densities[3] for temperatures from 298 to 373 K and pressures from 0.1 to 500 MPa. Error bars represent one standard deviation.

The LC and GC-PC-SAFT methods are used to predict the densities of the four surrogate mixtures at 298, 323, 348, and 373 K and pressures from 0.1 to 500 MPa, conditions similar to those used to measure densities of fuels 1 through 5[3]. As the NIST-based EoS is unavailable and the Peng-Robinson EoS significantly underperforms in predictions, both are not taken into account for the rest of this section. Figure 2.4 shows AAD values for the experimental densities of the fuels compared to predicted surrogate densities. The densities of fuels 1 through 4 are, overall, better predicted with the LC-PC-SAFT than the GC-PC-SAFT method. The closest agreements are found with the LC-PC-SAFT method with surrogates V0a (1.5%) and V1 (1.8%). The AAD values for fuels 1 through 4 are all less than 8% for the remaining comparisons of the LC- and GC-PC-SAFT methods and surrogates. Interestingly, both methods match the density of fuel 5 equally well. The largest AAD values for all five fuels are found with calculated densities of surrogate V2 regardless of the parameter set used for the calculation. Nevertheless, overall, none of the surrogate calculated densities results in an AAD larger than ~6%.

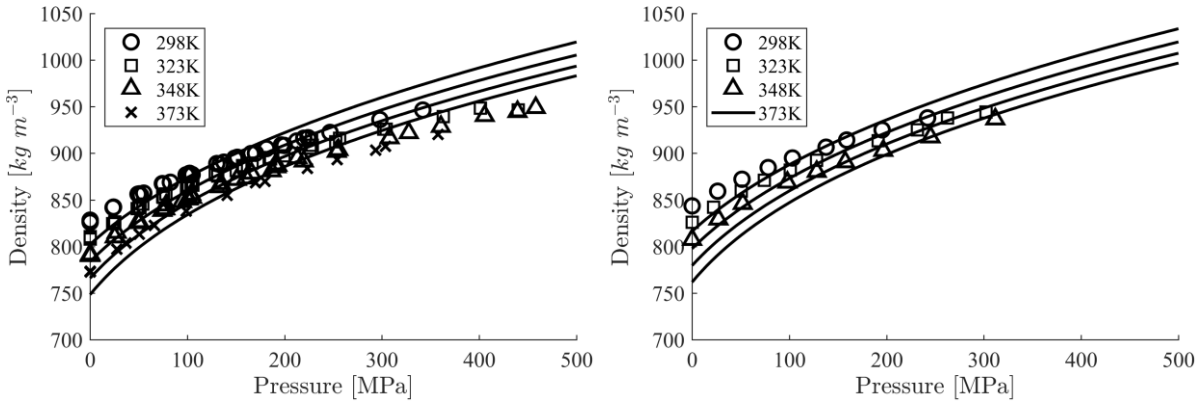

(a) V0a (LC-PC-SAFT) against Fuels 1-4 (b) V1 (LC-PC-SAFT) against Fuel 5

Figure 2.5: Surrogate densities calculated with LC-PC-SAFT (lines) compared to experimental densities (symbols)[3].

Figure 2.5 shows a comparison of predicted surrogate densities with experimental fuel densities of (a) fuels 1 through 4 against densities for V0a calculated with the LC-PC-SAFT method and (b) fuel 5[3] against densities for V1 also calculated with the LC-PC-SAFT method. Plots for the other surrogates and parameter sets are found in the Appendix A. For both cases, the predicted surrogate densities are slightly lower than the Diesel densities at all temperatures at low pressures and greater than the Diesel densities at all temperatures at high pressures. This trend is observed regardless of the chosen surrogate. Nevertheless, the maximum deviations are less than 4% at the upper limit of the pressure. However, the greatest discrepancy noted in these comparisons is that slopes of the predicted isotherms are not in agreement with the slopes of the experimental data. Hence, predicted isothermal compressibility will be in significant disagreement with experimental values.

2.3.3 Volatility

Figure 2.6 shows the predicted volatility curve at 0.1MPa for all four surrogates, calculated with LC-, GC-PC-SAFT and PR EoS, against the experimental curves for both the surrogates and fuel 6. It is obvious that PR EoS estimations are in greater disagreement with experimental data than both methods of PC-SAFT. As expected, the boiling temperatures increase with increasing vapour fraction

as heavier hydrocarbons remaining in the liquid phase require more energy and, hence, higher temperatures, to vaporise.

At vapour fractions up to ~10% the PC-SAFT approach, with either method used to calculate pure component parameters, overpredicts the surrogate boiling temperatures by as much as $5^{o}C$ while at vapour fractions greater than 60% this model underpredicts boiling temperatures. At vapour fractions greater than 80%, estimations for the “high accuracy” surrogates are a very poor match, where the deviation is close to $40^{o}C$ at a vapour fraction of 90%.

Similar conclusions are evident for the comparison of calculated surrogate vapour fractions with those for fuel 6, where a significant error close to complete vaporisation is also observed.

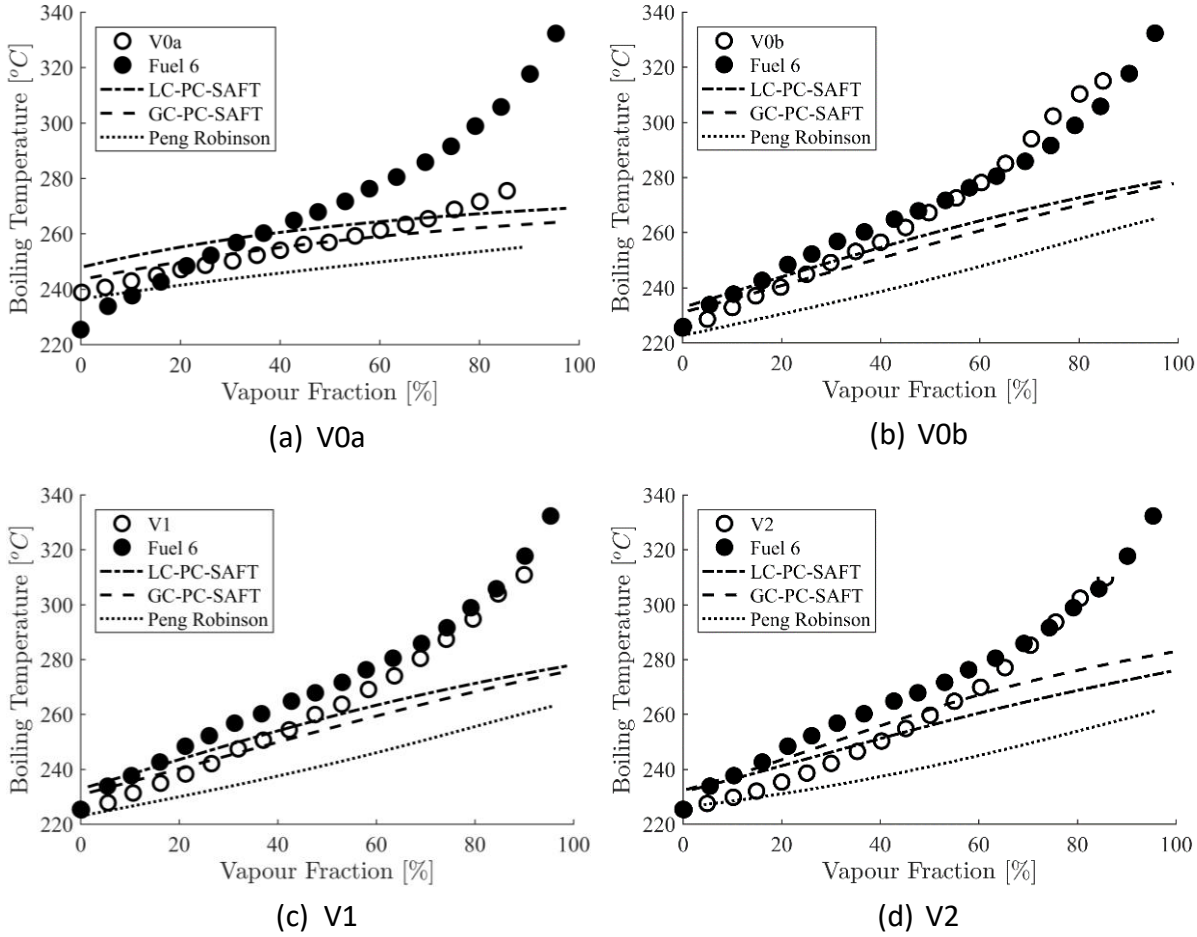

Figure 2.6: Volatility curves at 0.1MPa predicted by the PC-SAFT and PR EoS compared to experimental data for both surrogates and Fuel 6.

Figure 2.7 presents *AAD* values for experimental volatility curves at a constant pressure of 0.1 MPa for the four Diesel fuel surrogates [1] and that of fuel 6[1], compared to predictions using the LC-PC-SAFT and GC-PC-SAFT methods, i.e. *AAD* values for the results shown in Figure 2.6. Peng-Robinson estimations are omitted as they are clearly in greater disagreement than those of PC-SAFT. Both PC-SAFT parameter sets provide very similar boiling temperature estimates in close agreement to experimental values for all four surrogates, as shown in Figure 2.7a, particularly for V0a (1.4 - 2.3%).

The comparison against real Diesel volatility, Figure 2.7b, shows the LC-PC-SAFT estimates using V0b (5.9%), V1 (6.2%) and V0a (6.3%) are closer to experimental values than those obtained with the GC method. Conversely, the GC-PC-SAFT estimates using V2 (5.3%) are closer to real Diesel data than

those obtained with the LC method. Overall, the averaged errors for all surrogates by either method are within ~10% of the observed values.

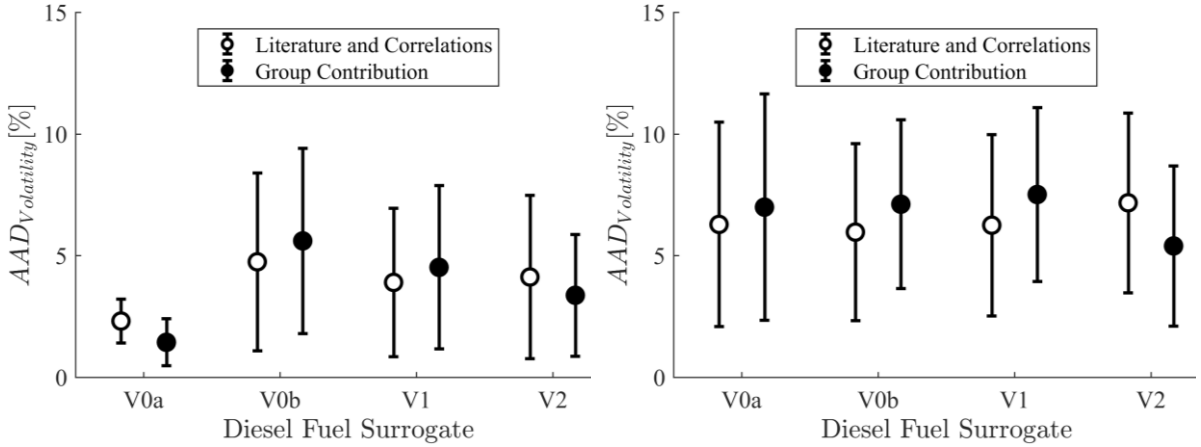

(a) Against surrogate data (b) Against Diesel data

Figure 2.7: Average Absolute Deviation ($AAD_{Volatility}$) for experimental boiling temperatures of four surrogates and Fuel 6[1] at 0.1 MPa with predictions using the LC-PC-SAFT and GC-PC-SAFT calculation methods. Error bars represent one standard deviation.

2.3.4 Viscosity

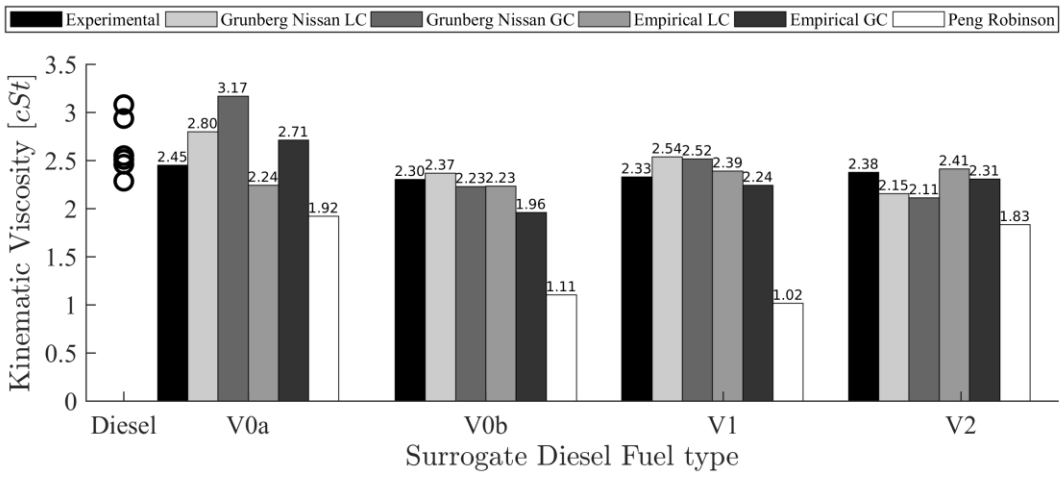

Figure 2.8: Comparison of experimental kinematic viscosities of four surrogates at 313.15 K and 0.1 MPa [5] to predictions using PC-SAFT with both parameter sets and mixing rules, and Peng Robinson[6]. As a reference, the open circles show the experimental kinematic viscosities of the six Diesel fuels at the same condition[3] [1] considered in this study. Units: 1cSt=10^{-6} m^2 s^{-1}

Figure 2.8 presents a comparison of experimental kinematic viscosity at 0.1 MPa and 313 K for the four surrogates[1] to those estimated by PR[6] and the PC-SAFT with both the LC and GC pure component parameters. Mixture viscosities are calculated with PC-SAFT using both the empirical (EM) mixing rule in Equation (2.22) and the Grunberg-Nissan (GN) mixing rule in Equation (2.21). On the other hand, only GN is applied to PR-EoS estimations in absence of any better alternative. For most cases the GC-PC-SAFT model with the EM mixing rule gives the closest predictions to surrogate experimental values with errors of 8.6% for V0a, 2.6% for V1, and 1.5% for V2. Predictions of the V0b kinematic viscosity with either the LC or GC-PC-SAFT method with the EM mixing rule give similar matches to the experimentally observed value. Peng-Robinson fails to provide accurate estimations, with errors ranging 20 to 60%. Thus, the results provided by the Peng-Robinson EoS are omitted in the rest of this

section. Moreover, overall viscosity predictions using the empirical mixing rule shown in Equation (2.22) provide slightly better matches with experimentally-observed values compared to predictions using the Grunberg-Nissan (GN) mixing rule, Equation (2.21). While it is possible to adjust the GN rule with a mixture-specific correction factor[146], this was not done to maintain fidelity with the decision to set binary interaction correction factors to zero in the PC-SAFT EoS mixing rules. Given that the empirical mixing rule, Equation (2.22), is computationally easier to use compared to the GN rule, the remaining mixture viscosity calculations are done with the EM mixing rule.

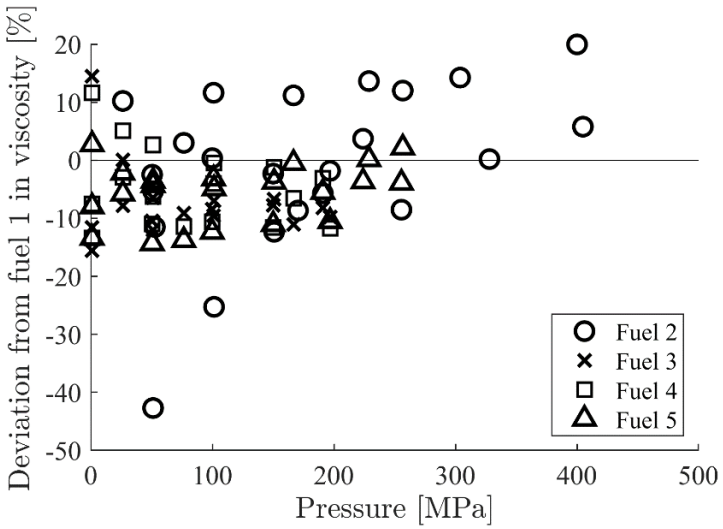

Figure 2.9: Deviation in viscosity of fuels 2 through 5 relative to the viscosity of fuel 1[4]. These comparisons cover a temperature from 298 to 373K. The uncertainty in the experimental viscosity is 2%. The percent errors are equal to $100 \cdot \left(\mu_{fuel\ i} - \mu_{fuel\ 1}\right)/\mu_{fuel\ 1}$

Before comparing calculated and experimental high-pressure fuel viscosities, it is worthwhile comparing experimental viscosities of fuels 1 through 5 to ascertain which fuel viscosities can be grouped and which ones should be considered separately, similar to the analysis performed with the fuel density data. Figure 2.9 shows a deviation plot comparing the viscosity of fuel 1 to the viscosity of fuels 2 through 5. The reported experimental uncertainty is 2%. The bulk of the viscosity data deviation for the different fuels falls within a range of ± 15%, which is much larger than the experimental uncertainty in the data. The large variation in viscosities is likely a consequence of the use of additives in fuels 2 through 5. Interestingly, these additives have very little effect on the density

of the fuels as previously shown in Figure 2.3. Note that additised fuel 2 exhibits the highest deviations and, therefore, the viscosity of fuel 2 is compared separately to the viscosity of the surrogates.

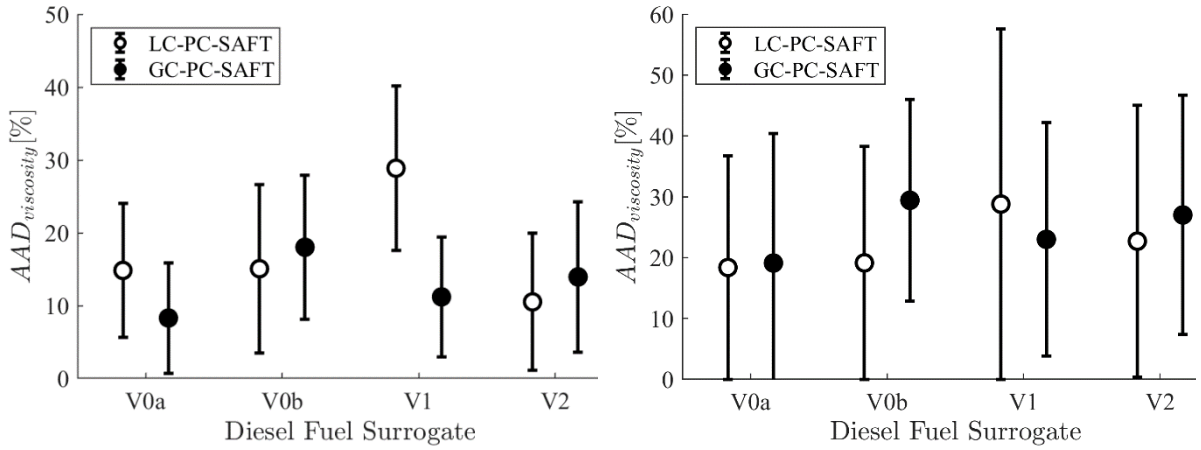

(a) Fuels 1, 3, 4, and 5 (b) Fuel 2

Figure 2.10: Average Absolute Deviation (*AAD*) showing how closely the entropy scaling predicted viscosities of the four surrogates match experimental viscosities averaged from Diesel fuels [3] for temperatures from 298 to 373 K and pressures from 0.1 to 500 MPa. The predictions use the empirical mixing rule defined in equation 2.21. Error bars represent one standard deviation.

Figure 2.10 compares dynamic viscosities averaged from fuels 1, 3, 4, and 5 (2.10a) and from fuel 2 (2.10b) [3]obtained at 298, 323, 348, and 373 K and pressures from 0.1 to 500 MPa to predicted surrogate viscosities over the same temperature-pressure ranges. Similar to the comparison of kinematic viscosity at low pressure, both parameter sources give similar predictions, with the exception of V1 calculated with LC-PC-SAFT. As shown, the errors for fuel 2 are greater than those for the other fuels, and in many cases the errors for fuel 2 are twice as large.

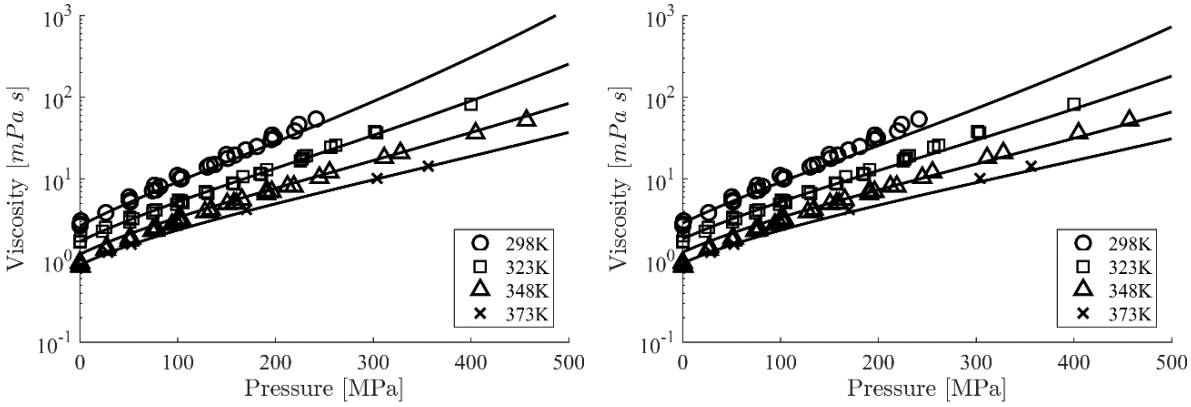

(a) V0a (GC-PC-SAFT) (b) V2 (LC-PC-SAFT)

Figure 2.11: Comparison of averaged experimental viscosities for fuels 1, 3, 4, and 5[3] to those predicted by PC-SAFT. The calculation uses the empirical mixing rule defined in equation (2.21).

A detailed viscosity comparison is provided in Figure 2.11 which shows predictions for V0a (GC-PC-SAFT) and V2 (LC-PC-SAFT) against averaged experimental data for fuels 1, 3, 4, and 5[3]. Plots for the other surrogates and both parameter sources are found in the Appendix A. Both the predicted and experimental viscosities increase with increasing pressure although the rate decreases as temperature increases. The predicted surrogate viscosities are in reasonably good agreement with experimental values for these retail Diesel fuels at most conditions. The largest increase in viscosity observed experimentally is at low temperatures and high pressures. It is in this region, at 298 K, where the disagreement between data and prediction is as high as 15%. This mismatch in viscosities at low temperatures and high pressures is characteristic of most viscosity models[149].

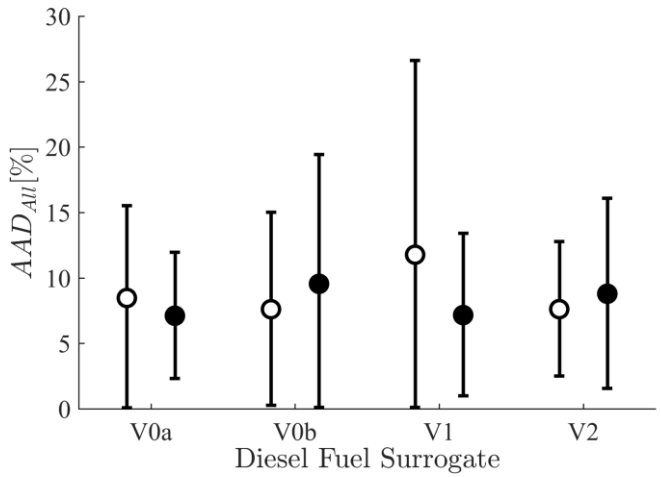

Figure 2.12: Average Absolute Deviation (AAD_{all}) showing the performance of four different surrogates to match the combined set of density, volatility, and viscosity data for six different Diesel fuels at temperatures from 298 to 373 K and pressures from 0.1 to 500 MPa. Error bars represent one standard deviation.

Although it is possible to match each thermodynamic and thermophysical property of Diesel fuel with a unique surrogate mixture, the normal practice is to use a small number of surrogate mixtures, if not just one mixture, to mimic all of the properties of a Diesel fuel. Figure 2.12 shows an assessment of how closely a combined set of Diesel fuel density, volatility, and viscosity data for six different Diesel fuels[5] at 298 to 373 K and 0.1 to 500 MPa match with each surrogate mixture considered in this study. For the calculation of these errors, each property contributes in the same amount to the total error. When a combined set of Diesel fuel properties are considered, it is evident that neither modelling option considered in this study is favoured. The lowest AAD_{all} is found for surrogate V1 (GC-PC-SAFT calculations) (7.1%), followed by V0a (GC-PC-SAFT calculations) (7.1%) and V2 (LC-PC-SAFT calculations) (7.6%) . AAD_{all} values for the rest of predictions, although larger, are still less than ~10% with the exception of V1 (LC-PC-SAFT calculations) with a deviation of ~11.7%.

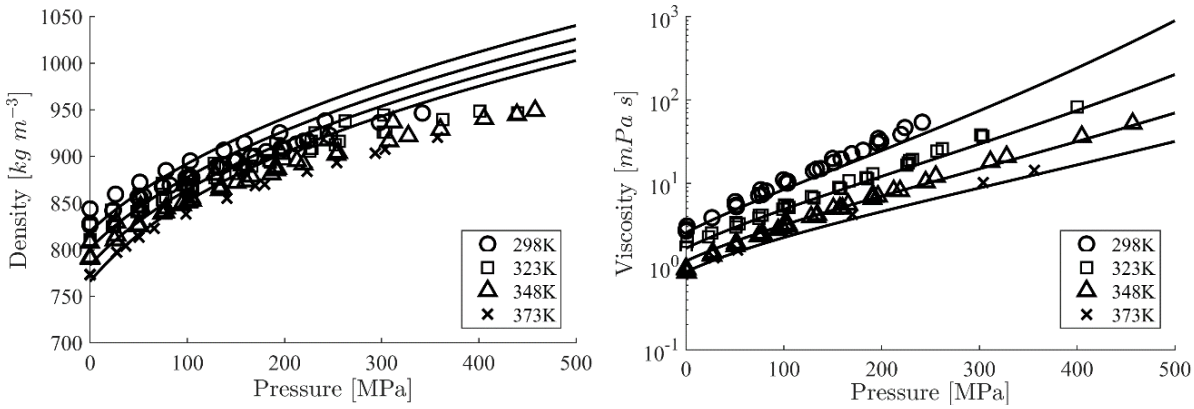

(a) Density (b) Viscosity

Figure 2.13: Isotherms for surrogate V1 calculated with the GC-PC-SAFT method compared to experimental data for Diesel fuels 1 through 6.

The combined GC-PC-SAFT predicted properties for the V1 surrogate had the best match to the studied Diesel fuel properties. Figure 2.13 (a) and (b) show how well the predicted V1 properties match the densities and viscosities of fuels 1 through 6. As shown in Figure 2.13 (a), the observed averaged Diesel density is underpredicted at low pressures and overpredicted at high pressures. However, these errors are within a maximum of ~3%. For viscosity, although it should be largely better than PR EoS, there is an important underprediction at low temperatures with errors as high as ~15%. Regarding volatility, as shown previously in Figure 2.6, the predictions overestimate the data at low vapour fractions and underestimate the data at high vapour fractions, with a maximum deviation of ~40 ^{o}C at a vapour fraction of 95%.

2.4 Conclusions

The properties of four surrogates proposed by Mueller, et al. were modelled using the PC-SAFT EoS to test the performance of this model to predict density, volatility, and viscosity. The PC-SAFT pure component parameters for the compounds in each surrogate mixture were obtained either from the literature or were calculated using correlations based on literature parameters (LC-PC-SAFT) or were calculated using a group contribution method (GC-PC-SAFT). Predicted surrogate mixture properties

were then compared to available property data for Diesel fuels. Both methods provided good predictions for the densities of the four surrogate mixtures. Likewise, the predicted surrogate mixture densities were in reasonably close agreement with Diesel fuel density reported over broad temperature and pressure ranges. Both methods also exhibited similar deviations for predicted normal boiling points for the surrogates and both methods exhibited similar trends in the distillation curves where predicted temperatures were too high at low vapour fractions and too low at high vapour fractions. High temperature, high pressure predicted surrogate viscosities obtained with the entropy scaling viscosity model matched Diesel experimental data within ~15% when using either the LC and GC parameter estimation techniques. Comparisons are also presented for calculations with both the PC-SAFT and PR EoS, showing the greater performance of the PC-SAFT EoS. Overall, the V1 surrogate modelled with the GC-PC-SAFT method, with an *AAD* of 7.1%, provided the best match of Diesel properties when a combination of Diesel properties was considered. This deviation from experimental results show the predictive capability of the PC-SAFT equation of state for Diesel fuels at a wide range of operating conditions, from 298K to 373K and from 0.1MPa up to 500MPa.

3. Vapor-Liquid Equilibrium calculations at specified composition, density and temperature with the Perturbed Chain Statistical Associating Fluid Theory (PC-SAFT) Equation of State

In this study, the PC-SAFT equation of state is used for vapour-liquid equilibrium calculations using as independent variables the mixture composition, density and temperature. The method is based on unconstrained minimisation of the Helmholtz Free energy via a combination of the successive substitution iteration and Newton-Raphson minimisation methods with line-search; the positive definiteness of the Hessian is guaranteed by a modified Cholesky decomposition. The algorithm consists of two stages; initially, the mixture is assumed to be a single-phase and its stability is assessed; in case of being found unstable, a second stage of phase splitting (flash) takes place, in which the pressure of the fluid and compositions of both the liquid and vapor phases are calculated. The reliability of two different methods presented in the existing literature, (i) using mole numbers and (ii) using the logarithm of the equilibrium constants as iterative variables, is evaluated in terms of both iterations and computational time needed to reach convergence, for seven test cases. These include both single and multicomponent Diesel fuel surrogates, known to give incomplete density information when using pressure and temperature as independent variables. Pressure and vapor volume fraction fields are discussed for a range of temperatures and densities, apart from the number of iterations needed during the flash calculation stage. A performance comparison is obtained against the Peng-Robinson equation of state.

3.1 Numerical method

This work is supported by public funding of the European Commission. As such, the complete algorithm described in the following sections is available upon request.

Any isolated system at constant density and temperature tends spontaneously to an equilibrium state while decreasing the Helmholtz free energy of the system, until the global minimum is reached, i.e. equilibrium. The Helmholtz free energy of the system can be calculated as

$$A(\boldsymbol{z},\rho,T) = \sum_{i=1}^{nc} z_i A_i^{id}(P(\boldsymbol{z},\rho,T),T) \; + \; A^{res}(\boldsymbol{z},\rho,T) \tag{3.1}$$

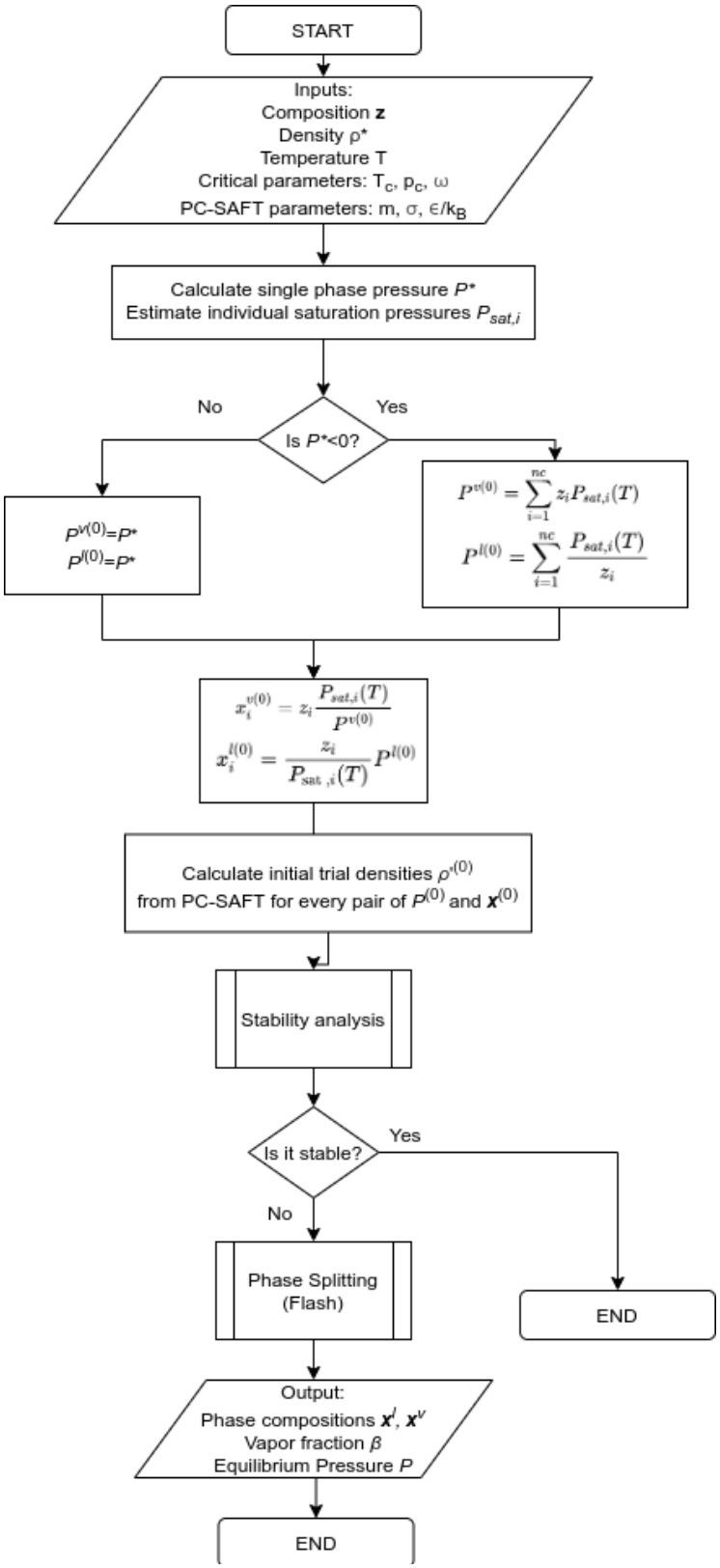

Scheme 3.1. General diagram for multiphase calculations

However, it may be the case that the state at which the equilibrium occurs is that of vapor and liquid coexisting. Thus, the amount of each phase, their composition and pressure need to be calculated. In this work, the presented algorithm studies the stability of the homogeneous mixture using the PC-SAFT EoS for a given composition $z_1,...,z_{nc}$ with density ρ and at a certain temperature T; in case it is found to be unstable, the vaporized fraction of the substance, the compositions of both phases and the resulting pressure in equilibrium are calculated via flash.

Both algorithms for the stability and flash stages have been already developed and published for the Peng Robinson EoS; only minor changes are needed for the PC-SAFT EoS regarding the convergence criteria in the iterations and constraints. Scheme 3.1 shows the

general diagram of the algorithm used in the multiphase calculations. For consistency, the whole algorithm is described here, and any novelty introduced is clearly stated in the following subsections.

3.1.1 Newton method

The Newton method [150] provides a good approximation for the root of an objective function. Essentially, the independent variables vector $\boldsymbol{\epsilon}$ of the objective function is iteratively updated from step *k* to the following *k* + 1 by

$$\boldsymbol{\epsilon}^{(k+1)} = \boldsymbol{\epsilon}^{(k)} + \lambda \boldsymbol{p}^{(k)} \tag{3.2}$$

where λ is the step length, which defines how far the next step moves along the Newton direction $\boldsymbol{p}^{(k)}$. The step length is set in two stages. First, an initial value of 1 is given and it is continuously halved until $\boldsymbol{\epsilon}^{(k+1)}$ satisfies the variable constraints of each problem, specified in the following sections. These constrains may be related, for instance, to the feasible values of density or compositions. Then, an inexact line search is executed to obtain a step length that satisfies the Wolfe conditions[133], which gives an efficient decrease of the objective function.

The Newton direction $\boldsymbol{p}^{(k)}$ is calculated by solving the system of equations:

$$\boldsymbol{H}^{(k)}\boldsymbol{p}^{(k)} = -\boldsymbol{g}^{(k)} \tag{3.3}$$

where ***g*** and ***H*** are the gradient and Hessian of the objective function to be minimised. In case the use of successive substitution iterations (SSI) method is needed, the only difference with the Newton method is that the Hessian is equal to the identity matrix ***I***.

For the system (3.3) to have a solution, the Hessian ***H*** needs to be positive definite, i.e. its eigenvalues are all positive real numbers. To satisfy this condition, the modified Cholesky factorisation[82] is applied in this study. The modifications introduce symmetric interchanges of rows and columns, via a permutation matrix ***P***, and the addition of a non-negative diagonal matrix ***E*** which is zero if the Hessian ***H*** is positive. Therefore, the system of equations (3.3) gets transformed, for every iteration step *k*, into:

$$[\boldsymbol{P}(\boldsymbol{H} + \boldsymbol{E})\boldsymbol{P}^T](\boldsymbol{P}\boldsymbol{p}) = -\boldsymbol{P}\boldsymbol{g} \tag{3.5}$$

Once the positive definiteness of the modified Hessian is satisfied, it is factorised as:

$$\boldsymbol{P}(\boldsymbol{H} + \boldsymbol{E})\boldsymbol{P}^T = \boldsymbol{M}\boldsymbol{M}^T \tag{3.6}$$

where $\boldsymbol{M}$ is a lower triangular matrix. Finally, the system is solved by performing backward and forward substitution with the triangular matrix, which consists in the following sequence of operations:

1. Solve $\boldsymbol{Mu} = -\boldsymbol{Pg}$ to obtain $\boldsymbol{u}$.
2. Solve $\boldsymbol{M^T}\tilde{\boldsymbol{u}} = \boldsymbol{u}$ to obtain $\tilde{\boldsymbol{u}}$.
3. Calculate the gradient $\boldsymbol{g} = \boldsymbol{P^T}\,\tilde{\boldsymbol{u}}$.

Convergence criteria

The Newton method is assumed to have converged whenever one of the following criteria is achieved:

1. The Euclidean norm of the change in the iteration variables $\|\lambda \boldsymbol{p}\|^2$ is less than 10^{-7}.
2. The Euclidean norm of the gradient $\|\boldsymbol{g}\|^2$ is less than 10^{-10}.

3.1.2 Stability stage

The stability problem is solved in a similar fashion as that presented by Baker et al.[132] for a mixture at constant temperature *T* and pressure *P*. A homogeneous mixture at a certain temperature *T* is in a stable state if the tangent plane to the Helmholtz free energy surface at composition *z* and density *ρ* does not intersect the Helmholtz free energy surface at any other point. The stability is tested by purposely dividing the homogeneous mixture in two phases, one of them in an infinitesimal amount and it is referred to as 'trial phase'. For any feasible two-phase mixture, if a decrease in the Helmholtz free energy is not achieved, then the mixture is stable. The so-called tangent plane distance (*TPD*) as function of the density times the composition of the trial phase $\rho' x_i{}'$ is:

$$TPD(\rho' x_i') = -\frac{P'-P^*}{R_g T} + \sum_{i=1}^{nc} \rho' x_i' (log\, f_i' - log\, f_i^*) \tag{3.7}$$

where the tildes over the variables indicate those calculated at the trial conditions and the asterisk indicates those calculated at the feed conditions. R_g is the universal gas constant and f_i is the fugacity

of the component *i*. Within the structure of PC-SAFT, it is advisable to write the expression in terms of the residual reduced Helmholtz free energy, having then:

$$P = \left(1 + \rho_m \frac{\partial a^{res}}{\partial \rho_m}\right) k_B T \rho_m \left(10^{10} \frac{\text{Å}}{m}\right)^3 \tag{3.8}$$

Where ρ_m is the number density of molecules and k_B is the Boltzmann constant. Regarding the fugacity,

$$log\, f_i \;\; = log(x_i P \phi_i) \tag{3.9}$$

Where the logarithm of the fugacity coefficient ϕ of the component i is defined as:

$$log\phi_i = \frac{1}{R_g T}\left(\frac{\partial A^r}{\partial N_i}\right)_{T,V,N_s \neq i} - \log Z \tag{3.10}$$

where Z is the compressibility factor and A^r is the non-reduced Helmholtz free energy. This equation is used for the Peng Robinson EoS following the formulation of Nichita[77]. For PC-SAFT, the original formulation of Gross and Sadowski[49] is used:

$$log\, \phi_i = a^{res} + \rho_m \frac{\partial a^{res}}{\partial \rho_m} + \frac{\partial a^{res}}{\partial x_i} - \sum_{j=1}^{nc} x_j \frac{\partial a^{res}}{\partial x_j} \tag{3.11}$$

The derivation of the TPD function can be seen in the work of Mikyska and Firoozabadi[151]. The stability is assured if for any feasible solution $\rho' x_i'$ the TPD function is non-negative. Therefore, the problem is reduced to the search of the global minima of the TPD function, subjected to the material constraints:

$$\rho' x_i' > 0 \quad \forall i \tag{3.12}$$

$$\sum_{i=1}^{nc} \rho' x_i' \leq \rho_{max}(x_i', T) \tag{3.13}$$

where ρ_{max} refers to the maximum packing fraction at fixed composition x_i' and temperature *T*. For the Newton method, the required gradient is given by:

$$\frac{\partial TPD}{\partial(\rho' x_i)} = log\, f_i' - log\, f_i^* \tag{3.14}$$

Nichita [152] studied alternatives to use as iteration variables such as $\log(\rho' x_i')$ and $\alpha_i = 2\sqrt{\rho' x_i'}$, in a similar manner as shown by Michelsen[72]. His study concluded that the α_i ensured the most robust and fast convergence for the stability problem and it is the one used in this work. For this case, the gradient is:

$$\frac{\partial TPD}{\partial \alpha_i} = \sqrt{\rho' x_i}(\log f_i' - \log f_i^*) \tag{3.15}$$

and the Hessian is:

$$\frac{\partial TPD}{\partial \alpha_i \, \partial \alpha_j} = \delta_{ij} + \sqrt{\rho' x_i}\sqrt{\rho' x_j}\left[\frac{\partial \log f_i}{\partial n_j} - \frac{\delta_{ij}}{\rho' x_i}\right] \tag{3.16}$$

In order to avoid unnecessary iterations when the Newton is converging to a trivial solution, i.e. *TPD* = 0, in this work another stopping criterion is used, also first introduced but for the TPN case by Michelsen[72]. At every iteration the convergence variable *r* is checked:

$$r = \frac{2\,TPD^{(k)}}{\sum_{i=1}^{nc}(\rho' x_i - \rho z_i)\left(\log f_i' - \log f_i^*\right)} \tag{3.17}$$

which tends to 1 as the method converges to the trivial solution. Therefore, the iterations are stopped if $|r - 1| < 0.2$ and $TPD^{(k)} < 10^{-3}$.

3.1.3 Initialisation

The stability stage needs an initial condition to start the iterative process. Tipically, Wilson's correlation [153] is used to guess the initial equilibrium constants K_i:

$$K_i = \frac{P_{c,i}}{P}\exp\left[5.37(1 + \omega_i)\left(1 - \frac{T_{c,i}}{T}\right)\right] \tag{3.18}$$

where for every component *i*, $P_{c,i}$ and $T_{c,i}$ are the critical pressure and temperature and ω_i is the acentric factor. These three values are used in most cubic EoS and are widely available in the literature, but not in PC-SAFT EoS. However, the exact critical values specific for the PC-SAFT EoS can be calculated following a published algorithm[154], which comprises an iterative process in order to verify the three critical specifications:

$$P(T_c, \rho_c) - P_c = 0 \tag{3.19}$$

$$\frac{\partial P}{\partial \rho} = 0 \text{ at } (T_c, \rho_c) \tag{3.20}$$

$$\frac{\partial^2 P}{\partial \rho^2} = 0 \text{ at } (T_c, \rho_c) \tag{3.21}$$

Unlike for the PT-multiphase problem, the pressure of the mixture is unknown a-priori for VT specifications, so a different strategy must be used, as the one used by Nichita[152]. According to Raoult's law:

$$K_i = \frac{P_{sat,i}(T)}{P} \tag{3.22}$$

where $P_{sat,i}(T)$ is the saturation pressure of the component *i* at a temperature *T*. From this law, follows that $P_{sat,i}(T) = P$ when $K_i = 1$, therefore from eq. (3.18) it follows:

$$P_{sat,i}(T) = P_{c,i} \exp\left[5.37(1+\omega_i)\left(1-\frac{T_{c,i}}{T}\right)\right] \tag{3.23}$$

The strategy for the initial composition of the trial phase is slightly different if it is considered to be vapor-like or liquid-like. Michelsen [72] proposed the initial composition of the trial phase, for both cases, to be:

$$x_i^{v(0)} = z_i K_i^{(0)} \quad \text{and} \quad x_i^{l(0)} = \frac{1}{z_i K_i^{(0)}} \tag{3.24}$$

which, using Raoul's law (14) transform to:

$$x_i^{v(0)} = z_i \frac{P_{sat,i}(T)}{P^{v(0)}} \quad \text{and} \quad x_i^{l(0)} = \frac{z_i}{P_{sat,i}(T)} P^{l(0)} \tag{3.25}$$

where the initial pressures $P^{v(0)}$ and $P^{l(0)}$ are first taken as that given by the EoS for the single phase system at T, ρ and composition $\boldsymbol{z}$. If the calculated pressure is negative, Mikyska and Firoozabadi [151] estimated them as:

$$P^{v(0)} = \sum_{i=1}^{nc} z_i P_{sat,i}(T) \quad \text{and} \quad P^{l(0)} = \sum_{i=1}^{nc} \frac{P_{sat,i}(T)}{z_i} \tag{3.26}$$

The initial density of the trial phase is then calculated iteratively using the EoS for both initial compositions $x_i^{v(0)}$ and $x_i^{l(0)}$ at fixed temperature T and at the corresponding initial pressures $P^{v(0)}$ and $P^{l(0)}$. As there may be two densities for every composition and pressure, there can be up to 4 initial estimates; all the initial estimates are used in the stability stage.

3.1.4 Initial Phase splitting

In case the mixture is found to be unstable, an initial splitting of the homogeneous phase is executed. From the stability analysis, the composition and density of the trial phase are fixed to ρ' and x_i'. With variations with respect to the method shown by Jindrova and Mikyska[76], the initial density and composition of the second phase, i.e. ρ'' and x_i'', are estimated in terms of the molar fraction of the trial phase over the feed, $\beta = N'/N^*$, from the material and volume constraints:

$$\beta x_i' + (1-\beta)x_i'' = z_i \tag{3.27}$$

$$\beta \frac{1}{\rho'} + (1-\beta)\frac{1}{\rho''} = \frac{1}{\rho} \tag{3.28}$$

The initial amount of each phase is estimated in the following way:

1. An arbitrary initial trial molar fraction β is chosen. In two phase systems, $\beta \in (0,1)$, thus the chosen initial value in this work is 0.99.
2. The composition and density of the second phase are calculated from the material and volume constraints (3.27) (3.28) by:

$$x_i'' = \frac{z_i - \beta x_i'}{1-\beta} \tag{3.29}$$

and

$$\rho'' = \frac{1-\beta}{\frac{1}{\rho} - \beta\frac{1}{\rho'}} \tag{3.30}$$

3. The density of the second phase is checked to be lower than that given by the maximum packing fraction

$$\rho'' < \rho_{max}(x_i'', T) \tag{3.31}$$

If not, a new lower molar fraction value is assumed (i.e. halving the previous value), and the algorithm returns to step 2.

4. The variation in the Helmholtz free energy is calculated by:

$$\Delta A = A^{2\,phase} - A^* = \left(A'(\boldsymbol{x}', \rho', T) + A''(\boldsymbol{x}'', \rho'', T)\right) - A^* \tag{3.32}$$

5. It is checked whether $\Delta A < 0$, meaning that the current phase split produces a decrease in the Helmholtz free energy. If $\Delta A \geq 0$ the molar fraction is halved and step 2 is repeated. If $\Delta A < 0$ the process is stopped, and the flash stage begins. The phase with the highest density is considered to be the liquid phase (*l*) and the other one the vapor phase (*v*).

3.1.5 Flash stage

Following the initial phase splitting, the flash stage calculates the amount and compositions of both phases in equilibrium, in addition to the final equilibrium pressure. This calculation is done via the minimisation of the variation of the Helmholtz free energy, as in equation (3.32). Depending on the iteration variables, two methodologies have been tested. Firstly, the one described by Jindrova and Mikyska [83] uses the number of moles in both phases and the phase volumes. Secondly, the one described by Nichita [77] uses the natural logarithm of the equilibrium constants. The two methods have been coupled with the PC-SAFT framework and the derivatives needed can be found in the Appendix B.

Number of moles and volume as iteration variables

When using the number of moles and the volume of both phases, per mole of feed, the problem comprises (2 *nc*)+2 iteration variables $n_1^v, \dots, n_{nc}^v, V^v, n_1^l, \dots, n_{nc}^l, V^l$. However, because of the material and volume balances:

$$n_i^v + n_i^l = z_i \tag{3.33}$$

$$V^v + V^l = \frac{1}{\rho} \tag{3.34}$$

the variables of one phase are dependent on those of the other phase. Therefore, as described by Jindrova and Mikyska[83], it is possible to solve a reduced system in terms of the *nc*+1 vapor variables. For the reduced problem, the gradient of the system is given by:

$$g_i = \frac{\partial \Delta A}{\partial n_i^v} = \frac{\log f_i^v - \log f_i^l}{\sqrt{2}} \quad \text{for} \quad i = 1, nc \tag{3.35}$$

$$g_{nc+1} = \frac{\partial \Delta A}{\partial V^v} = -\frac{P^v - P^l}{\sqrt{2} R_g T} \tag{3.36}$$

and the Hessian:

$$\boldsymbol{H} = 1/2 \begin{pmatrix} & & & \vdots & \\ & \boldsymbol{B} & & \vdots & \boldsymbol{C} \\ & & & \vdots & \\ \cdots & \cdots & \cdots & \vdots & \cdots \\ & \boldsymbol{C}^T & & \vdots & D \end{pmatrix} \tag{3.37}$$

$$B_{ij} = \frac{\partial \log f_i^v}{\partial n_j^v} + \frac{\partial \log f_i^l}{\partial n_j^l} \tag{3.38}$$

$$C_i = -\frac{\frac{\partial P^v}{\partial n_i^v} + \frac{\partial P^l}{\partial n_i^l}}{R_g T} \tag{3.39}$$

$$D = -\frac{\frac{\partial P^v}{\partial V^v} + \frac{\partial P^l}{\partial V^l}}{R_g T} \tag{3.40}$$

In order to obtain the variation of the variables for both phases, the Newton direction *p* is transformed back into the full (2 *nc*)+2 dimension premultiplicating by the reducing matrix *Z:*

$$\boldsymbol{Z} = \frac{1}{\sqrt{2}} \begin{pmatrix} I_{nc+1} \\ -I_{nc+1} \end{pmatrix} \tag{3.41}$$

Finally, the composition and density of both phases are calculated by first obtaining the vapor mole fraction $\beta = \sum_{i=1}^{nc} n_i^v$ and then:

$$x_i^v = \frac{n_i^v}{\beta} \quad \text{and} \quad x_i^l = \frac{n_i^l}{1-\beta} \tag{3.42}$$

$$\rho^v = \frac{\beta}{V^v} \quad \text{and} \quad \rho^l = \frac{1-\beta}{V^l} \tag{3.43}$$

Following the work of Paterson et al.[78], the effect of initial Successive Substitution Iterations

(SSI)during the flash stage were tested. However, no improvement was observed and on average more iterations were needed to reach convergence.

Logarithm of equilibrium constants $\log K_i$ as iteration variables

The use of the logarithms of equilibrium constants, $\log K_i = \log(x_i^v / x_i^l)$, as iteration variables in the flash problem is one of the most used methods when the multiphase problem is defined in terms of pressure and temperature. Nichita [77] applied it to the VT-Flash problem by decoupling the pressure equality condition $P^v(x_i^v, \rho^v, T) = P^l(x_i^l, \rho^l, T) = P^{eq}$, which is calculated at every iteration step. Therefore, the iteration variables are reduced to the nc components defining $log\ \boldsymbol{K}$. Then, at every step the Rachford-Rice equation is solved to obtain the vapor mole fraction β using the Newton-Raphson method:

$$\sum_{i=1}^{nc} \frac{z_i(K_i-1)}{1+\beta(K_i-1)} = 0 \tag{3.44}$$

Which allows to obtain the molar fractions of both phases for every iteration k by:

$$x_i^l = \frac{z_i}{1+\beta(K_i-1)} \tag{3.45}$$

and

$$x_i^v = K_i x_i^l \tag{3.46}$$

Then, the equilibrium pressure P^{eq} is calculated iteratively by solving the volume distribution equation:

$$\beta \frac{1}{\rho^v(x_i^v, P^{eq}, T)} + (1-\beta)\frac{1}{\rho^l(x_i^l, P^{eq}, T)} = \frac{1}{\rho} \tag{3.47}$$

When calculating the density at certain pressure, many roots may be encountered. In such a case, the density giving the least Gibbs free energy is chosen. The iterative method chosen is that of Brent[155]. The gradient in this case reads:

$$\frac{\partial \Delta A}{\partial \log K_i} = \log f_i^v - \log f_i^l \tag{3.48}$$

and the Hessian:

$$H_{ij} = \frac{\partial \ log \ K_i}{\partial \ N_j^v} + \frac{\partial \ log \ f_i^v}{\partial \ N_j^v} + \frac{\partial \ log \ f_i^l}{\partial \ N_j^l} + \frac{1}{R_g \ T} \frac{\left(\frac{\partial \ P^v}{\partial \ N_i^v} + \frac{\partial \ P^l}{\partial \ N_i^l}\right)\left(\frac{\partial \ P^v}{\partial \ N_j^v} + \frac{\partial \ P^l}{\partial \ N_j^l}\right)}{\frac{\partial \ P^v}{\partial \ V^v} + \frac{\partial \ P^l}{\partial \ V^l}} \tag{3.49}$$

As proposed in the original paper of Nichita[77], a first iteration using the SSI method is applied.

3.2 Results and Discussion

In this section, results for the VLE problem using composition, density and temperature are shown for a set of seven cases. Case 1 is a single component Diesel surrogate, (n-dodecane) widely used in the Diesel industry; this case will show the performance of the algorithm for single components where the PT FLASH fails. Cases 2 and 3 are binary mixtures, typically used as benchmark cases for testing multiphase equilibrium algorithms[75]. The composition for Case 2 is 0.547413 methane and 0.452587 pentane, while for Case 3 is 0.547413 carbon dioxide and 0.452587 decane. Case 4 is another binary mixture used in the widely used database of the so-called 'Spray A'[156], 0.3 nitrogen and 0.7 dodecane. Case 5 is a four-component mixture, also widely used for testing of multiphase algorithms[75], composed of 0.2463 nitrogen, 0.2208 methane, 0.2208 propane and 0.3121 decane. Case 6 is a hydrocarbon eight-component mixture created also as a Diesel fuel surrogate[157], composed of 0.202 octadecane, 0.027 hexadecane, 0.292 heptamethylnonane, 0.144 1-methylnaphthalene, 0.154 tetralin, 0.055 trans-decalin, 0.051 butylcyclohexane and 0.075 1,2,4-trimethylbenzene. Finally, case 7 explores the application of the presented method to a multi-component mixture consisting of 50 different hydrocarbons, with equally distributed composition ranging from methane to octadecane. The complete set of hydrocarbons is given in the Appendix B. Cases 3 and 4 are validated against experiments, apart from an additional synthetic mixture of 6 components, commonly named Y8[158]. For all cases, the EoS parameters and binary interaction parameters are given in the Appendix B. Table

3.1 shows the density-temperature grids studied for each case, apart from the number of total points tested with the algorithms.

A summary of the iterations needed for convergence for every stage and flash methodologies used in this work can be found in Table 3.2. The average values are calculated as the sum of the iterations needed until convergence for the whole domain and then divided for the number of points studied. As seen in the first row, the stability analysis grows with the number the components of the mixture. While for a single component (Case 1), the number of iterations needed for convergence in stability is around 4, for binary mixtures (Cases 2-4), it increases to around 7. For the 4 components mixture (Case 5), the number of stability iterations needed are not much affected with respect to the binary mixtures. For the eight-component hydrocarbon mixture (Case 6), the average number of iterations needed grows around 50%. Finally, for the 50-component mixture (Case 7), the number of iterations is higher but close to the previous case.

Case	nc	T(K) window	T(K) no. points	ρ (Kmol/m^3) window	ρ no. points	Total no. points
1	1	[280-700]	400	[0.001-5]	400	160000
2	2	[320-430]	110	[0.001-12]	1200	132000
3	2	[250-600]	350	[0.001-9]	900	315000
4	2	[250-650]	400	[0.001-10]	900	360000
5	4	[250-600]	350	[0.001-12]	1200	420000
6	8	[300-750]	450	[0.001-4.5]	450	202500
7	50	[300-650]	400	[0.001-6]	400	160000

Table 3.1: Density-Temperature window and total number of points.

A case dependant result is found for the flash stage. For the NVL method (second row of Table 2), the binary mixture of Case 2 is the one with the lower number of flash iterations needed, followed by the single component Case 1 and the other two binary mixture Cases 3 and 4. A substantial increase

is found for the 4-component mixture, which almost triples the iterations needed for the binary mixtures. Although doubling the number of components in Case 6, for the 8-component the flash iterations gets reduced by 10 for the conditions to converge. Finally, the 50-component mixture shows a doubled number of iterations with respect to Case 6, needing on average around 30 iterations until convergence during the flash stage.

In the case of the lnK method (third row on Table 3.2), the number of iterations is significantly reduced by more than 40% with respect to the NVL method. However, as explained in the methodology section for the lnK independent variables, this method suffers from the same limitation of the PT-Flash problem and it can't be used for single components and mixtures of similar components, as Cases 1 and 6. Regarding the rest of cases, Case 2 is the one with the least iterations needed (up to 4), followed by the other binary mixtures Cases 4 and 3. For Case 5, the 4-component mixture needs between 3 and 4 times more iterations than for the binary mixtures. For the 50-component surrogate, the difference between the methods gets reduced to only 2 iterations less than those needed for the NVL-VLE algorithm.

	Case 1	Case 2	Case 3	Case 4	Case 5	Case 6	Case 7
Stability	3.93	7.63	6.26	6.87	11.25	15.31	17.82
Flash (NVL)	7.24	6.26	9.05	9.21	26.82	16.20	30.80
Flash (lnK)	-	3.99	5.32	4.24	15.12	-	28.33

Table 3.2: Average number of iterations needed for convergence using every method studied here for both the stability and flash algorithms.

Table 3.3 shows the average total convergence time, i.e. both stability and flash stages, for any ρ and T conditions, in ms. The CPU used during this study was an Intel(R) Xeon(R) CPU E5-2690 v3 at 2.60GHz and a memory of 128GB of RAM. From the number of iterations, it would seem clear that the lnK method was the best one to be used in processes needing fast but reliable calculations, such as those needed in CFD simulations. However, the time needed for convergence clearly points in the opposite way, as the lnK method lasts a minimum of 20 times longer than the time needed for convergence with the NVL. This difference in computational time is caused during the calculation of

density in the pressure equality condition, as it needs to be obtained iteratively, while NVL only satisfies it once convergence is reached. For the single component Case 1, the NVL method needed 0.6 ms, while no results could be obtained for the lnK method as it fails. For the binary mixtures (Cases 2-4), around 1 ms was needed for the NVL method against the 20-25ms for the lnK. The computational time needed for the 4-component mixture of Case 5 was around 5ms for the NVL method and 135ms for the lnK method (25 times longer). Case 6 needed 15.6 ms with NVL while the lnK method failed to converge to the correct solution whenever the phase transition was isobaric-isothermal. For the 50-components mixture of Case 7, each complete VLE calculation took close to 2 seconds, while for the lnK flash procedure it took 10 times longer. Therefore, the NVL method is chosen in the following sections.

Flash strategy	Case 1	Case 2	Case 3	Case 4	Case 5	Case 6	Case 7
NVL	0.68965	1.0782	1.1203	0.77236	7.2450	35.401	1,955
lnK	-	19.933	24.141	23.72	135.48	-	18,378

Table 3.3: Average time, in ms, per case needed for convergence using both flash methods studied here.

In the following subsections, results from using NVL iterations are shown regarding the pressure field, vapor volume fraction and number of flash iterations for convergence. Finally, results are validated against experimental VLE data. All the calculation data can be found in the Appendix B.

3.2.1 Pressure Field

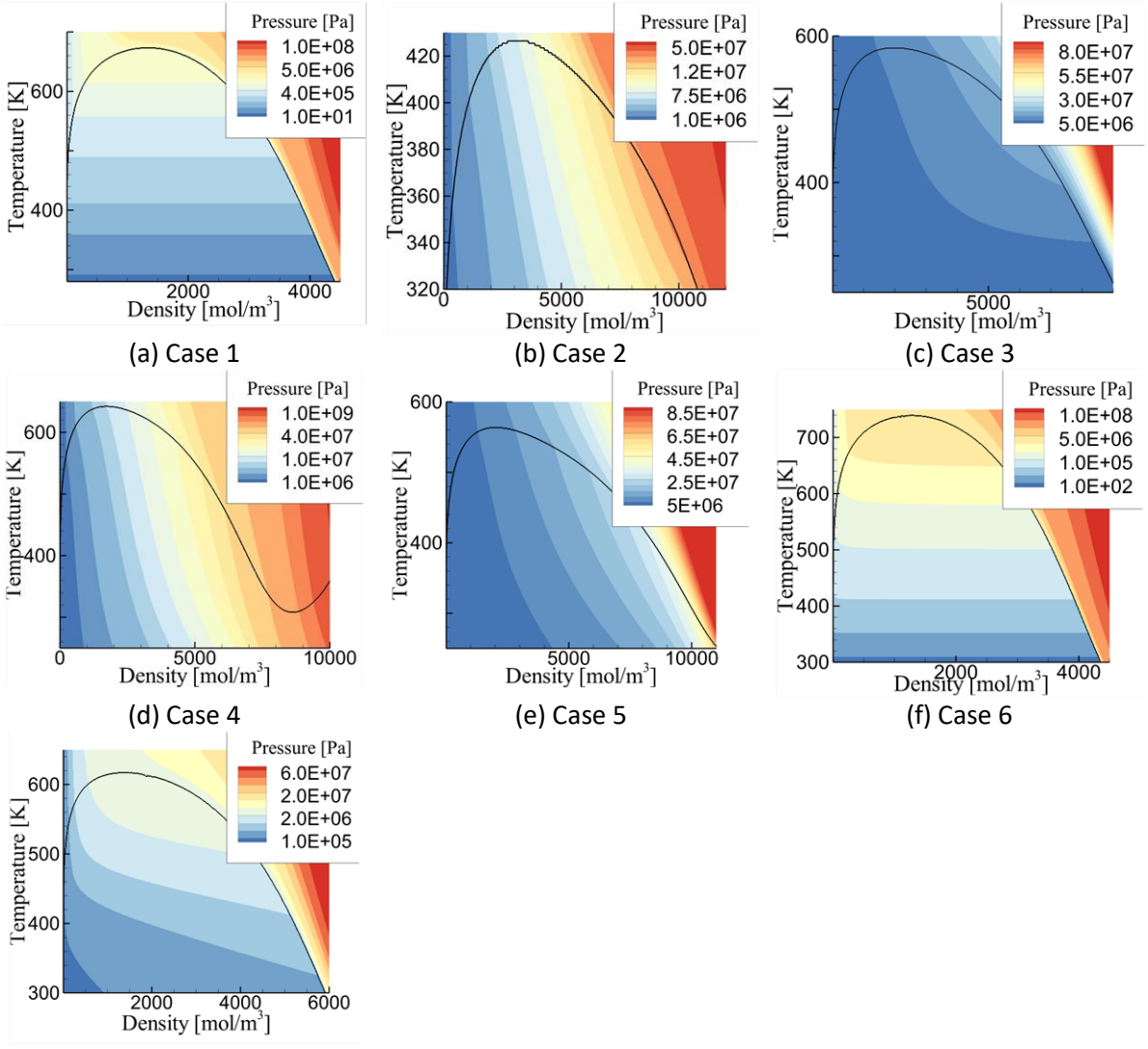

Figure 3.1. Pressure field for all cases studied in the paper, the black curve draws the saturation line. The colour scale is unique for every figure.

Figure 3.1 shows the pressure field for every case, marking with a black curve the saturation line. Depending on the components and composition, the pressure field varies significantly. Cases 1 and 6, those which are meant to model Diesel fuel, show similar horizontal isobaric lines when in the VLE region, where the PT-VLE algorithm is known to fail. Case 1 shows isobaric-isothermal phase transition by definition, as it is a single component. Case 6, the 8-component mixture, shows a similar trend due to the similarity between the components, although the small differences among them can be seen close to the dew curve, where the isobars bend upwards. Cases 2, 4 and 5 show isobars with significant slope which isobaric vapor-liquid transition comes with a massive decrease in temperature, typical of

mixtures exhibiting extremely different phase transition properties. For instance, from Case 2 the critical temperature of pentane is close to 2.5 times than that of methane, while more obviously in Case 4 the critical temperature of dodecane is more than 5 times higher than that of nitrogen. Case 3 shows an intermediate field between Cases 1 and 2, where while at high temperatures the slope is sufficiently pronounced, at low temperatures and high densities the isobars become progressively flat, where the PT-VLE problem is expected to start failing. Regarding the 50-component hydrocarbon mixture, the isobars show significant slope as there are both very light and very heavy hydrocarbons, for instance methane and octadecane.

3.2.2 Vapor volume Fraction Field

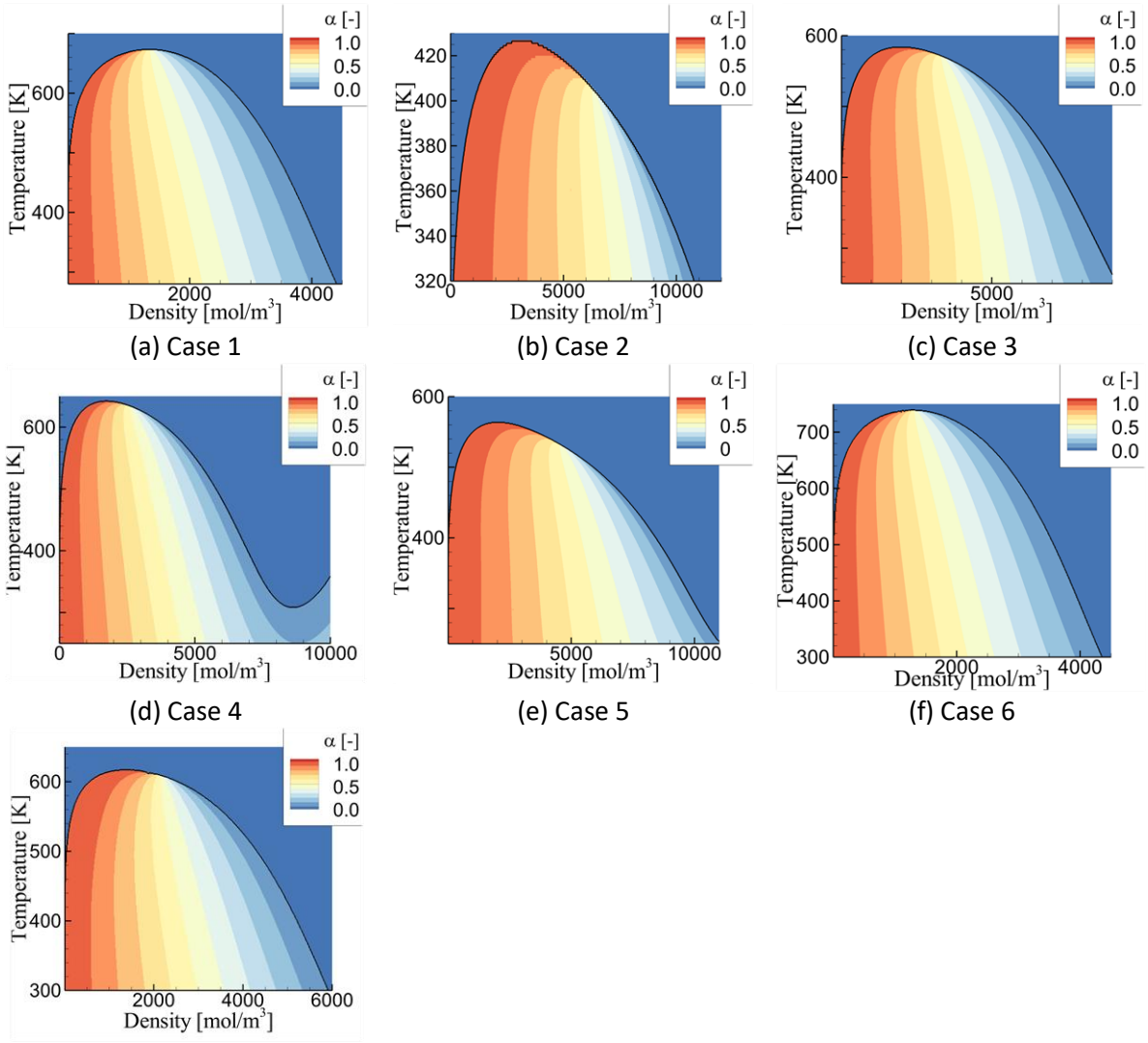

Figure 3.2. Vapor volume fraction field for all cases studied in the paper, the black curve draws the saturation line. The colour scale is the same on every figure.

Figure 3.2 shows the vapor volume fraction field for every case, marking with a black curve the saturation line. Cases 1 and 6 show the typical vapor volume fraction field for every single component, where the isolines converge at the critical point, being in this case the maximum temperature and pressure at which a two-phase state can be found. On the rest of cases, the critical point is not located on the maximum two-phase temperature or pressure, but on a lower value. This phenomenon gives rise to the retrograde vaporisation[159], which accounts for the anomalous isothermal vaporisation of the mixture when the pressure is increased. Case 4, in addition, shows at 320K a liquid-liquid critical

point, where the equilibrium pressure is higher than 100MPa, clearly seen on the change in curvature of the saturation curve.

3.2.3 Flash iterations until convergence

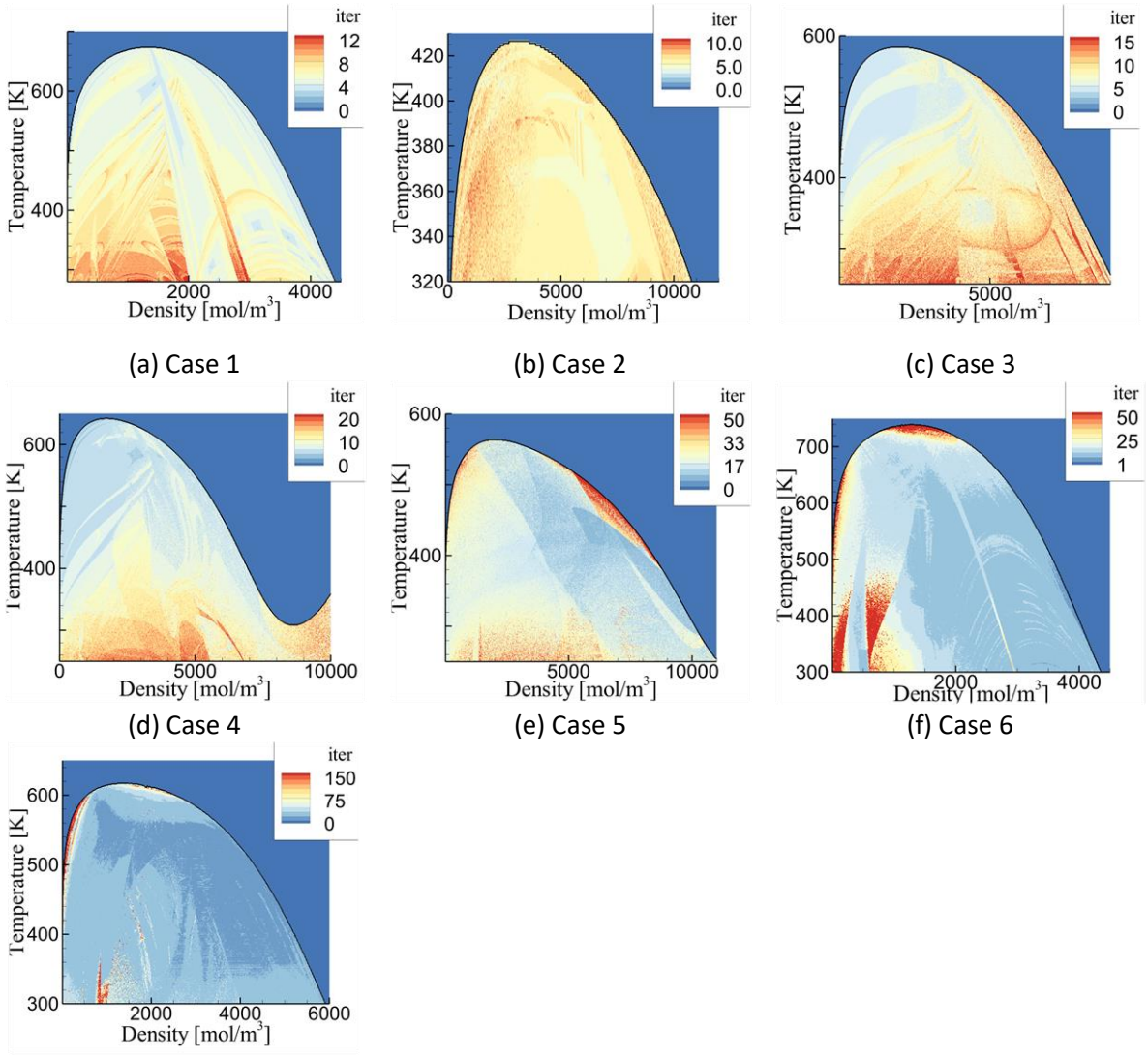

Figure 3.3. Flash iterations field for all cases studied in the paper, the black curve draws the saturation line. The colour scale is unique for every figure.

Figure 3.3 shows the number of flash iterations needed for convergence using the NVL-algorithm for every case, marking with a black curve the saturation line. Case 1 shows a reasonably homogeneous distribution, with maximum number of iterations of 10 at low temperatures and intermediate densities. The distribution of Case 2 iterations is as homogeneous as in Case 1, with a maximum iteration number of 10. For Case 3, the highest numbers are localised at temperatures lower than 350K and close to the bubble-point curve, where the number of iterations reach 15. Regarding

Case 4, the higher number of iterations are found at temperatures lower than 350K and at densities higher than 9,000mol/m^3, where the calculated equilibrium pressure reaches 1,000MPa. For the 4-component mixture in Case 5, more than 50 iterations are needed along to the bubble point curve at high temperatures. High number of iterations are also observed for temperatures lower than 300K and close to the dew-point curve at high temperatures. Overall, at high temperatures the phase change needs a particularly high number of iterations for convergence. The 8-component surrogate in Case 6 the maximum number of iterations, which may reach 100, are found close to the critical point and at high temperatures close to the dew-point curve. For the 50-component hydrocarbon mixture, the number of iterations grow considerably compared with the previous cases, where the threshold of 150 iterations is reached again at the critical point and the dew curve, in addition to localised high number of iterations at 1,000mol/m^3 and temperatures lower than 350K.

3.2.4 Performance comparison against Peng Robinson EoS

The performance of the algorithm can be influenced significantly by the chosen equation of state, as every iteration needs the calculation of many properties and its derivatives for the two phases. The use of PC-SAFT EoS has been already reported to increase the computational time needed for a single equilibrium calculation with respect to Peng Robinson[160]. Previous works, using a PT-VLE calculation, have obtained differences in CPU time of 2-3 times between the Peng Robinson EoS and PC-SAFT EoS[84] for a variety of mixtures. For some mixtures, even, the computational time was found smaller for the original PC-SAFT than for the cubic EoS. However, von Solms[84] estimated that the CPU time needed for the calculation of all the derivatives involved in the PT-VLE was 4-5 times higher than for the SRK EoS, using the simplified PC-SAFT for a mixture of 15 components. The simplified PC-SAFT is known to be significantly more efficient in VLE calculations as some of the terms of the original version become composition-independent. Therefore, the difference between cubic EoS and the PC-SAFT is expected to be higher than 4-5 times, even if the number of function evaluations is similar.

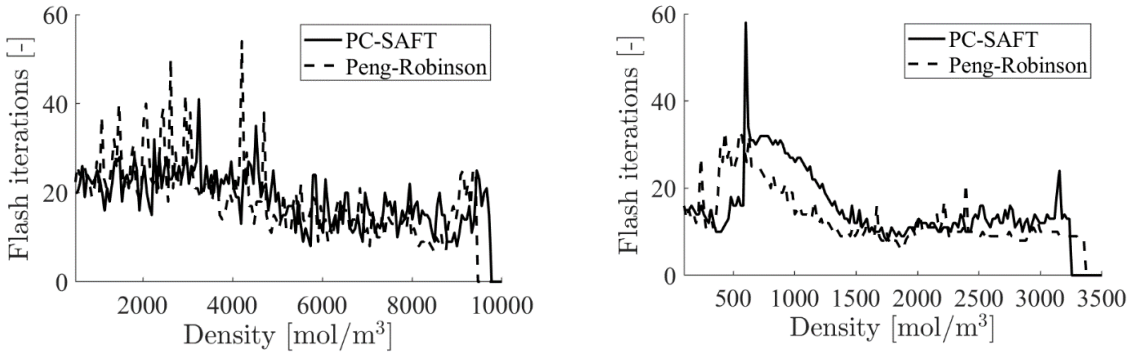

(a) (b)

Figure 3.4. Flash iterations needed for Cases 5 and 6 at 300K using Peng-Robinson and PC-SAFT as Equations of State at 300K.

Figure 3.4 shows two performance comparisons for Cases 5 (4 component mixture) and 6 (8 component mixture) regarding the iterations needed for calculating the equilibrium at 300K for a range of densities, using both Peng Robinson and PC-SAFT EoS. Flash iterations are both initialized

from a previous stability analysis. As shown, for the 4-component mixture the iterations needed are quite similar for both Equations of State, apart from particular conditions at which the cubic equation seems to spike. Overall, the iterations needed at lower densities than 5000mol/m3 are higher than those at higher densities. For the 8-component surrogate, the number of iterations needed at low densities are significantly higher for PC-SAFT, although at densities higher than 1500mol/m3 the convergence is achieved in a similar number of iterations.

EoS	Case 1	Case 2	Case 3	Case 4	Case 5	Case 6	Case 7
PC-SAFT	629.79	1340.6	1143.8	1059.4	1878.1	13996	363270
Peng Robinson	156.25	182.62	191.98	210.94	250.31	937.53	10332
Ratio	4.03	7.34	5.96	5.02	7.5	14.9	35.16

Table 3.4: Computational time in μs, per single VLE calculation, needed for all cases using Peng Robinson and PC-SAFT. The last row shows the ratio between both CPU times.

Table 3.4 shows the computational time, per VLE calculation, needed for all cases using both Peng Robinson and PC-SAFT EoS. Results indicate a significant difference between both EoS, which increases with the number of components. While for a single component the CPU time for PC-SAFT is about 4 times higher than for Peng-Robinson, for two components it grows to about 6 and up to 15 for the 8-component surrogate of case 6. An extreme case is seen for case 7, where the computational time needed to calculate the VLE for a 50-component mixture increases to 35. These differences can be explained due to the high dependence on composition of the PC-SAFT EoS, which increases the number of calculations needed for the derivatives exponentially. The reader may acknowledge the extent of the derivations in the complete formulation of the algorithm found in the Appendix B. This can be also seen in Table 3.5, where the computational time per single calculation of the derivatives is shown. The range in temperature and density per case is the same as in previous sections. As seen, the difference between the CPU time of Peng Robinson and PC-SAFT grows with the number of components in a similar fashion than for the complete VLE calculations. Discrepancies between the single EoS and complete VLE calculations can be explained because of differences in the number of

iterations needed for the convergence, which is not necessarily the same, although similar as already seen in Figure 3.4.

EoS	Case 1	Case 2	Case 3	Case 4	Case 5	Case 6	Case 7
PC-SAFT	8.844	13.37	13.70	14.66	31.20	100.0	25380
Peng Robinson	1.800	2.323	2.341	2.342	3.421	7.046	58.75
Ratio	4.91	5.76	5.84	6.25	9.12	14.19	43.2

Table 3.5: Computational time in μs, per single calculation of all the needed derivatives, for all cases using Peng Robinson and PC-SAFT. The last row shows the ratio between both CPU times.

These results show why when computational power is the main restriction in simulations, past works tend to choose the Peng-Robinson over more accurate EoS such as the PC-SAFT. For instance, in Computational Fluid Dynamics, equilibrium calculations may be needed in more than 1 million cells per timestep, making the EoS choice the main decision criterion regarding the trade-off between accuracy and computational efficiency.

3.2.5 Validation against experiments

Figure 3.6 shows validation cases to assess the accuracy of the model when compared to experimental data. The data was collected and compared for Case 2[161], Case 4[162] and the Y8 synthetic mixture[158]. The Y8 mixture is composed of 6 components with composition: 0.8097 methane, 0.0566 ethane, 0.0306 propane, 0.0457 n-pentane, 0.0330 n-heptane and 0.0244 n-decane. The binary interaction parameters were set to 0 for the Y8 mixture. As it can be seen, there exists good agreement for every case using the corresponding binary interaction parameters. The first two figures show the typical binary phase diagram at different constant temperatures, while the first figure shows the equilibrium constants for every component in the mixture at fixed temperature.

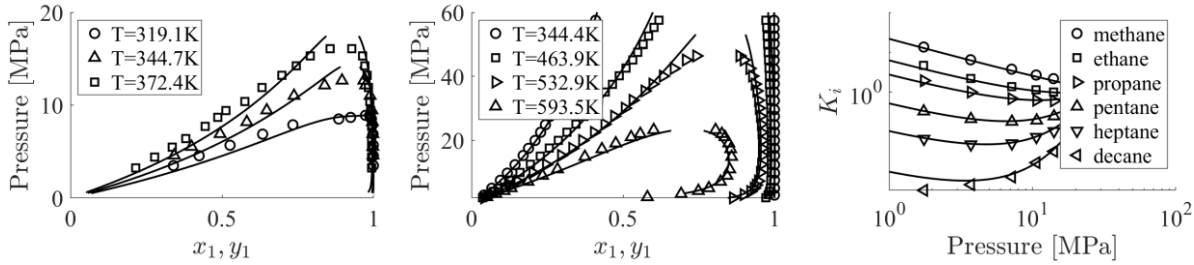

(a) (b) (c)

Figure 3.6: Predicted vapor-liquid equilibrium compared with experimental data for (a) Case 2, (b) Case 4 and (c) the Y8 mixture [37].

Table 3.5 shows the Average Absolute Deviation (AAD [%]) of the calculations with respect to the experimental values for the above cases and it is defined as:

$$AAD[\%] = \frac{100}{N_p}\sum_{i}^{N_p}\left|\frac{(x_i, y_i)^{exp} - (x_i, y_i)^{calc}}{(x_i, y_i)^{exp}}\right| \tag{3.50}$$

Where N_p is the number of compared experimental data points.

	Case 2	Case 4	Y8 Mixture
$AAD[\%]$	2.7901	0.9281	3.6289

Table 3.5: Average Absolute Deviation (AAD [%]) of the three cases shown in Figure 3.6.

As observed in the table, the agreement with experiments is good even for the 6-component mixture, where the average deviation is lower than 4%. However, it is necessary to notice that this agreement is significantly dependent on the binary interaction parameter k_{ij} which is obtained by fitting with experimental VLE data.

3.3 Conclusions

In this section, the PC-SAFT EoS was used for Vapor Equilibrium calculation at specified composition, density and temperature. The presented algorithm was tested on several cases of both single and multicomponent substances. The calculation utilised the Newton iterations to reach the global minimum of the Helmholtz free energy in two stages, namely stability analysis and flash. As a result, the pressure of the fluid and the compositions of both the liquid and vapor phases were calculated. The reliability of two different methods for the flash stage, one based in number of moles and volume (NVL) and another based in the logarithm of the equilibrium constants (lnK), were evaluated in terms of both iterations and computer time needed to reach convergence.

Results showed that although the lnK method needs less iterations until convergence, the total computational time needed is considerably longer. This difference in computational time is caused during the calculation of density in the pressure equality condition, as it needs to be satisfied iteratively. The NVL method does not need to satisfy this condition at every iteration, therefore no inner iterative loops are needed, and faster convergence was obtained. Moreover, the lnK method cannot be used for single components, as its value is unity during all iterations, and it fails continuously for mixtures with similar components, as the 8-component Diesel surrogate studied in Case 6. A performance comparison was obtained against the Peng-Robinson EoS, showing a substantial decrease in computational time when using the cubic compared to the molecular based EoS. Validation against experiments show good agreement of the numerical model.

Future work should be headed towards more complex mixtures, resourcing to the latest applications of PC-SAFT introducing associating[163], multipolar [164] [165] and/or aqueous ionic liquid solutions[166], as the accuracy of this molecular-based EoS is of great value for academic and industrial applications.

4. Preferential cavitation and friction-induced heating of multi-component Diesel fuel surrogates up to 450MPa

This section investigates the influence of properties variation of a multicomponent Diesel fuel surrogate in the range of injection pressures from 60MPa to 450MPa on nozzle flow and cavitation. The compressible form of the Navier-Stokes equations is numerically solved in a density-based solver employing the homogeneous mixture model for accounting the present of liquid and vapour phases, while turbulence is resolved using a Large Eddy Simulation approximation. Simulations are performed on a tapered heavy-duty Diesel engine injector at a nominal fully-open needle valve lift of 350μm. To account for the effect of extreme fuel pressurisation, two approaches have been followed: (i) a barotropic evolution of density as function of pressure, where thermal effects are not considered and (ii) the inclusion of wall friction-induced and pressurisation thermal effects by solving the energy conservation equation. The PC-SAFT equation of state is utilised to derive thermodynamic and thermophysical property tables for an eight-component surrogate based on a grade no.2 Diesel emissions-certification fuel as function of pressure, temperature and fuel vapour volume fraction. Moreover, the preferential vaporisation of the fuel components within the injector's hole is predicted by Vapour-Liquid Equilibrium calculations.

4.1 Numerical Method

4.1.1 CFD model

The in-house density-based CFD codes used in this work solves the compressible Navier-Stokes equations utilising the open-access OpenFOAM[167] platform. The barotropic behaviour of the fluid does not consider the energy conservation equation. The second one solves the Navier-Stokes system and the energy conservation equation. Both solvers share a system which consists of the continuity equation:

$$\frac{\partial \rho}{\partial t} + \nabla \cdot (\rho \boldsymbol{u}) = 0 \tag{4.1}$$

Where ρ is the mixture density and $\boldsymbol{u}$ the velocity vector field, and the momentum equation:

$$\frac{\partial (\rho \boldsymbol{u})}{\partial t} + \nabla \cdot (\rho \boldsymbol{u} \otimes \boldsymbol{u}) = -\nabla p + \nabla \cdot \boldsymbol{\tau} \tag{4.2}$$

where p is the pressure and $\boldsymbol{\tau}$ is the stress tensor defined as $\boldsymbol{\tau} = \mu_{eff}[\nabla \boldsymbol{u} + (\nabla \boldsymbol{u})^T] + \mu_B \mathbf{I} \nabla \cdot \boldsymbol{u}$, with $\mathbf{I}$ as the unit tensor, μ_B as the bulk viscosity and μ_{eff} defined as the sum of laminar, μ given by the thermodynamic table, and turbulent, μ_T, dynamic viscosities. The bulk viscosity μ_B is neglected in this work because its effect can be negligible on the general dynamics of the flow[168]. Moreover, general and accurate models regarding this viscosity are, to the author's best knowledge, not available. Regarding the turbulence model, a Large Eddy Simulation (LES) model is used, as it can reproduce accurately enough the turbulent structures found in Diesel nozzles[93, 169]. In the present study, the Reynolds number is ~[35000-90000] and thus, it is within the range of applicability of the selected model. In particular, the turbulent viscosity is modelled using the Wall Adaptive Large Eddy (WALE) model[170], by the equation:

$$\mu_t = \rho {L_s}^2 \frac{\left({S_{ij}}^d {S_{ij}}^d\right)^{3/2}}{\left(S_{ij} S_{ij}\right)^{5/4} + \left({S_{ij}}^d {S_{ij}}^d\right)^{5/4}} \tag{4.3}$$

where S_{ij} is the rate of strain tensor and ${S_{ij}}^d$ is the traceless symmetric part of the square of the strain of the velocity gradient tensor, i.e.:

$${S_{ij}}^d = \frac{1}{2}\left({g_{ij}}^2 + {g_{ji}}^2\right) - \frac{1}{3}\delta_{ij} {g_{kk}}^2 \tag{4.4}$$

With, $g_{ij} = \frac{\partial u_i}{\partial x_j}$ and δ_{ij} the Kronecker delta. The length scale, L_s, is based on the filter size and the cell to wall distance, d_{wall}, as follows:

$$\mathrm{L} = min\{\kappa\, d_{wall}, C_w\, V^{1/3}\} \tag{4.5}$$

where the used model constants are: κ the von Karman constant, 0.41, and C_w = 0.325.

In order to take into account thermal effects, in this work the energy conservation equation is also solved:

$$\frac{\partial(\rho E)}{\partial t} + \nabla \cdot (\rho \boldsymbol{u} E) = -\nabla \cdot (p\boldsymbol{u}) + \nabla \cdot (\tau \cdot \boldsymbol{u}) - \nabla \cdot (k_T \nabla T) \tag{4.6}$$

where E is the specific total energy of the system, defined as internal energy plus the kinetic energy, i.e. $E = h - \frac{p}{\rho} + \frac{|\boldsymbol{u}|^2}{2}$ where h is the enthalpy, and k_T the thermal conductivity of the fluid given by the property tables.

Hybrid flux model

Two-phase flows are characterised, among others, by large variations in speed of sound. While the speed of sound in the liquid phase is of the order of $O(10^3)$m/s and that of gas is $O(10^2)$m/s, in the liquid-vapour state it sinks down to $O(1)$m/s. Therefore, for a typical velocity at the orifice of $O(10^2)$m/s, it can be expected a Mach number range from $O(10^{-1})$ to $O(10^2)$. For density-based solvers, low Mach numbers are related to convergence problems and dispersion, so a hybrid flux is used for accounting for both low and high Mach numbers. That, in terms of the interface pressure within the approximated Riemann solver scheme is:

$$p = [1 - \beta(M)]p^{inc} + \beta(M)p^{comp} \tag{4.7}$$

where

$$p^{inc} = \frac{C^L p^R + C^R p^L}{C^L + C^R} \tag{4.8}$$

$$p^{comp} = \frac{C^L p^R + C^R p^L + C^R C^L (u^L - u^R)}{C^L + C^R} \tag{4.9}$$

where $C = \rho c$ is the acoustic impedance, u is the interface velocity, L and R refer to the left and right side of the interface and:

$$\beta(M) = 1 - e^{-aM} \tag{4.10}$$

where a is a blending coefficient, set to 1.5. Thus $\beta(M) \to 0$ when $M \to 0$, and therefore $p = p^{inc}$. On the other hand, $\beta(M) \to 1$ when $M \to \infty$, and therefore $p = p^{comp}$.

4.1.2 Injector geometry and operating conditions

The examined injector geometry was based on a common rail 5-hole tip injector with tapered hole. The most important dimensions for this injector are shown in Table 4.1. As focus is given here

on the effect of fuel properties, complications arising from the needle valve motion have been ignored. Although the simulation is transient, the needle valve was assumed to be still at its full lift of 350μm during the main injection stage. Transient effects although important for cavitation erosion[171], nozzle wall wetting and formation of non-well atomised liquid fragments that can affect emissions are out of scope of the present work.

The simulated geometry considers only one fifth of the full injector geometry, as shown in Figure 4.1, imposing periodic boundary conditions on the symmetry planes. A hemispherical volume is attached to the nozzle exit; this volume is added in order to be able to capture the complete cavitation cloud inside the nozzle and avoid interference with the outlet boundary. Characteristic volumes of the injector geometry are also pointed out by colour in Figure 4.1. As the wall temperature of the nozzle is practically unknown, the walls are assumed to be adiabatic. Constant pressure boundary conditions of 60, 120, 180, 250, 350 and 450MPa at the inlet and 5MPa at the outlet have been imposed. The temperature at the boundaries is set as those corresponding to the isentropic expansion of the fuel from a reference point set at 5MPa and 324K, shown in Table 4.2. Also, in Table 4.2 it can be found the mean exit velocity, speed of sound on the liquid, Mach number and discharge coefficient for each injection pressure. This outlet temperature is chosen based on the theoretical outlet temperature for operation at a reference injection pressure of 180MPa and a discharge coefficient of unity, i.e. the ideal case without pressure losses, as calculated in[172] using the same geometry. The two-phase flow is assumed to be a homogeneous mixture of vapour and liquid in mechanical equilibrium, i.e. both phases share the same pressure and velocity fields. This implies that as there is only one fluid in the entire domain, the discharge is on liquid; this configuration resembles that of injector test benches, where fuel is squirted for thousands of hours into a liquid-filled collector.

Geometrical characteristics		
Needle radius at inlet (mm)		1.711
Orifice length L (mm)		1.262
Orifice diameter (mm)	Entrance D_{in}	0.37
	Exit D_{out}	0.359
Sac volume (mm^3)		1.19
k-factor[173] = (D_{in} - D_{out})/10, D in µm		1.1

Table 4.1. Dimension of the injector used for the simulations on this work.

$P_{inj}[MPa]$	T_{inlet} [K]	U_{exit} [m/s]	$c_{liquid}[m/s]$	$M_{liquid}[-]$	C_d
60	332	332.39	1128	0.2946	0.842
120	340	461.02	1066	0.4324	0.819
180	345	564.69	1057	0.5342	0.813
250	350	664.77	1045	0.6361	0.812
350	359	781.67	1012	0.7724	0.807
450	365	881.74	1001	0.8808	0.804

Table 4.2. For each injection pressure, inlet temperatures, mean exit velocity, speed of sound on the liquid, Mach number and discharge coefficient. The outlet conditions are fixed to 5MPa and 324K.

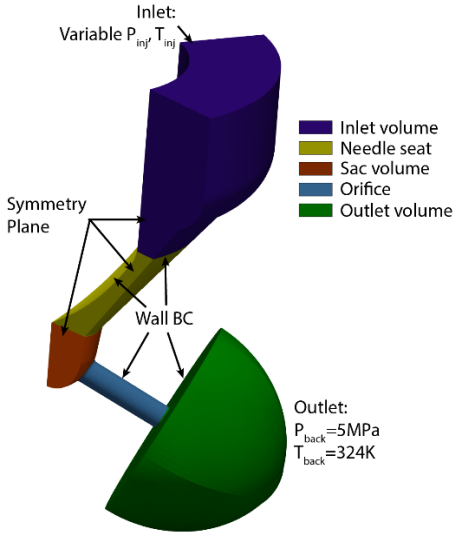

Figure 4.1. Simulated geometry, one fifth of the complete injector nozzle. Characteristic volumes are colourised, and the boundary conditions are indicated.

Regarding the computational mesh, two topologies have been used. Before the orifice entrance, in the sac volume, there is an unstructured tetrahedral mesh. For the rest of the domain, a hexahedral block-structured mesh is used. Given the flow conditions inside the injector nozzles, the Reynolds

number at the orifice, where cavitation develops, varies significantly between the cases. For 60MPa, it is ~35000, for 180MPa is ~60000 and ~90000 for 450MPa. This corresponds to Taylor length scales, λ_g:

$$\lambda_g = \sqrt{10} Re^{-0.5} D \in (4\mu m, 6.5\mu m) \quad (4.11)$$

Where D is an indicative length of the geometry, in this case the nozzle hole exit diameter. The resolution in the core of the orifice is ~5μm, with refinement near the walls up to a minimum cell size of ~2 μm. As the vaporous core of cavitating vortices has been found to be in the order of 20μm[174], the cell size is small enough to capture the smallest scales present in the flow that can potentially lead to vortex cavitation. The timestep was adapted to a fixed acoustic Courant number of 0.5, thus the timestep varied from 8ps for the 450MPa case to 100ps for the 60MPa case. Table 4.3 shows integral quantities of engineering interest, such as the overall mass and energy balance for each injection pressure, with thermal effects being considered. The last column in Table 4.3 shows the difference found in the mass flow rate at the exit for a refined mesh, decreasing the smallest cell size to 1.06μm and, therefore, increasing the number of cells to 11M. No significant differences were found and therefore the 1.5M cells mesh was used in the following sections.

	Mass flow rate $[g/s]$		**Energy flow rate** $[kJ/s]$		**%change in** $\dot{m}_{out}$
P_{inj}	***Inlet***	***Outlet***	***Inlet***	***Outlet***	**after refinement**
60	24.37	24.53	31.97	32.19	-
120	33.89	34.16	42.08	42.43	-
180	41.32	41.72	48.19	48.67	0.0528
250	49.06	49.38	53.91	54.28	0.0785
350	58.09	58.38	57.74	58.11	0.1169
450	66.31	66.59	59.17	59.44	0.1542

Table 4.3. Time-averaged mass and energy flow rates at the inlet and outlet for all cases, with thermal effects being considered. The last column shows the percentage change in mass flow rate at the outlet after a refinement from 1.5M to 11M cells for cases 180MPa to 450MPa, decreasing thus minimum cell size from 2.12μm to 1.06μm.

4.1.3 Thermodynamic and thermophysical properties

As already mentioned, the thermodynamic and thermophysical properties of the Diesel surrogate are modelled using the PC-SAFT EoS[175] for a density range of 0.001-1100kg/m3 and an internal energy range of -1.40779-4.7529MJ/kg in a tabulated format. The pure-component parameters can be found

in Appendix C. The range in internal energy corresponds to temperatures in range of 280-2000K. These limits allow the correct characterisation of the vaporised and compressed fuel alike while also capturing the increased temperatures due to friction-induced heating. The structure of the table consists on 1000x1000 elements separated by constant intervals of the decimal logarithm (log10) of the density and internal energy. The properties are calculated every 0.006047 log10(kg/m^3) and 6.16696kJ/kg. For the barotropic approach, the properties were calculated maintaining the entropy of the fluid constant to that obtained at 324K and the imposed outlet pressure of 5MPa. Therefore, in the isentropic case the pressure depends exclusively on density as in any other barotropic-type EoS. Figure 4.2 shows the properties that govern the behaviour of the Diesel surrogate with respect to pressure following different isentropic curves, depending on the assumed reference temperature. While the black line refers to the one used in the barotropic approach, the other two refer to reference temperatures of: (i) 384K that is the maximum temperature reached in the liquid-vapor equilibrium phase for P_{inj}=180MPa considering thermal effects, and (ii) 484K that the maximum temperature reached in the liquid-vapor equilibrium phase for P_{inj}=450MPa considering thermal effects. As shown, at higher temperatures the values for density, viscosity and thermal conductivity decrease, while increasing the heat conductivity.

The calculation of the vapour volume fraction α_v is determined by minimizing the Helmholtz Free Energy, using the algorithm presented in Section 3. For the conditions studied in these isentropic simulations, the vapour pressure for the isentropic Diesel fuel is predicted to be 230Pa. For the case where the complete range is resolved, the saturation pressure is not fixed and will depend as well on the internal energy.

As noted in the introduction section, the validity of thermodynamic equilibrium at such a range of pressure conditions is not easy to obtain. Models typically assume a spherical bubble shape, the interaction between bubbles (break-up, coalescence) is not easy to describe and the coupling with the continuous phase (liquid) is difficult in areas of large void fractions[114]. In any case, the relaxation time of the tensile stresses, i.e. those acting in the metastable state, was numerically estimated to be of

the order of 10ns for a vertical tube filled with liquid, impacted vertically, suddenly and producing an expansion wave of 30MPa[176]. However, the concentration used in this study was infinitesimally small, which is not applicable to real systems and thus its result is a significant overprediction. Nevertheless, it is possible to use this time-scale to observe that, as the residence time of the fluid can be estimated to be of 1μs for an injection pressure of 450MPa, the time to reach equilibrium would be, at least, 100 times faster.

The speed of sound c is calculated for a single phase directly from its definition:

$$c = \sqrt{\left(\frac{\partial p}{\partial \rho}\right)_s} \tag{4.12}$$

Where the subscript s indicates that the derivative is computed at constant entropy. When the fluid is in the two-phase region, the speed of sound follows Wallis' rule[177]:

$$\frac{1}{\rho c^2} = \frac{\alpha_v}{\rho_v c_v^2} + \frac{1-\alpha_v}{\rho_l c_l^2} \tag{4.13}$$

where the subscripts v and l stand for vapour and liquid phase.

In case of the dynamic viscosity, μ, it is calculated by using an entropy scaling method[141], as in Section 2.2. For the two-phase region, the homogeneous viscosity is calculated with the expression[178]:

$$\mu = (1-\alpha_v)\left(1+\frac{5}{2}\right)\mu_l + \alpha_v \mu_v \tag{4.14}$$

Regarding the thermal conductivity, it is also calculated using the entropy scaling method[179] and a simple weighted mixing rule with the vapour volume fraction is used:

$$k_T = (1-\alpha_v)\, k_{T,l} + \alpha_v\, k_{T,v} \tag{4.15}$$

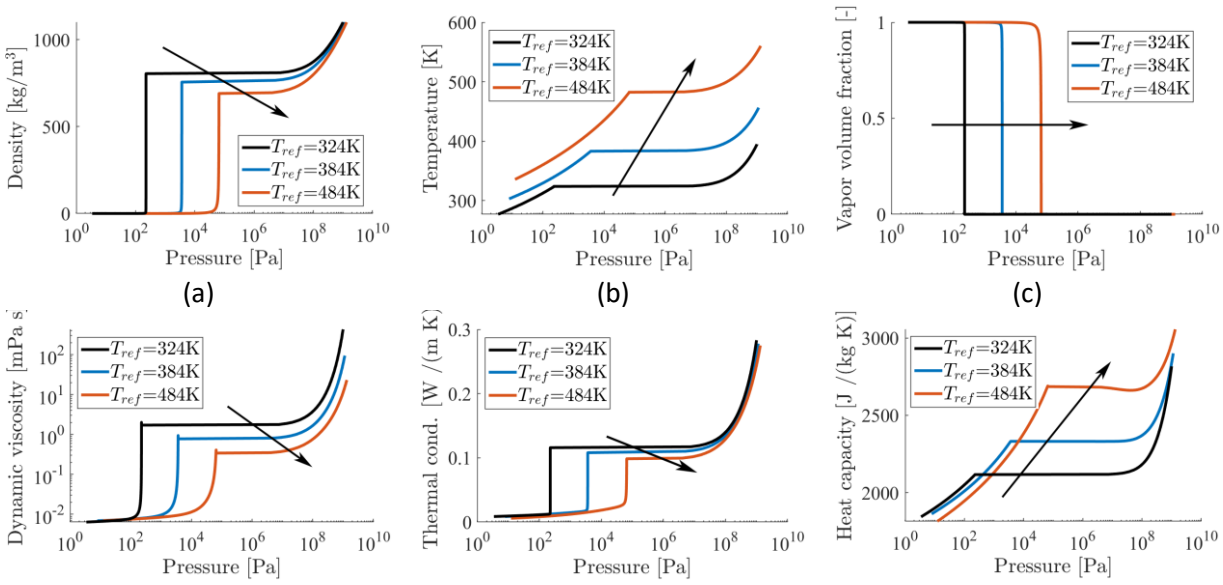

Figure 4.2. Thermodynamic and thermophysical data following an isentropic expansion of the Diesel surrogate. Three cases are shown depending on the reference temperature at 5MPa: (i) 324K for the barotropic method used in this work, (ii) 384K as the maximum temperature reached in the liquid-vapor equilibrium phase for P_{inj}=180MPa considering thermal effects, and (iii) 484K as the maximum temperature reached in the liquid-vapor equilibrium phase for P_{inj}=450MPa considering thermal effects. Arrows added to guide the reader on the direction of increasing reference temperature.

4.2 Results

In this section, the results obtained for the range of injection pressures from 60MPa and up to 450MPa are presented. If not stated otherwise, all results consider thermal effects. Firstly, the internal flow through the injector is inspected. Secondly, the changes in temperature and vapour pressure are investigated and compared with the case where thermal effects are neglected. Thirdly, the formation of cavitation inside the nozzle orifice is analysed. Lastly, due to the multicomponent nature of the fuel, the preferential cavitation of its components is examined.

4.2.1 Flow field

Figures 4.3 through 4.5 show time-averaged predictions for three flow variables through the Diesel injector, respectively, at three injection pressures. The variables presented are: (i) the magnitude of the vorticity on a logarithmic scale, (ii) density and (ii) viscosity. The results are presented in two sets of slices: one longitudinal to the injector geometry and four transversals to the nozzle hole. Thin solid black lines are added for clarity; all plots on each Figure share the same colour scale. Vorticity can indicate locations where thermal effects become significant due to shearing. Lower values, of the order of 10^5/s or smaller, are seen in the core of the flow as it travels through the sac volume and into the orifice. These values indicate a relatively uniform velocity profile. Close to the wall's vorticity is generated reaching values up to 10^8/s, due to the large shear induced from the velocity no-slip condition on the walls. High values of ~10^7/s are also found on a relatively wide region located on the top half of the orifice volume, where separation of the flow occurs and cavitation is forming. Density and viscosity show similar behaviour throughout the injector. Inside the nozzle's sac volume, densities take values from 845 kg/m^3 for injection pressure of 60MPa, 900.342 kg/m^3 for 180MPa and up to 982.345 kg/m^3 for 450MPa. This density decreases as the fuel expands through the orifice down to ~720kg/m^3 on average at the exit of the orifice (50MPa). As the flow separates at the entrance of the injector orifice and the fuel cavitates, densities decrease locally 3 orders of magnitude, to ~10^{-3} kg/m^3, inducing strong density gradients. It can be also clearly seen that as injection pressure increases, the

extend of low-density values for the vapour-liquid mixture is significantly reduced, due to the gradual condensation of vapour caused by the increased pressures present inside the injection hole. The isosurface of 50% vapour volume fraction is included, showing for the 180 and 450MPa cases two coherent structures separated at the symmetry midplane; thorough discussion of the cavitation formation and development will be given in the following subsections. Regarding viscosity, the increase with injection pressure in the nozzle's sac volume is significantly higher than that for density. At 60MPa, the viscosity of the fuel is 2.66mPa·s, doubling to 5.2mPa·s at 180MPa and then quadrupling up to 19.64mPa·s at 450MPa. Average values at the nozzle exit are ~1.3mPa·s. Minimum values of $7 \cdot 10^{-3}$mPa·s are found again at the entrance of the orifice where the flow separates.

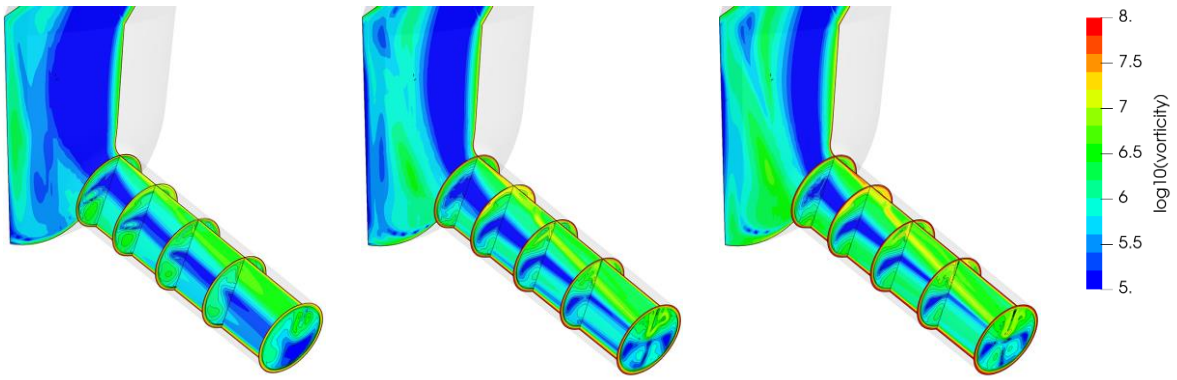

(a) 60MPa (b) 180MPa (c) 450MPa

Figure 4.3. Predicted time-averaged vorticity, in logarithmic scale, on different slices at the sac volume and orifice for three injection pressures. Thermal effects are considered.

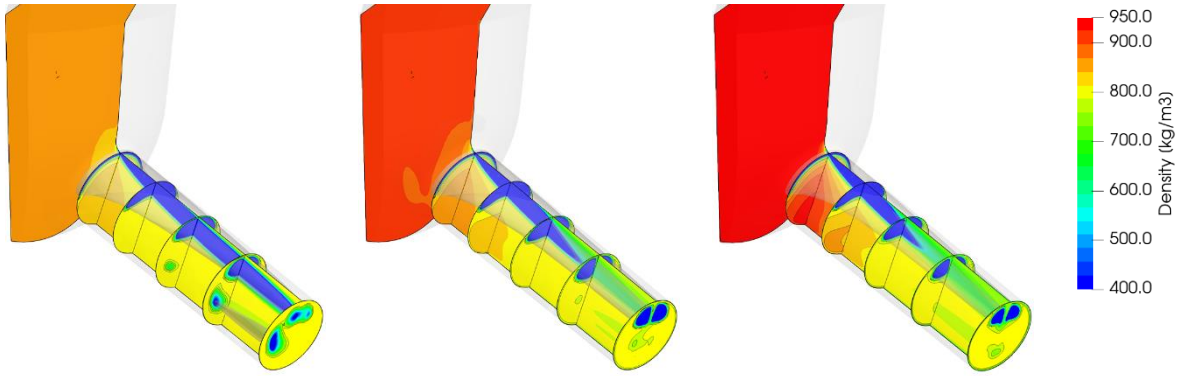

(a) 60MPa (b) 180MPa (c) 450MPa

Figure 4.4. Predicted time-averaged density on different slices at the sac volume and orifice for three injection pressures. Thermal effects are considered. The isosurface for vapour volume fraction of 50% is included, which shows two coherent structures separated at the midplane for (b) and (c).

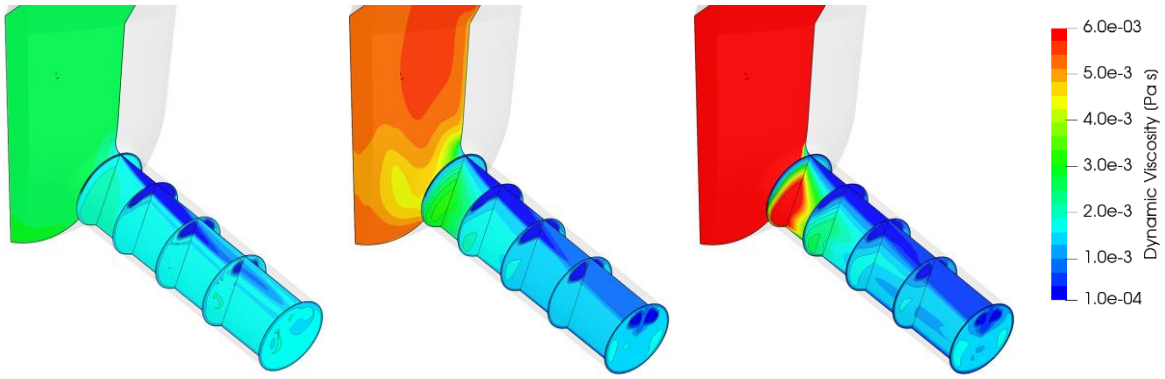

(a) 60MPa (b) 180MPa (c) 450MPa

Figure 4.5. Predicted time-averaged dynamic viscosity on different slices at the sac volume and orifice for three injection pressures. Thermal effects are considered.

Figure 4.6 shows the mass flow rate as function of the pressure drop for all cases, comparing the barotropic approach with that considering thermal effects. As expected, the mass flow rate increases linearly with the square root of the difference between the injection and back pressure. This shows that in neither of the two approaches the flow gets chocked with the increase of the injection pressure. Moreover, the values for the thermal and the barotropic cases are found to be very close. Due to the temperature increase, the density of the fluid drops for the thermal case, but so does the viscosity, enhancing the velocity of the flow. For instance, at 180MPa the density of the thermal case is 2.9% smaller than that for the barotropic case, while the velocities are 2.1% greater, while at 450MPa these

differences are 2.1% and 1.63%, respectively. As a result, these two effects offset each other, and the mass flow rate does not change significantly.

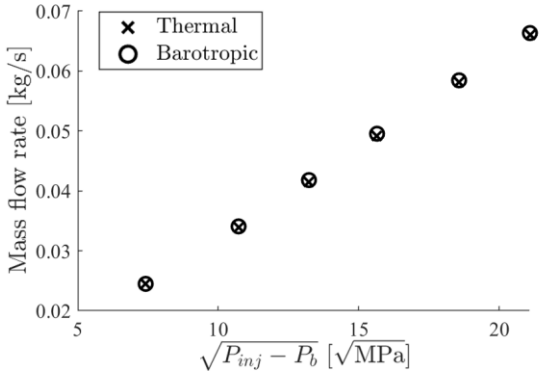

Figure 4.6. Mass flow rate at the orifice exit for both barotropic and thermal case.

4.2.2 Changes in temperature and vapor pressure due to wall friction-induced and pressurisation thermal effects

Figure 4.7 shows the relative temperature change with respect to the injection temperature, defined as:

$$\frac{T - T_{inj}}{T_{inj}} * 100 \tag{4.16}$$

Results are shown for the 60MPa, 180MPa and 450MPa cases, for which the injection temperature is indicated in Table 4.2. A solid line in the longitudinal slice shows where $T = T_{inj}$, thus all points inside this isoline show cooling and those outside show heating. Several observations can be made. First, as the injection pressure increases, temperature gradients increase accordingly, i.e. both lower and higher relative temperatures are found. The temperature of the fuel is heated up due to friction with the walls; this heating is mainly localised on the wall and quickly dissipated towards the centre of the orifice. Where the fuel cavitates, however, the heating cannot be dissipated due to the vapour's significantly lower thermal conductivity and heat capacity, in addition to the significantly lower velocities observed in this region. Thus, the vapour heats up very quickly. As shown, inside the orifice

the higher relative temperatures are also localised in the top region and its peak is found close to the entrance to the injection hole. At this location, the fuel completely cavitates due to flow separation. With respect to the injection temperature, values in this region are found at 60MPa to be ~5% overall higher with a local peak of 50% higher; at 180MPa the top region is observed to heat up ~10% with a local maximum of 70%; lastly, for 450MPa the heating of the fuel is the highest, with 25% and 80% as the maximum. On the other hand, cooling is also enhanced with injection pressure, as seen in the core of the flow. As the injection pressure increases, so does the expansion of the fuel in the orifice, and thus its local cooling away from the shear zones. For 60MPa, the cooling observed is of 5%, 7.5% for 180MPa and up to 10% for 450MPa.

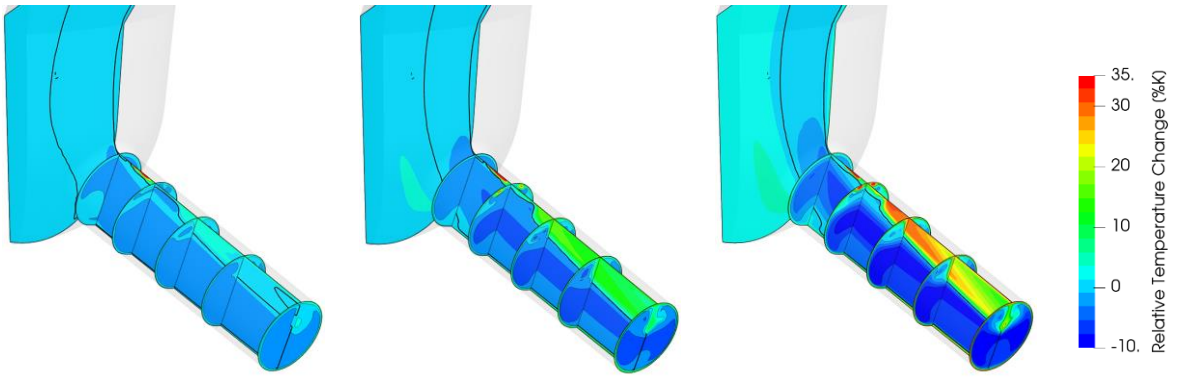

(a) 60MPa (b) 180MPa (c) 450MPa

Figure 4.7. Predicted time-averaged temperature change with respect to the injection temperature, defined as $(T - T_{inj})/T_{inj} * 100$, when thermal effects are considered. The injection temperature for each case is shown in Table 4.2. A solid thick black line is plotted in the longitudinal slice where $T = T_{inj}$, thus all points inside this isoline show cooling and those outside show heating. Results are shown on different slices at the sac volume and orifice for three injection pressures.

Figure 4.8 shows the temperature range found when thermal effects are considered for the liquid, vapour and vapour-liquid equilibrium (VLE) phases; the boiling temperature for the barotropic approach and injection temperatures are added as a reference. The range on the vapour phase is significantly higher than that for the liquid phase. Maximum absolute temperatures found in the injector take values of 510K at 60MPa, 570K at 180MPa and up to 640K at 450MPa. On the liquid phase, heating effects are more contained: at 60MPa the liquid fuel gets heated up to 360K, while for

180MPa it is 410K and for 450MPa is 504K, obtaining a temperature increase of around 28K per 100MPa with respect to the injection temperature. Regarding cooling, it is mainly observed in the liquid phase due to the expansion of the fuel. While for 60MPa the minimum temperatures are found to be 325K, for 180MPa are 337K and 357K for 450MPa, thus making a rough correlation of a 7K of temperature decrease per 100MPa. Where the liquid and vapor coexist, ranges are lower than for the liquid phase. The temperature ranges found are 325-350K for 60 MPa, 335-400K for 180MPa and 355-485K for 450MPa, thus obtaining a maximum temperature range of up to 130K.

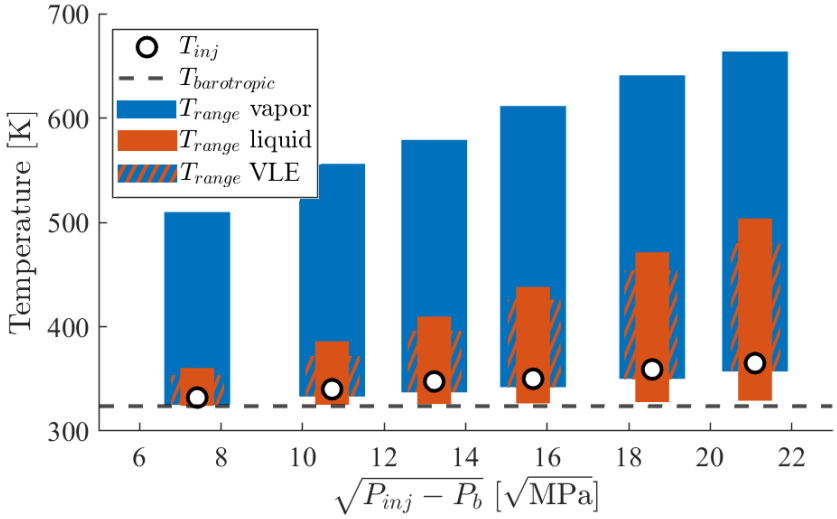

Figure 4.8. Variation in temperature for the liquid, vapor and vapor-liquid equilibrium (VLE) phases, when thermal effects are considered, versus the square root of pressure difference. As a reference, both the injection temperature and the reference temperature used in the barotropic approach are included.

Figure 4.9 shows on the density-temperature thermodynamic diagram the distribution of predicted values in the whole computational domain; the saturation curve of the Diesel surrogate and the isentropic evolution used in the barotropic approach are also indicated. The colour of the plotted points helps identifying their location within the computational domain, i.e. in the injector inlet upstream the needle seat passage, along the needle seat passage, sac volume and inside the injector hole. For all injection pressure cases investigated, it can clearly be seen that the process is not isothermal; as shown before, the range in temperatures increases with increasing injection pressure.

The flow upstream of the nozzle hole (on the right of the saturation curve) shows a smaller range in temperatures than that through the orifice, mostly following the isentropic curve with the corresponding cooling effect due to the expansion of the liquid. There are points that diverge from this isentropic curve both in the needle seat and more clearly in the sac volume, due to thermal effects. This can be clearly seen in the plot for 450MPa: the flow in the sac volume splits into two legs, one corresponding to the core of the flow cooling down due to the liquid expansion and following the isentropic curve, while the other one its heated up because of wall friction.

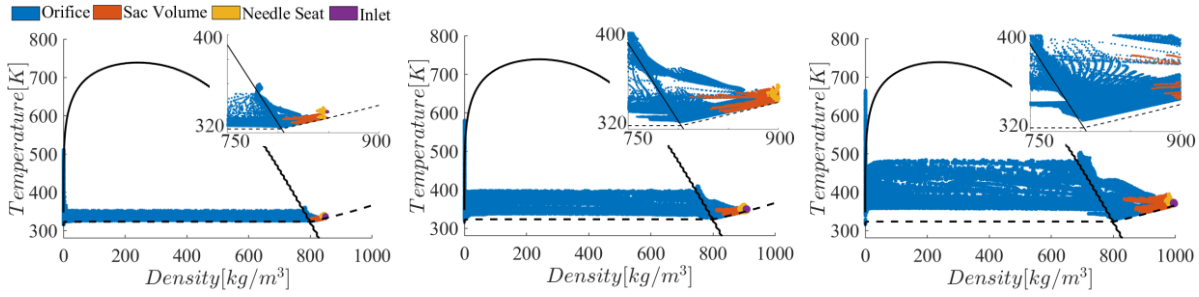

(a) 60MPa (b) 180MPa (c) 450MPa

Figure 4.9. Predicted time-averaged density-temperature values over the whole computational domain for three different injection pressures. Thermal effects are considered. The saturation curve for the multicomponent Diesel surrogate (solid line) and the isentropic approach (dashed line) are indicated. Colour of the symbols distinguishes the zone in the injector they correspond to. As an inset, the distribution of point close to the saturation curve is added.

Another interesting result from the comparison between the barotropic approach and the consideration of thermal effects is shown in Figure 4.10. This figure shows, for a single-time instance, both the isentropic curve, and the results corresponding to thermal effects being considered. The symbols are coloured according to the value of vapor volume fraction. In all cases, the liquid phase follows the isentropic curve reasonably well at high pressures (corresponding to zones before the orifice) while diverging from it as the pressure falls during the discharge of fuel through the nozzle hole. This divergence is significantly enhanced as the injection pressure increases and therefore thermal effects become more pronounced. The distribution of points become progressively wider and shifted to higher pressures, potentially driving towards greater pressure gradients where vapour is

found. As the vapour phase distribution is shifted towards greater pressures, so does the vapour pressure, shown in Figure 4.11 for all cases investigated; it increases with injection pressure to a substantial degree, diverging significantly from the barotropic assumption due to thermal effects. The minimum vapour pressure increases from 290Pa for 60MPa, to 523.5Pa at 180MPa and up to 1259Pa at 450MPa.

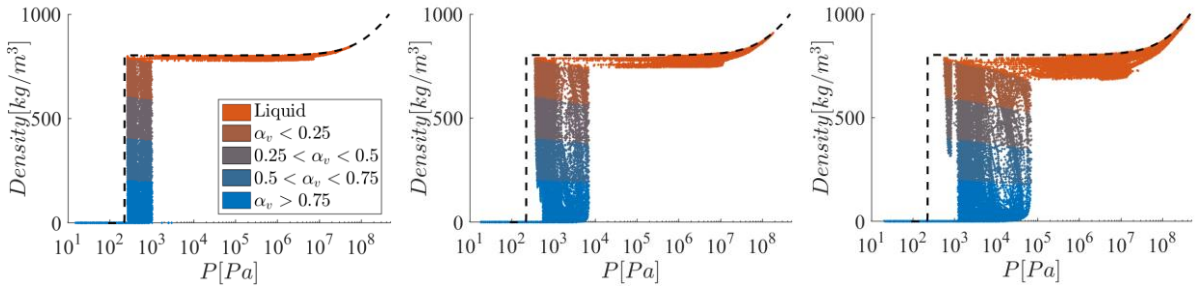

(a) 60MPa (b) 180MPa (c) 450MPa

Figure 4.10. Predicted single-time instance of logarithm of pressure versus density values over the whole computational domain for three injection pressures, when thermal effects are considered; the curve for the barotropic evolution (dashed line) is indicated. The colour of the symbols shows their value of the vapor volume fraction within different ranges.

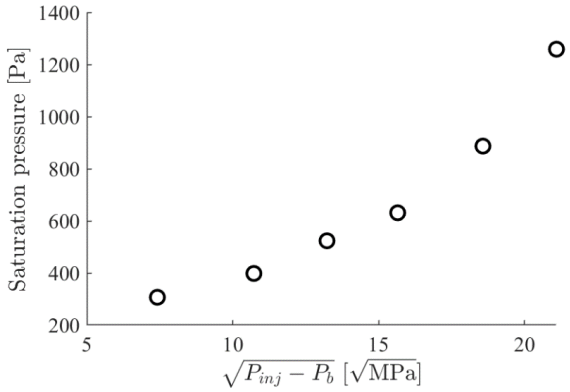

Figure 4.11. Saturation pressure versus the square root of the pressure difference, found for every injection pressure when thermal effects are considered.

4.2.3 Effect of injection pressure on cavitation

Figure 4.12 shows the time-averaged pressure distribution, in logarithmic scale, for three injection pressures on a longitudinal slice of the injector. The isosurface for 50% in vapour volume fraction and the isoline for 5MPa, i.e. the back pressure, are illustrated. As shown, the main difference between

the cases is found at the sac volume, where pressures take values of 55MPa for P_{inj}=60MPa, 162MPa for P_{inj}=180MPa and 405MPa for P_{inj}=450MPa. Indeed, these values are very close to those at the injector inlet. As the needle valve is at full lift, the fuel flows rather undisturbed by the smooth geometrical transition between the inlet and the sac through the needle seat passage. Thus, the expansion of the fuel down to the sac volume is not significant and, therefore, most of this expansion occurs at the orifice. As the injection pressure increases, so does the pressure in the orifice, seen on the increased extent of the 5MPa isoline within the orifice. Regarding cavitation, the isosurface of the vaporised fuel appears to reach just slightly the orifice exit for 60MPa and vortex cavitation is produced as a detached cloud. For 180MPa and 450MPa, cavitation completely reaches the orifice exit and no vortex cavitation is observed. Moreover, the cavitation cloud for 450MPa appears to be thinner than that for 180MPa.

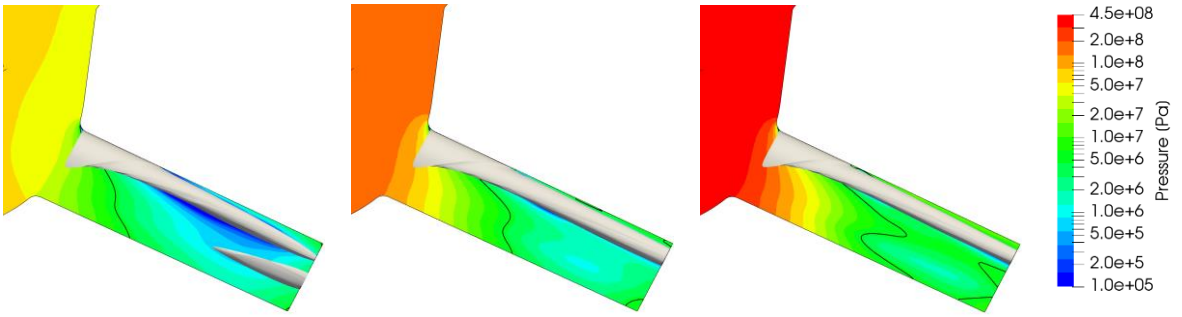

(a) 60MPa (b) 180MPa (c) 450MPa

Figure 4.12. Predicted time-averaged pressure on a longitudinal slice of the injector. A solid black isoline at 5MPa, the back pressure, and the isosurface for 50% vapour volume fraction have been included. The colour map is in logarithmic scale and thermal effects are considered.

These observations of the cavitating cloud are quantified in Figure 4.13(a), which shows the time-averaged vapor volume fraction inside the injector orifice versus the square root of the difference between injection and back pressures. Results correspond to both the barotropic and thermal cases. As shown, the barotropic and complete formulation approaches follow similar trends. Due to the higher average temperatures and consequently higher vapour pressures found when considering thermal effects, cavitation growth is enhanced and thus found to be greater than in the barotropic

approach. For both cases the volume of vapour formed inside the orifice first increases up to 120MPa and then decreases as the injection pressure increases. This is a rather unexpected result, as it is commonly believed that increasing the injection pressure results to higher velocities, which induce a greater boundary layer separation inside the orifice; in turn, flow separation would lead to an enhanced contraction of the flow and thus, a greater reduction in the static pressure; if this is below the local vapour pressure, more cavitation would be expected. However, the trend observed do not follow this reasoning. At low injection pressures, cavitation grows inside the orifice with injection pressure. Meanwhile, as shown previously in Figure 4.12, pressures in the orifice also increase with the injection pressure. From a certain point onwards, however, increasing the pressures in the orifice appears to inhibit the growth of cavitation. Figure 4.13(b) quantifies the volume occupied by different ranges of pressure inside the orifice. As seen, pressures greater than the back pressure, i.e. P=5MPa, occupies from ~20% at 60MPa up to ~55% for 450MPa. The volume with pressures below 5MPa but above the vapor pressure decreases from 65% at 60MPa down to 35% for 450MPa. Finally, the volume occupied by pressures lower than the vapor pressure then shows the same result as the average vapor volume fraction.

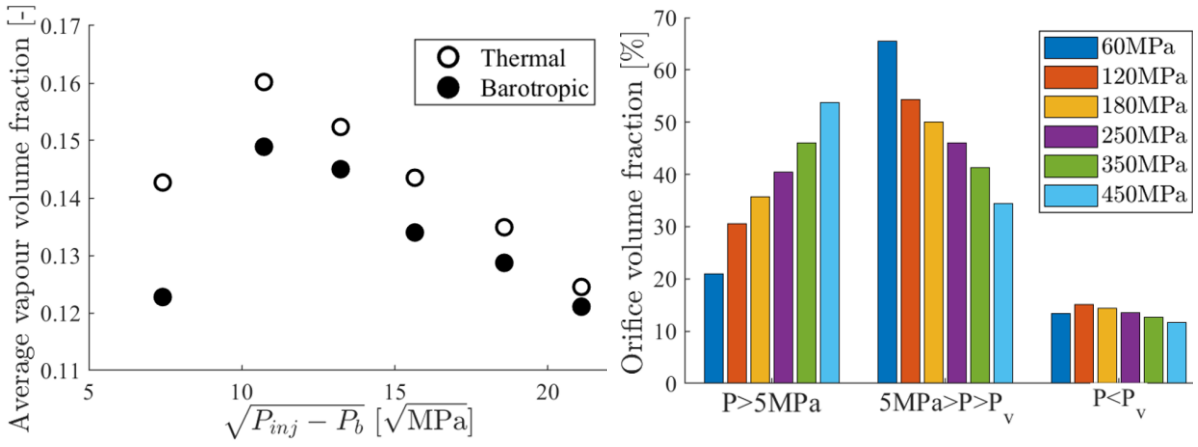

(a) (b)

Figure 4.13. (a) Time-averaged vapor volume fraction inside the injector orifice versus the square root of the pressure difference between injection pressure and back pressure. The symbols show the results both for the barotropic approach and those for thermal effects being considered. (b) Orifice volume fraction histogram for different pressure ranges inside the orifice volume when thermal effects are considered.

Various parametric studies have been performed to disprove these results as a numerical artefact; the relevant results are summarised in Figure 4.14 and have included injection into gas, simulations assuming constant fuel viscosity, non-tapering of the nozzle hole and different turbulence models such as the k-omega SST RANS model with the Reboud correction[180]. Although the absolute values of cavitation volume fraction are not the same, as cavitation is significantly dependant on the model and properties used, a similar reduction of cavitation with the injection pressure is observed for all cases.

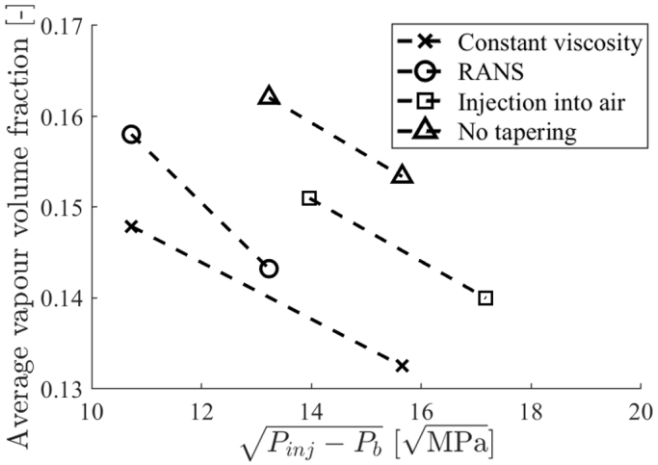

Figure 4.14. Effect of boundary/simulation parameters on calculated vapour volume fraction as function of injection pressure.

The increased pressures found overall, vapor cloud included, also affects the amount of mass vapour within the orifice. Figure 4.15 shows the vapour mass flow rate along the orifice length for all injection pressures and both the barotropic and the thermal cases. Two insets of the temperature distribution are added to the thermal case, corresponding to locations of high vapour mass flow rate at 450MPa. On the slices, an isoline showing the location of vapour is also included. The density of the vapour fuel ρ_v is calculated by PC-SAFT during the VLE calculations. As seen, as the injection pressure increases so does the flow rate of vapour mass along the orifice. For instance, at 20% of the orifice length and for the thermal case, the vapour mass flow rate is 0.06mg/s for 60MPa, 0.22mg/s for 180MPa and 1.02mg/s for 450MPa. However, the results for the thermal case are significantly higher than those for the barotropic one, due to the higher temperatures obtained. At 20% of the orifice length, for the barotropic case the vapour mass flow rate is 0.085mg/s for 450MPa, while for the thermal case it is

1.02mg/s. This difference can be explained because, when in vapour-liquid equilibrium, the vapour density increases with temperature. For instance, at 350K the saturated vapour density is 2.5*10^{-3}kg/m^3, at 360K it increases to 5.03*10^{-3}kg/m^3, i.e. a 200% difference, and at 370K it doubles again to 9.9*10^{-3}kg/m^3. This can be also observed on the two peaks found at approximately 40 and 75% of the orifice length, for the thermal case. In these locations, as shown by the insets, a significant increase in temperature is found, which produce also an increase in the vapour density.

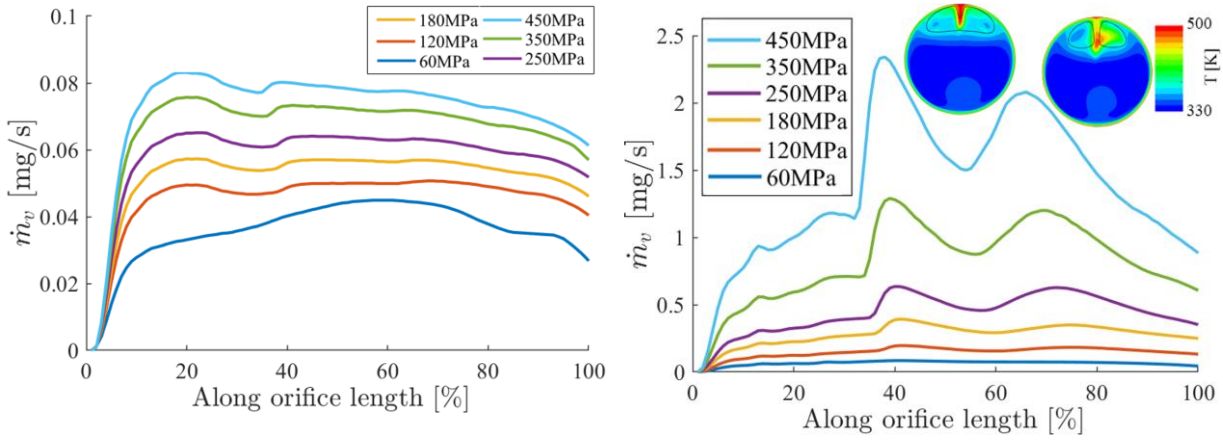

(a) Barotropic (b) Thermal

Figure 4.15. Time-averaged vapour mass flow rate along the orifice length for both (a) barotropic and (b) thermal cases, at all injection pressures. Two insets of the temperature distribution are added to the thermal case, corresponding to locations of high vapour mass flow rate at 450MPa. On the slices, an isoline showing the location of vapour is also included.

Figure 4.16 shows the slope of the vapour mass flow rate along the orifice length, thus presenting the locations of net evaporation (positive values) and condensation (negative values) per meter of the orifice length as the fuel cavitates within the nozzle hole. As already seen in Figure 4.15, overall values are higher in the thermal case due to the dependence of the vapour density on temperature, particularly at 40% and 75% of the orifice length. Nevertheless, both values for evaporation and condensation are seen to increase with injection pressure for the barotropic and thermal cases. This is clearly shown in the thermal case by the amplitude of the observed positive and negative peaks. For instance, at the entrance there is a value for evaporation of 0.6g/s·m for 60MPa, 2.7g/s·m for 180MPa and 13g/s·m for 450MPa, while at ~45% of the orifice length there is a value for condensation of 0.07g/s·m for 60MPa, 0.62g/s·m for 180MPa and 6g/s·m for 450MPa. Moreover, while for the

barotropic case most of the evaporation (values for the 450MPa case) is observed at the beginning of the orifice, with a value of 1.2g/s·m, followed by small positive values at 40% of 0.1g/s·m and of 0.01g/s·m at 60%, for the thermal case the peak in evaporation occurs at 40% of the orifice length, with a significantly higher value of 32g/s·m, followed by a smaller value of 13g/s·m at the entrance and of 7g/s·m at 60%.

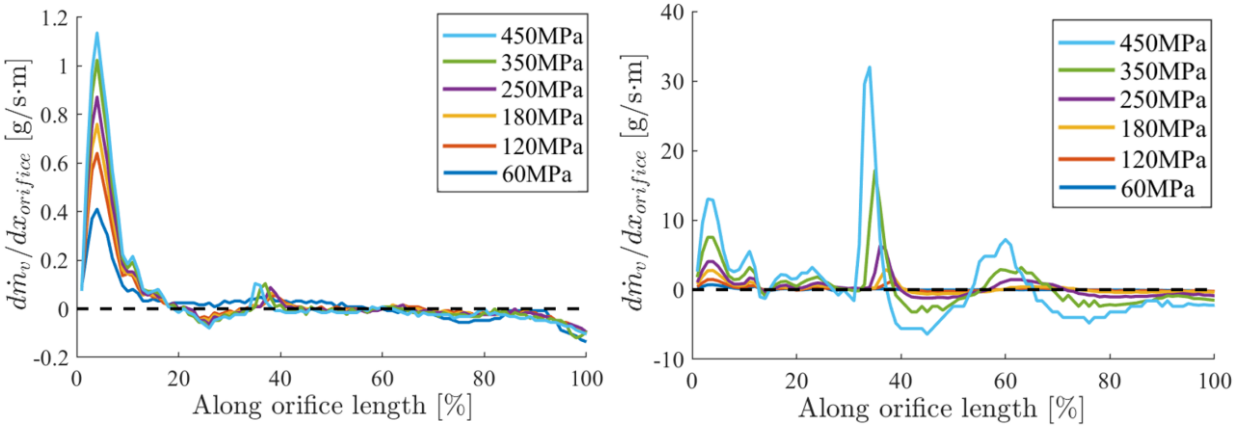

(a) Barotropic (b) Thermal

Figure 4.16. Slope of the vapour mass flow rate along the orifice length, showing locations of net evaporation (positive) and condensation (negative), for both barotropic and thermal cases. A dashed horizontal line is added at value 0, for reference.

An additional interesting finding is related to the influence of varying simultaneously the injection and back pressures on cavitation vapour volume fraction[181] but keeping the cavitation number fixed; this is defined as:

$$CN = \frac{P_{inj} - P_b}{P_b - P_{sat}} \tag{4.17}$$

The cavitation number chosen is 35, the same obtained for the original case of 180MPa. For keeping constant cavitation number, increasing the injection pressure results to increasing the back pressure and, on the other hand, decreasing the injection pressure results to decreasing back pressure. Figure 4.17 shows that the vapour volume fraction still decreases inside the orifice as the injection pressure increases, even by keeping constant the cavitation number. Thus, for the same injector and fluid, these

results show that a constant cavitation number does not indicate a similar cavity size, but it strongly depends on the absolute value of the injection and back pressure values used.

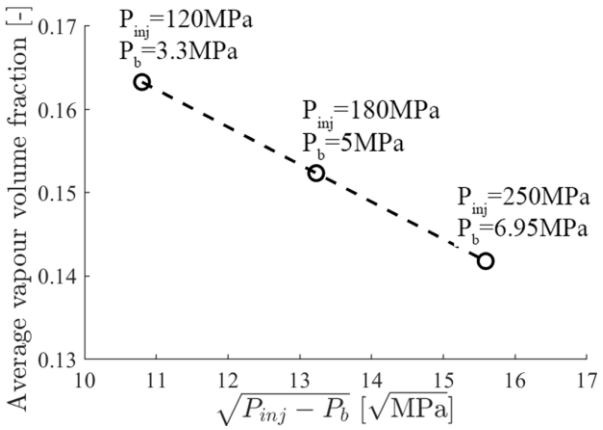

Figure 4.17. Time-averaged vapour volume fraction inside the injector orifice versus the square root of the pressure difference between injection pressure and back pressure. All cases have the same cavitation number, CN=35. Thermal effects are considered.

4.2.4 Preferential cavitation

One of the benefits of using PC-SAFT coupled with a VLE algorithm is that it allows the calculation of the vaporised amount of each individual fuel component. As an example, Figure 4.18 shows the vapour mass fraction at 350K of the Diesel surrogate (dashed line) and of four representative components (the heaviest, lightest and two intermediates, in solid lines), as a function of the specific volume, i.e. the fuel vaporises as it expands. As shown, the mixture vaporises at a variable rate as it expands, while each component vaporises as well at their distinct rhythm. The lightest component, i.e. 1,2,4-trimethylbenzene, is seen to vaporise at a higher rate than the mixture and completely vaporises significantly sooner. The heaviest one, i.e. n-octadecane, vaporises much slower than the mixture, but reaches the complete vaporisation at the same time. The intermediate components vaporise at rates in between the previous ones, depending on their different properties.

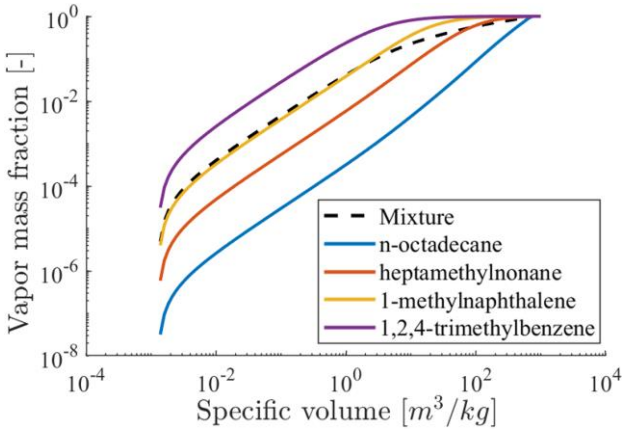

Figure 4.18. Mass fraction of vaporised surrogate and representative components (the heaviest, lightest and two intermediate) as a function of specific volume for a 0D expansion of the fuel at 350K.

As the volume fraction per component cannot be retrieved from the equation of state, mass fractions are used here. The vaporised mass fraction of every component v_i, is calculated using the mass vapour fraction of the mixture θ, the composition of the vapour phase $\boldsymbol{x}$ and the composition of the total mixture $\boldsymbol{z}$ by:

$$v_i = \theta * x_i / z_i \tag{4.18}$$

Figure 4.19 shows isosurfaces of the mass vapour fraction for selected components. The mass vapour fraction is selected so that the isosurface for trimethylbenzene coincides to that of the mixture 50% vapor volume fraction. As shown, trimethylbenzene is the maximum cavitating component and the heaviest one, i.e. octadecane, cavitates significantly less and mostly at the entrance of the orifice, where the flow separates, and cavitation is stronger. No significant amount of the 5 heavier components are found in the vortex cavitation cloud found at 60MPa. Moreover, as the injection pressure increases, every component is seen to cavitate further inside the cavitating cloud, observable on the isosurface for octadecane, due to both the higher pressures and temperatures occurring in the orifice.

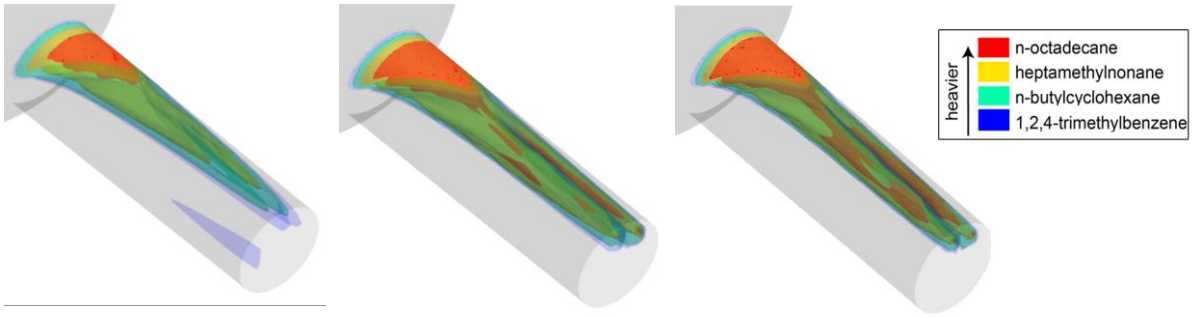

(a) 60MPa (b) 180MPa (c) 450MPa

Figure 4.19. Effect of the injection pressure on the partial vaporisation of a selection of Diesel surrogate components. Results are time-averaged and thermal effects are considered. Per case, the mass fraction used for the isosurfaces is obtained as that for trimethylbenzene which gives the same surface than the one for the mixture 50% vapor volume fraction.

Figure 4.20 shows the mass composition of the cavitating cloud inside the orifice for all injection pressures studied. Results are time-averaged and consider thermal effects. Table 4.4 shows the values in a table fashion. It is important to note that the vapor mass composition of the vapour cloud is dependent on the initial composition of the fuel, included on the second column. In any case, lighter components are the ones found to be in greater amount due to their higher volatility. As seen, in all cases the 4 lightest components compose more than 75% of the vapour mass. The compound most present in the total mass of the Diesel surrogate, heptamethylnonane with 35% in mass fraction, is not the one found in greater amount in vapour phase, due to its heavy nature. The mass of vapor from this is only 3.44% of the mass of total vapor at 60MPa and up to 12.5% at 450MPa. Similar observations can be drawn from octadecane, which covers 27% of the total mass of the fuel, but in the vapor cloud it is just above 1%. On the other hand, the lighter butylcyclohexane with a 11% of the total fuel mass, covers 23% and ~24% of the mass of vapor at 60MPa and 450MPa, respectively. The lightest component in the surrogate, 1,2,4-trimethylbenzene, which mass is 5% of the initial fuel mass, when vaporised it provides 23% of the total mass of vapor at 450MPa. As seen previously in Figure 4.16, the total mass of vapour, and as a result the mass of vapour of all components, increases with injection pressure. Moreover, due to the heterogeneity of the cavitation process predicted by PC-SAFT, increasing the total mass of total vapor does not result in a proportional increment of the vapour mass

of each component. Each component, however, cavitates differently depending on its own molecular structure and temperature/pressure conditions. This influences the final mass composition of the vapour cloud, as some components may decrease its part on the vapor composition with injection pressure while effectively increasing its cavitating mass. This can be seen in the vapor mass composition provided by trimethylbenzene, tetralin and trans-decalin, which decreases, and that of 1-methylnaphthalene, heptamethylnonane, n-hexadecane and n-octadecane, which increases with injection pressure.

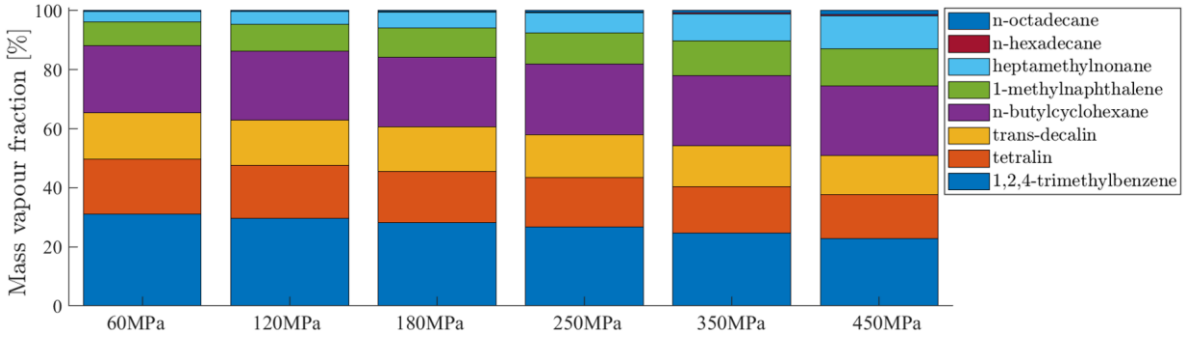

Figure 4.20. Time-averaged predictions for the vaporised mass composition of the vapor cloud, in a stacked fashion, at all injection pressures. Thermal effects are considered.

		P_inj [MPa]					
Component	**z [% mass]**	**60**	**120**	**180**	**250**	**350**	**450**
n-octadecane	27.308	0.2416	0.2575	0.3487	0.5068	0.8566	1.3300
n-hexadecane	3.2477	0.1050	0.1338	0.1822	0.2517	0.3784	0.5209
heptamethylnonane	35.124	3.4426	4.2924	5.3811	6.7659	8.9891	11.152
1-methylnaphthalene	10.877	8.1457	9.0432	9.8387	10.675	11.723	12.463
n-butylcyclohexane	10.815	22.619	23.278	23.589	23.805	23.807	23.550
trans-decalin	4.0392	15.721	15.431	15.051	14.601	13.894	13.232
tetralin	3.8009	18.597	18.028	17.437	16.743	15.733	14.834
1,2,4-trimethylbenzene	4.7883	31.128	29.537	28.174	26.652	24.619	22.918

Table 4.4. Time-averaged predictions for the vaporised mass composition of the vapor cloud, at all injection pressures. The initial surrogate mass composition is included. Thermal effects are considered.

4.3 Summary and Conclusions

This section has set out to investigate the in-nozzle flow characteristics for a Diesel injector when the injection pressure increases up to 450MPa. For this, the 8-component Diesel surrogate from the previous sections is modelled using the PC-SAFT EoS and its properties precalculated and included in a table format for its use during the CFD simulations. Two different assumptions have been utilised, one neglecting friction-induced thermal effects, following an isentropic evolution, and another where the energy conservation equation is solved, and thus thermal effects are considered. The in-nozzle flow and preferential cavitation of the components has been estimated and its evolution with the injection pressure has been discussed. The findings from this study make several contributions to the current literature. First, it is the first work studying the effect of cavitation at extreme injection pressures up to 450MPa. Secondly, it is the first work using the molecular-based PC-SAFT equation of state for the modelling of the Diesel fuel properties. Finally, it is also the first work predicting the preferential cavitation of the components in a Diesel injector.

As expected, the mass flow rate increases linearly with the square root of the difference between injection and back pressures. No significant differences in mass flow rate were observed for a refined mesh. Moreover, the values for the thermal and the barotropic cases are found to be very close. Due to the temperature increase, the density of the fluid drops for the thermal case, but so does the viscosity, enhancing the velocity of the flow. As a result, both effects offset each other, and the mass flow rate does not change significantly. In-nozzle vorticity increases as well, finding the highest values close to the walls and in the vapour-liquid equilibrium phase. Due to this increase, thermal effects are enhanced, which affects the flow by making it diverge from the isentropic evolution. Although the average temperature of the fuel is increasing, cooling exists in the core of the flow, as the fuel expands undisturbed by velocity gradients or any other source of heating. The temperature peak was found at the upper surface of the orifice, close to its entrance. This peak in temperature corresponds to

complete fuel vaporisation locally, which then heats up due to the vapour's lower mass, thermal conductivity and heat capacity. The increase in the overall temperature of the fuel affects also the vapor pressure of the fuel, which is seen to increase with the injection pressure.

One of the more significant findings to emerge from this study is that in-nozzle cavitation volume fraction decreases with injection pressure, although the mass of fuel cavitating increases. This trend has been explained by observing the pressure distribution within the nozzle orifice, which increase significantly with injection pressure and effectively decrease the growth of cavitation. This increase in the pressure and temperatures within the orifice also affects, as a result, the vapour mass flow rate and the net evaporation and condensation per meter of the orifice length as the fuel cavitates within the nozzle hole, which increase significantly with the injection pressure.

The second major finding of this work is related to the preferential cavitation of each fuel components. Due to the multicomponent nature of the studied Diesel fuel, its phase-change is a complex process, which can be captured with an appropriate equation of state. In this work, it was shown that each component cavitates at a distinct rhythm, different to that of the mixture and to that of the other components. The composition of the fuel vapour shows that the lighter components cavitate at a significantly greater amount than the heavy ones. With increasing injection pressure, all fuel components cavitate in higher mass quantities due to the higher densities of the fuel at the pressures developing in the nozzle orifice.

5. Conclusions and future work

5.1 Conclusions

On this thesis, the influence of properties variation of Diesel fuel in the range of injection pressures from 60MPa to 450MPa on nozzle flow and cavitation is investigated. Diesel fuel properties are modelled with PC-SAFT using an 8-component surrogate and this equation of state is coupled with a vapour-liquid equilibrium algorithm. As a result, the preferential vaporisation of each component within the mixture can be also calculated.

At first, the properties of four surrogates proposed by Mueller et al.[1] were modelled using the PC-SAFT EoS to test the performance of this model to predict density, volatility, and viscosity. The pure component parameters needed for PC-SAFT were obtained either from the literature or were calculated using correlations based on literature parameters (LC-PC-SAFT) or were calculated using a group contribution method (GC-PC-SAFT). Good predictions were obtained by using both of these methods at broad ranges of temperatures and pressures, for density and viscosity, when compared with experimental data for a variety Diesel fuels. Regarding volatility, predicted temperatures at low vapour fractions where found too high and too low for high vapour fractions. Overall, the 8-component surrogate modelled with the GC-PC-SAFT method was the closest in agreement with experimental data, demonstrating the predictive capability of PC-SAFT for Diesel fuels at extreme operating conditions.

Then, the PC-SAFT EoS was coupled with a Vapor-Liquid Equilibrium algorithm, using specified composition, density and temperature as inputs. This algorithm was tested on several single and multicomponent cases. Newton iterations were used to calculate the global minimum of the Helmholtz free energy in two stages, i.e. stability and flash. Two different methods, depending on the iterative variables used, were studied: one based in number of moles and volume (NVL) and another based in the logarithm of the equilibrium constants (lnK). The lnK method showed the least number of iterations needed for convergence but also the longest computational time required. Moreover,

the lnK method failed continuously for single components or for mixtures with similar components, as with the 8-component Diesel surrogate. With respect to Peng-Robinson, PC-SAFT showed higher requirements regarding computational time. Validation against experiments showed good agreement of the numerical model.

Lastly, in-nozzle flow characteristics for a Diesel injector when the injection pressure increases up to 450MPa were investigated, using the 8-component surrogate. Its properties were precalculated and included in a table format for its use during the CFD simulations. An approach where the energy conservation equation is solved, and thus friction-induced heating is considered, is used and compared against a barotropic one, following an isentropic evolution. As injection pressure increases, vorticity, density and viscosity inside the injector is found to increase as well. For the thermal case, the temperatures and vapour pressure inside the orifice are found to also increase significantly, thus making it diverge from the isentropic evolution. In-nozzle cavitation volume fraction was seen to decrease with injection pressure, although the mass of fuel cavitating increased, due to the higher pressures found in the orifice as the injection pressure increases, effectively decreasing the growth of cavitation. The composition of the fuel vapour showed that the lighter components cavitate at a significantly greater amount than the heavy ones, although all components cavitated in higher mass quantities with injection pressure.

5.2 Future Work

The use of the state-of-the-art PC-SAFT EoS for the calculation of multiphase thermodynamic and thermophysical properties and its use in CFD simulations provides a significant potential for future research. My recommendations for future work are:

- PC-SAFT and its use in VLE calculations should be headed towards more complex mixtures, resourcing to the latest applications of PC-SAFT introducing associating[163], multipolar [164] [165]

and/or aqueous ionic liquid solutions[166], as the accuracy of this molecular-based EoS is of great value for academic and industrial applications. For instance, associating and multipolar terms are needed for the correct characterisation of biodiesels, which are renewable and biodegradable alternative fuels. These are usually blended with Diesel fuels to reduce tailpipe emissions. On the other hand, biological substances, used for instance in waste and drinking water treatment or fertilizer production, could be accurately modelled by this equation of state and its multiphase properties could be calculated with the VLE algorithm. Moreover, chemical equilibrium could be coupled with thermodynamic equilibrium for the accurate modelling of processes involving reactions.

- The results for high injection pressures need to be validated against experiments, thus experimental work should be done particularly on the effect on cavitation and temperature effects at these extreme conditions. Also, the potential effects on erosion and emissions should be assessed, as the decrease in vapour volume fraction with injection pressure may have beneficial consequences. The effect of additives on the flow characteristics is a topic where this research could also be of help, providing an accurate database of Diesel properties which could be coupled with a model introducing the effects of additives in the flow.
- As cavitation influences the Diesel spray in the combustion chamber, CFD research should be headed towards a joint simulation where the flow inside injector and the combustion chamber is calculated in a single domain. Fortunately, it is easier to obtain experimental data from Diesel sprays at extreme injection pressure conditions, thus this could be an indirect way to validate the simulation results at such high injection pressures.

Appendix A

A.1 Results for density

Predictions compared to averaged experimental densities (symbols) of five Diesel fuels[4] Symbols: circles - 298 K, squares - 323 K, triangles - 348 K, x - 373 K.

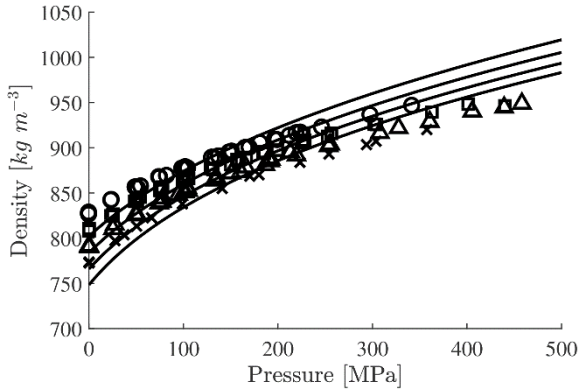

Figure A.1: V0a with LC-PC-SAFT

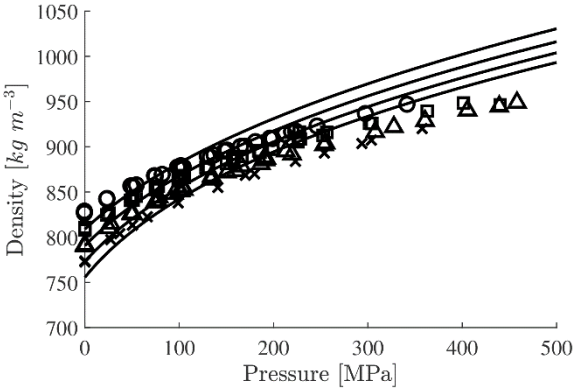

Figure A.2: V0a with GC-PC-SAFT

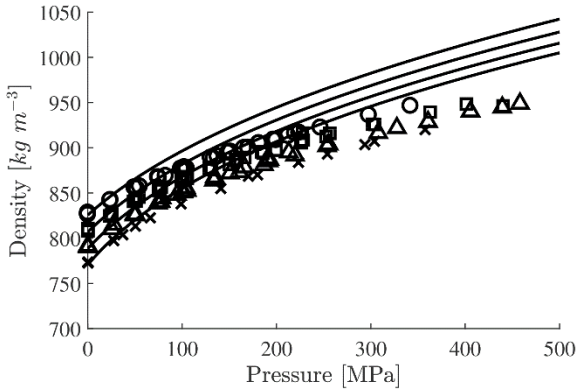

Figure A.3: V0b with LC-PC-SAFT

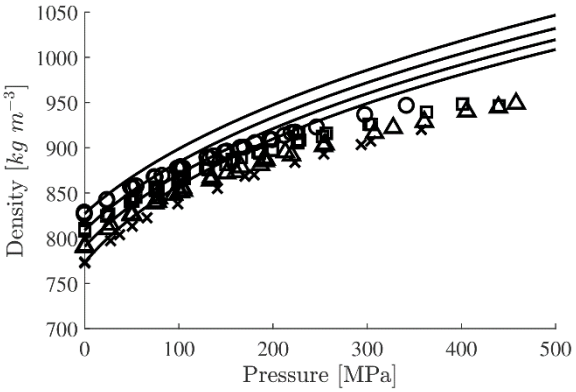

Figure A.4: V0b with GC-PC-SAFT

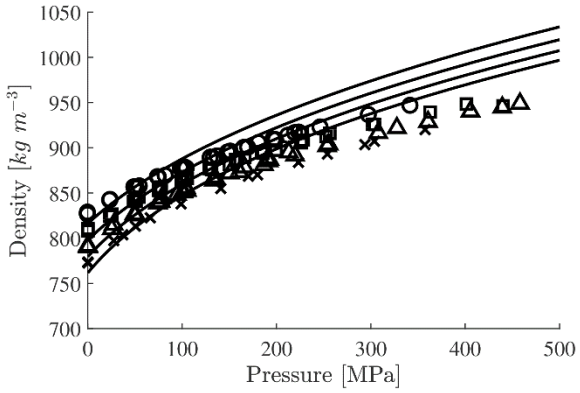

Figure A.5: V1 with LC-PC-SAFT

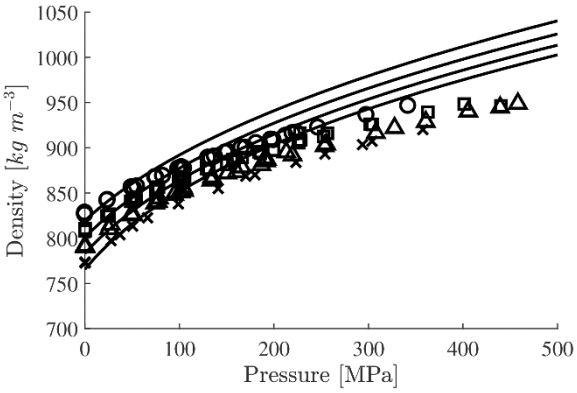

Figure A.6: V1 with GC-PC-SAFT

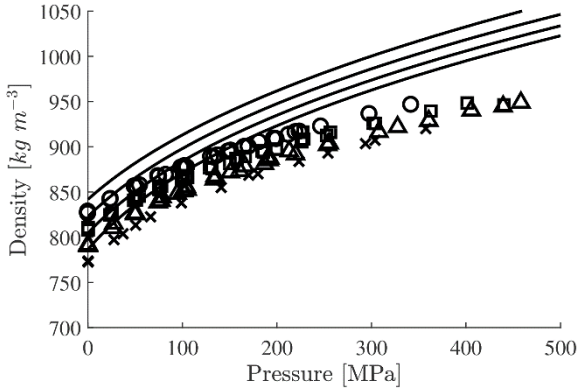

Figure A.7: V2 with LC-PC-SAFT

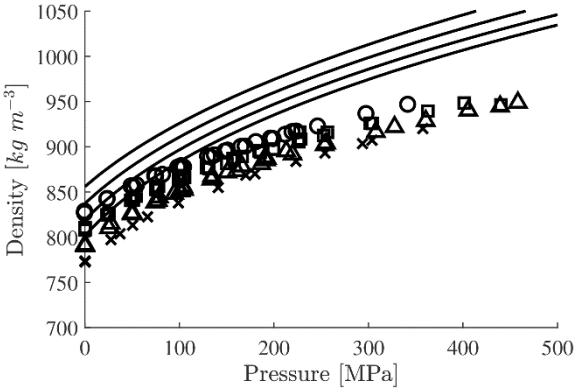

Figure A.8: V2 with GC-PC-SAFT

A.2 Results for viscosity

Predictions compared to experimental viscosities (symbols) of diesel fuels 1 and 3-5 reported[4]. Symbols: circles - 298 K, squares - 323 K, triangles - 348 K, x - 373 K.

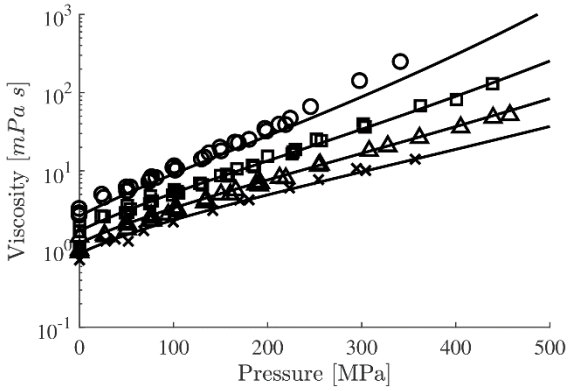

Figure A.9: V0a with LC-PC-SAFT

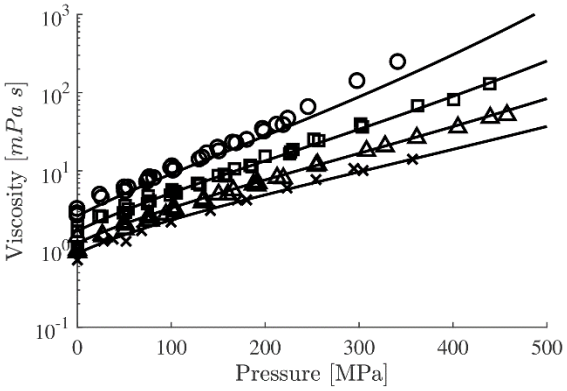

Figure A.10: V0a with GC-PC-SAFT

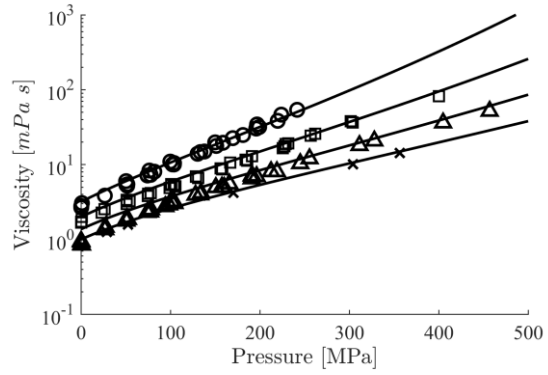

Figure A.11: V0b with LC-PC-SAFT

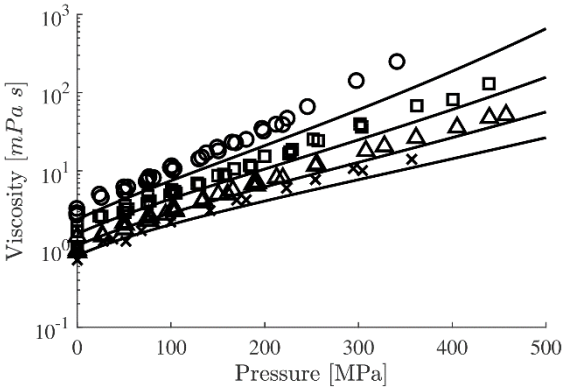

Figure A.12: V0b with GC-PC-SAFT

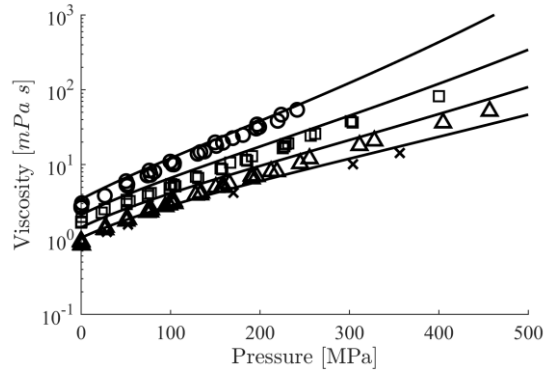

Figure A.13: V1 with LC-PC-SAFT

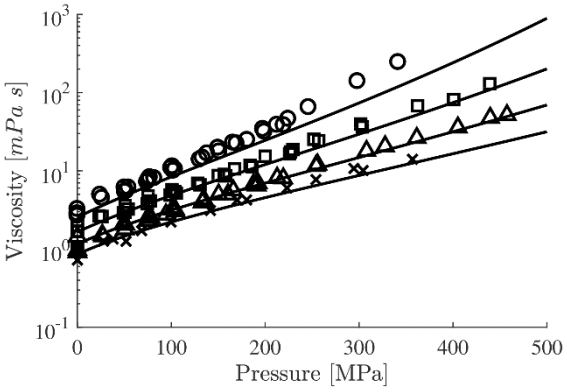

Figure A.14: V1 with GC-PC-SAFT

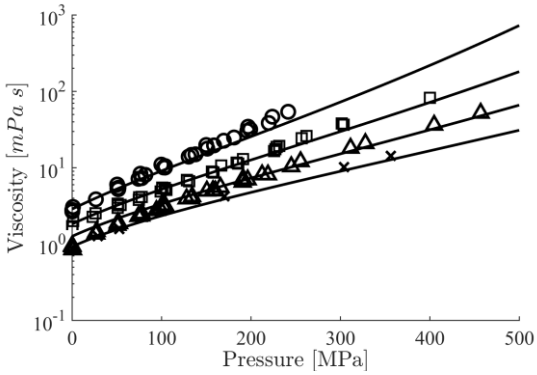

Figure A.15: V2 with LC-PC-SAFT

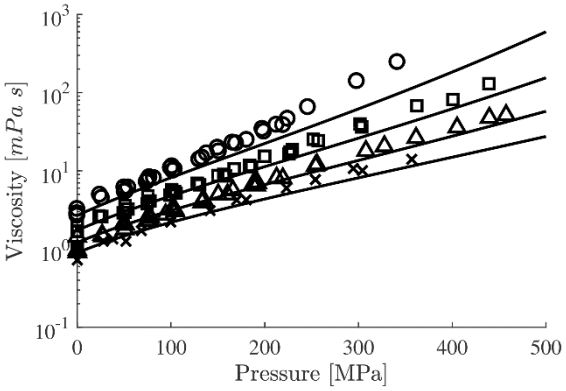

Figure A.16: V2 with GC-PC-SAFT

Appendix B

B.1 List of hydrocarbons used in the Fifty hydrocarbon mixture

Methane, ethane, propane, butane, pentane, hexane, heptane, octane, nonane, decane, undecane, dodecane, tridecane, tetradecane, pentadecane, hexadecane, heptadecane, octadecane, isopentane, 2,2-dimethylbutane, 2,3-dimethylbutane, 2-methylpentane, 3-methylpentane, 2,2,3-trimethylbutane, 3-ethylpentane, 2,2-dimethylpentane, 2,4-dimethylpentane, 3,3-dimethylpentane, 2,2,3-trimethylpentane, 2,3-dimethylhexane, 3,4-dimethylhexane, 2,3,4-trimethylpentane, 2,3,3-trimethylpentane, 2,2-dimethylhexane, 2,2,4-trimethylpentane, 2-methylheptane, 3-methylheptane, 4-methylheptane, 2,5-dimethylhexane, 2-methyl-3-ethylpentane, 3-methyl-3-ethylpentane, 2,2,3,3-tetramethylbutane, 3-ethylhexane, 2,4-dimethylhexane, 3,3-dimethylhexane, 2,2,4,4-tetramethylpentane, 2,2,5-trimethylhexane, 2,2-dimethylheptane, 2,2-dimethyl-3-ethylpentane, 2-methyloctane, 2,2,3,3-tetramethylpentane, 2,2,3,4-tetramethylpentane, 2,3,3,4-tetramethylpentane, 2,4,4-trimethylhexane.

B.2 PC-SAFT and critical parameters

Compound	m[−]	σ[˚A]	$\epsilon/k_B[K]$	T_{crit}[K]	$P_{crit}[MPa]$	ω[−]
carbon dioxide	2.073	2.785	169.21	304.00	7.375	0.239
nitrogen	1.205	3.313	90.960	126.20	3.398	0.037
n-methane	1.000	3.704	150.03	190.56	4.599	0.011
n-ethane	1.607	3.521	191.42	308.95	4.463	0.099
n-propane	2.002	3.618	208.11	369.83	4.248	0.153
n-butane	2.332	3.709	222.88	432.50	4.218	0.200
n-pentane	2.690	3.773	231.20	469.70	3.825	0.252
isopentane	2.562	3.830	230.75	467.89	3.758	0.229
n-hexane	3.058	3.798	236.77	519.33	3.543	0.300
2,2-dimethylbutane	2.601	4.004	243.51	497.18	3.439	0.233
2,3-dimethylbutane	2.685	3.955	246.07	509.75	3.539	0.248
2-methylpentane	2.932	3.854	235.58	507.41	3.468	0.278
3-methylpentane	2.885	3.861	240.48	514.35	3.557	0.273
n-heptane	3.483	3.805	238.40	552.10	3.249	0.350
2,2,3-trimethylbutane	2.737	4.091	258.65	540.45	3.320	0.250
3-ethylpentane	3.140	3.907	249.17	552.74	3.367	0.311
2,2-dimethylpentane	2.955	4.009	246.3	532.35	3.203	0.287
2,4-dimethylpentane	3.143	3.925	238.91	530.19	3.182	0.304
3,3-dimethylpentane	2.892	4.036	254.43	544.71	3.290	0.269
n-octane	3.818	3.837	242.78	583.06	3.019	0.399
2,2-dimethylhexane	3.448	3.960	243.00	560.42	2.958	0.339
2,3-dimethylhexane	3.463	3.930	249.02	575.37	3.093	0.347
3,4-dimethylhexane	3.403	3.943	253.13	580.66	3.151	0.347
2,5-dimethylhexane	3.548	3.928	240.85	550.00	2.490	0.357
2,4-dimethylhexane	3.495	3.945	242.99	553.50	2.560	0.344
3,3-dimethylhexane	3.220	4.018	256.55	562.00	2.650	0.320

2,2,3-trimethylpentane	3.095	4.067	260.59	574.59	3.152	0.298
2,3,4-trimethylpentane	3.215	4.016	257.82	580.66	3.151	0.316
2,3,3-trimethylpentane	3.017	4.100	268.0	584.70	3.216	0.291
2,2,4-trimethylpentane	3.141	4.086	249.77	554.19	2.949	0.304
2-methylheptane	3.704	3.868	241.21	559.60	2.480	0.378
3-methylheptane	3.626	3.881	245.39	563.60	2.550	0.371
4-methylheptane	3.654	3.870	243.36	561.70	2.540	0.371
2-methyl-3-ethylpentane	3.332	3.961	254.65	567.80	2.870	0.248
3-methyl-3-ethylpentane	3.098	4.068	266.66	567.80	2.870	0.248
2,2,3,3-tetramethylbutane	2.924	4.142	266.48	567.80	2.870	0.248
3-ethylhexane	3.566	3.885	247.45	565.40	2.610	0.362
n-nonane	4.208	3.845	244.51	609.28	2.806	0.445
1,2,4-trimethylbenzene	3.610	3.749	284.25	649.10	3.232	0.377
2,2,4,4-tetramethylpentane	3.175	4.209	262.92	574.60	2.490	0.314
2,2,5-trimethylhexane	3.762	3.984	241.1	569.80	2.490	0.314
2,2-dimethylheptane	3.871	3.950	243.3	577.80	2.350	0.383
2,2-dimethyl-3-ethylpentane	3.450	4.070	259.84	577.80	2.350	0.383
2-methyloctane	4.071	3.889	243.85	587.00	2.310	0.423
2,2,3,3-tetramethylpentane	3.125	4.179	279.57	607.60	2.740	0.304
2,2,3,4-tetramethylpentane	3.249	4.146	267.81	592.70	2.530	0.301
2,3,3,4-tetramethylpentane	3.184	4.161	277.47	607.10	2.530	0.309
2,4,4-trimethylhexane	3.406	4.109	258.97	617.70	2.670	0.309
n-decane	4.663	3.838	243.87	617.70	2.110	0.489
tetralin	3.088	3.996	337.46	720.00	3.650	0.304
trans-decalin	3.291	4.067	307.98	687.05	3.140	0.272
n-butylcyclohexane	3.682	4.036	282.41	667.00	2.570	0.274
n-undecane	4.908	3.889	248.82	654.91	2.432	0.537
1-methylnaphthalene	3.422	3.901	337.14	772.00	3.570	0.334
n-dodecane	5.306	3.896	249.21	673.26	2.265	0.576
n-tridecane	5.688	3.914	249.78	690.05	2.102	0.618
n-tretadecane	5.900	3.940	254.21	710.38	2.029	0.644
n-pentadecane	6.286	3.953	254.14	723.97	1.891	0.685
n-hexadecane	6.669	3.944	253.59	720.60	1.419	0.747
heptamethylnonane	5.603	4.164	266.46	692.00	1.568	0.548
n-heptadecane	6.981	3.968	255.65	750.78	1.697	0.753
n-octadecane	7.438	3.948	254.90	745.26	1.214	0.795

B.3 Non-zero binary interaction parameters

CO_2-C_{10}	0.1329
N_2-C_1	0.0280
N_2-C_3	0.0760
N_2-C_{10}	0.0560
N_2-C_{12}	0.1446
C_1-C_3	0.0560
C_1-C_5	0.0240
C_1-C_{10}	0.0560

B.4 Helmholtz Free Energy and its derivatives needed for Density-Temperature Multiphase calculations

The PC-SAFT EoS parameters per component are the number of segments m_i, the diameter of the segments, σ_i and an energy related parameter ϵ_i.

The Helmholtz free energy A^{res} is the starting point in PC-SAFT, as all other properties can be obtained as derivatives of A^{res}. In the following, a tilde (~) will be used for reduced quantities, and caret symbols (^) will indicate molar quantities. The reduced Helmholtz free energy, for example, is given by

$$\tilde{a^{res}} = \frac{A^{res}}{NkT}$$

while in terms of the molar quantity:

$$\tilde{a}^{res} = \frac{\hat{a}^{res}}{RT}$$

The "natural" variables of PC-SAFT in this formulation are Temperature T, molecular density ρ and molar fraction x_i.

The molecular density is related to the molar density $\hat{\rho}$ by:

$$\hat{\rho} = \frac{\rho}{N_{AV}}\left(10^{10}\frac{\mathrm{A}}{\mathrm{m}}\right)^3$$

However, in some parts of the formulation the density is used in terms of the *packing fraction* η, related to ρ by

$$\eta = \frac{\pi}{6}\rho\sum_{i=1}^{n_c} x_i m_i d_i^3$$

where the temperature-dependent segment diameter d_i is given by:

$$d_i = \sigma_i\left[1 - 0.12\exp\left(-3\frac{\epsilon_i}{kT}\right)\right]$$

Then, in the context of PC-SAFT the derivatives with respect of density are related by:

$$\rho\frac{\partial}{\partial\rho}|_{T,\boldsymbol{x}} = \eta\frac{\partial}{\partial\eta}|_{T,\boldsymbol{x}}$$

$$\rho^2\frac{\partial^2}{\partial\rho^2}|_{T,\boldsymbol{x}} = \eta^2\frac{\partial^2}{\partial\eta^2}|_{T,\boldsymbol{x}}$$

B.4.1 Change of variables from volume and moles to density and composition

During the flash method, the derivatives are described in terms of volume and moles, however they need to be changed to density and composition for PC-SAFT

First, the composition and density are described in terms of moles and volume

$$x_i = \frac{n_i}{\sum_k n_k}$$

$$\rho = \frac{\hat{\rho} N_{AV}}{\left(10^{10}\frac{\text{Å}}{m}\right)^3} = \frac{\frac{n_0}{V} N_{AV}}{\left(10^{10}\frac{\text{Å}}{m}\right)^3} = \frac{\sum_k n_k N_{AV}}{V\left(10^{10}\frac{\text{Å}}{m}\right)^3}$$

Therefore, the derivatives can be rewritten using the chain rule

$$\frac{\partial}{\partial V}|_{T,\boldsymbol{n}} = \frac{\partial \rho}{\partial V}|_{T,\boldsymbol{n}} \frac{\partial}{\partial \rho}|_{T,\boldsymbol{x}} = \frac{-\sum_k n_k N_{AV}}{V^2\left(10^{10}\frac{\text{Å}}{m}\right)^3} \frac{\partial}{\partial \rho}|_{T,\boldsymbol{x}} = \frac{-\sum_k n_k N_{AV}}{\left(\frac{\sum_i n_i N_{AV}}{\rho\left(10^{10}\frac{\text{Å}}{m}\right)^3}\right)^2 \left(10^{10}\frac{\text{Å}}{m}\right)^3} \frac{\partial}{\partial \rho}|_{T,\boldsymbol{x}}$$

$$= \frac{-\rho^2\left(10^{10}\frac{\text{Å}}{m}\right)^3}{\sum_k n_k N_{AV}} \frac{\partial}{\partial \rho}|_{T,\boldsymbol{x}}$$

And regarding $\frac{\partial}{\partial n_j}|_{T,V,n_{s\neq j}}$

$$\frac{\partial}{\partial n_j}|_{T,V,n_{s\neq j}} = \frac{\partial}{\partial \rho}|_{T,\boldsymbol{x}} \frac{\partial \rho}{\partial n_j}|_{T,V,n_{s\neq j}} + \sum_i^{n_c} \frac{\partial}{\partial x_i}|_{T,\rho} \frac{\partial x_i}{\partial n_j}|_{T,V,n_{s\neq j}}$$

Where

$$\frac{\partial x_i}{\partial n_j}|_{T,V,n_{s\neq j}} = \frac{\delta_{ij} - x_i}{\sum_k n_k}$$

And

$$\frac{\partial \rho}{\partial n_j}|_{T,V,n_{s\neq j}} = \frac{N_{AV}}{V\left(10^{10}\frac{\text{Å}}{m}\right)^3} = \frac{\rho}{n_T}$$

Thus

$$\frac{\partial}{\partial n_j}|_{T,V,n_{s\neq j}} = \frac{\partial}{\partial \rho}|_{T,\boldsymbol{x}} \frac{\rho}{n_T} + \sum_i^{n_c} \frac{\delta_{ij} - x_i}{n_T} \frac{\partial}{\partial x_i}|_{T,\rho}$$

B.4.2 Helmholtz Free Energy

The residual Helmholtz free energy consists of the hard-chain reference contribution and the dispersion contribution:

$$\tilde{a}^{res} = \tilde{a}^{hc} + \tilde{a}^{disp}$$

B.4.2.1 Hard-Chain Reference Contribution

$$\tilde{a}^{hc} = \overline{m}\tilde{a}^{hs} - \sum_{i=1}^{n_c} x_i (m_i - 1) \ln g_{ii}^{hs}$$

where the $\overline{m}$ is the mean segment number in the mixture.

$$\overline{m} = \sum_{i=1}^{n_c} x_i m_i$$

The Helmholtz free energy of the hard-sphere fluid is given on a per-segment basis

$$\tilde{a}^{hs} = \frac{1}{\zeta_0}\left[\frac{3\zeta_1\zeta_2}{(1-\zeta_3)} + \frac{\zeta_2^3}{\zeta_3(1-\zeta_3)^2} + \left(\frac{\zeta_2^3}{\zeta_3^2} - \zeta_0\right)\ln(1-\zeta_3)\right]$$

and the radial distribution function of the hard-sphere fluid for the $i-i$ pairs is

$$g_{ii}^{hs} = \frac{1}{1-\zeta_3} + \left(\frac{d_i}{2}\right)\frac{3\zeta_2}{(1-\zeta_3)^2} + \left(\frac{d_i}{2}\right)^2\frac{2\zeta_2^2}{(1-\zeta_3)^3}$$

where ζ_n is defined as

$$\zeta_n = \frac{\pi}{6}\rho\sum_{i=1}^{n_c} x_i m_i d_i^n \quad n \in \{0,1,2,3\}$$

Therefore $\eta = \zeta_3$.

B.4.2.2 Dispersion Contribution

The dispersion contribution to the Helmholtz free energy is given by

$$\tilde{a}^{disp} = -2\pi\rho I_1(\eta,\overline{m})\overline{m^2\epsilon\sigma^3} - \pi\rho\overline{m}C_1 I_2(\eta,\overline{m})\overline{m^2\epsilon^2\sigma^3}$$

where it is introduced the abbreviation C_1, defined as

$$C_1 = \left[1 + \overline{m}\frac{8\eta-2\eta^2}{(1-\eta)^4} + (1-\overline{m})\frac{20\eta-27\eta^2+12\eta^3-2\eta^4}{[(1-\eta)(2-\eta)]^2}\right]^{-1}$$

And

$$\overline{m^2\epsilon\sigma^3} = \sum_{i=1}^{n_c}\sum_{j=1}^{n_c} x_i\, x_j m_i m_j \left(\frac{\epsilon_{ij}}{kT}\right)\sigma_{ij}^3$$

$$\overline{m^2\epsilon^2\sigma^3} = \sum_{i=1}^{n_c}\sum_{j=1}^{n_c} x_i\, x_j m_i m_j \left(\frac{\epsilon_{ij}}{kT}\right)^2\sigma_{ij}^3$$

Where conventional combining rules are employed to determine the parameters for a pair of unlike segments.

$$\sigma_{ij} = \frac{1}{2}(\sigma_i + \sigma_j)$$

$$\epsilon_{ij} = \sqrt{\epsilon_i\epsilon_j}(1-k_{ij})$$

The integrals of the perturbation theory are substituted by simple power series in density

$$I_1(\eta,\overline{m}) = \sum_{i=0}^{6} a_i(\overline{m})\eta^i$$

$$I_2(\eta, \overline{m}) = \sum_{i=0}^{6} b_i(\overline{m})\eta^i$$

where the coefficients a_i and b_i depend on the chain length according to

$$a_i(\overline{m}) = a_{0i} + \frac{\overline{m}-1}{\overline{m}} a_{1i} + \frac{\overline{m}-1}{\overline{m}}\frac{\overline{m}-2}{\overline{m}} a_{2i}$$

$$b_i(\overline{m}) = b_{0i} + \frac{\overline{m}-1}{\overline{m}} b_{1i} + \frac{\overline{m}-1}{\overline{m}}\frac{\overline{m}-2}{\overline{m}} b_{2i}$$

The universal model constants for the a0i, a1i, a2i, b0i, b1i, and b2i are given for the model.

i	a_{0i}	a_{1i}	a_{2i}	b_{0i}	b_{1i}	b_{2i}
0	0.9105631445	-0.3084016918	-0.0906148351	0.7240946941	-0.5755498075	0.0976883116
1	0.6361281449	0.1860531159	0.4527842806	2.2382791861	0.6995095521	-0.2557574982
2	2.6861347891	-2.5030047259	0.5962700728	-4.0025849485	3.8925673390	-9.1558561530
3	-26.547362491	21.419793629	-1.7241829131	-21.003576815	-17.215471648	20.642075974
4	97.759208784	-65.255885330	-4.1302112531	26.855641363	192.67226447	-38.804430052
5	-159.59154087	83.318680481	13.776631870	206.55133841	-161.82646165	93.626774077
6	91.297774084	-33.746922930	-8.6728470368	-355.60235612	-165.20769346	-29.666905585

B.4.3 Pressure (Derivative of $\tilde{a}^{res}$ with respect to density)

The first property than can be derived from the Helmholtz Free Energy is the pressure P in Pascals.

$$P = ZkT\rho\left(10^{10}\frac{\text{Å}}{\text{m}}\right)^3$$

where Z is the compressibility factor, which will be derived using the thermodynamic relation

$$Z = 1 + \eta\left(\frac{\partial\tilde{a}^{res}}{\partial\eta}\right)_{T,\boldsymbol{x}} = 1 + \rho\left(\frac{\partial\tilde{a}^{res}}{\partial\rho}\right)_{T,\boldsymbol{x}}$$

Then

$$Z = 1 + \rho\left(\frac{\partial\tilde{a}^{hc}}{\partial\rho}\right)_{T,\boldsymbol{x}} + \rho\left(\frac{\partial\tilde{a}^{disp}}{\partial\rho}\right)_{T,\boldsymbol{x}} = 1 + Z^{hc} + Z^{disp}$$

B.4.3.1 Hard-Chain Reference Contribution

The residual hard-chain contribution to the compressibility factor is given by:

$$Z^{hc} = \rho\left(\frac{\partial\tilde{a}^{hc}}{\partial\rho}\right)_{T,\boldsymbol{x}} = \overline{m}\rho\left(\frac{\partial\tilde{a}^{hs}}{\partial\rho}\right)_{T,\boldsymbol{x}} - \sum_i x_i(m_i - 1)\frac{\rho\left(g_{ii}^{hs}\right)_\rho}{g_{ii}^{hs}}$$

Where

$$\rho\left(\frac{\partial\tilde{a}^{hs}}{\partial\rho}\right)_{T,\boldsymbol{x}} = \eta\left(\frac{\partial\tilde{a}^{hs}}{\partial\eta}\right)_{T,\boldsymbol{x}} = Z^{hs} = \frac{\zeta_3}{1-\zeta_3} + \frac{3\zeta_1\zeta_2}{\zeta_0(1-\zeta_3)^2} + \frac{3\zeta_2^3 - \zeta_3\zeta_2^3}{\zeta_0(1-\zeta_3)^3}$$

And

$$\rho\left(g_{ii}^{hs}\right)_{\rho} = \eta\left(g_{ii}^{hs}\right)_{\eta} = \frac{\zeta_3}{(1-\zeta_3)^2} + \left(\frac{d_i}{2}\right)\left[\frac{3\zeta_2}{(1-\zeta_3)^2} + \frac{6\zeta_2\zeta_3}{(1-\zeta_3)^3}\right] + \left(\frac{d_i}{2}\right)^2\left[\frac{4\zeta_2^2}{(1-\zeta_3)^3} + \frac{6\zeta_2^2\zeta_3}{(1-\zeta_3)^4}\right]$$

B.4.3.2 Dispersion Contribution

The residual dispersion contribution to the compressibility factor is given by:

$$Z^{disp} = \rho\left(\frac{\partial\tilde{a}^{disp}}{\partial\rho}\right)_{T,\boldsymbol{x}} = -2\pi\rho\frac{\partial(\rho I_1)}{\partial\rho}\overline{m^2\epsilon\sigma^3} - \pi\rho\overline{m}\left[C_1\frac{\partial(\rho I_2)}{\partial\rho} + \rho C_{1,\rho}I_2\right]\overline{m^2\epsilon^2\sigma^3}$$

Now, if we have a function $M = M(\rho)$, a relation between its derivative with respect to density and its derivative with respect to the packing fraction as:

$$\frac{\partial\rho M}{\partial\rho} = M + \rho M_{\rho} = M + \eta M_{\eta} = \frac{\partial\eta M}{\partial\eta}$$

Then we can rewrite the dispersion contribution as

$$Z^{disp} = -2\pi\rho\frac{\partial(\eta I_1)}{\partial\eta}\overline{m^2\epsilon\sigma^3} - \pi\rho\overline{m}\left[C_1\frac{\partial(\eta I_2)}{\partial\eta} + \eta C_{1,\eta}I_2\right]\overline{m^2\epsilon^2\sigma^3}$$

Where

$$\frac{\partial(\eta I_1)}{\partial\eta} = \sum_{j=0}^{6} a_j(j+1)\eta^j$$

$$\frac{\partial(\eta I_2)}{\partial\eta} = \sum_{j=0}^{6} b_j(j+1)\eta^j$$

With two new abbreviations: C_2 and Q.

$$\frac{\partial C_1}{\partial\eta} = C_2 = -C_1^2 Q$$

$$Q = \overline{m}\frac{-4\eta^2 + 20\eta + 8}{(1-\eta)^5} + (1-\overline{m})\frac{2\eta^3 + 12\eta^2 - 48\eta + 40}{[(1-\eta)(2-\eta)]^3}$$

B.4.4 Chemical Potential (Derivative of $\tilde{a}^{res}$ with respect to molar fraction)

The residual chemical potential $\hat{\mu}_i^{res}$ can be obtained from

$$\hat{\mu}_i^{res}(T,\rho) = \left(\frac{\partial(n_T\hat{a}^{res})}{\partial n_i}\right)_{T,V,n_{s\neq i}} = \hat{a}^{res} + n_T\left(\frac{\partial(\hat{a}^{res})}{\partial n_i}\right)_{T,V,n_{s\neq i}}$$

now changing the variables to T, ρ, $\boldsymbol{x}$ and normalizing:

$$\frac{\hat{\mu}_i^{res}(T,\rho)}{kT} = \tilde{a}^{res} + \rho\frac{\partial\tilde{a}^{res}}{\partial\rho}\Big|_{T,\boldsymbol{x}} + \sum_i^{n_c}(\delta_{ij} - x_i)\frac{\partial\tilde{a}^{res}}{\partial x_i}\Big|_{T,\rho}$$

$$= \tilde{a}^{res} + (Z-1) + \sum_i^{n_c}(\delta_{ij} - x_i)\frac{\partial\tilde{a}^{res}}{\partial x_i}\Big|_{T,\rho}$$

Then it only comes to the derivative with respect to molar fraction.

$$\left.\frac{\partial \tilde{a}^{res}}{\partial x_j}\right|_{T,\rho,x_{s\neq j}} = \left.\frac{\partial \tilde{a}^{hc}}{\partial x_j}\right|_{T,\rho,x_{s\neq j}} + \left.\frac{\partial \tilde{a}^{disp}}{\partial x_j}\right|_{T,\rho,x_{s\neq j}}$$

B.4.4.1 Hard-Chain Reference Contribution

The residual hard-chain contribution is given by:

$$\frac{\partial \tilde{a}^{hc}}{\partial x_j}|_{T,\rho,x_{s\neq j}} = m_j \tilde{a}^{hs} + \overline{m}\frac{\partial \tilde{a}^{hs}}{\partial x_j}|_{T,\rho,x_{s\neq j}} - \left(m_j - 1\right)\ln\left(g_{jj}^{hs}\right) - \sum_i x_i (m_i - 1)\frac{1}{g_{ii}^{hs}}\frac{\partial g_{ii}^{hs}}{\partial x_j}|_{T,\rho,x_{s\neq j}}$$

With

$$\begin{aligned}\left(\frac{\partial \tilde{a}^{hs}}{\partial x_j}\right)_{T,\rho,x_{s\neq j}} &= \frac{-\zeta_{0,x_j}}{\zeta_0}\tilde{a}^{hs} \\ &+ \frac{1}{\zeta_0}\left[\frac{3\left(\zeta_{1,x_j}\zeta_2 + \zeta_1\zeta_{2,x_j}\right)}{1-\zeta_3} + \frac{3\zeta_1\zeta_2\zeta_{3,x_j}}{(1-\zeta_3)^2} + \frac{3\zeta_2^2\zeta_{2,x_j}}{\zeta_3(1-\zeta_3)^2} + \frac{\zeta_2^3\zeta_{3,x_j}(3\zeta_3-1)}{\zeta_3^2(1-\zeta_3)^3}\right. \\ &\left. + \left(\frac{3\zeta_2^2\zeta_{2,x_j}\zeta_3 - 2\zeta_2^3\zeta_{3,x_j}}{\zeta_3^3} - \zeta_{0,x_j}\right)\ln(1-\zeta_3) + \left(\zeta_0 - \frac{\zeta_2^3}{\zeta_3^2}\right)\frac{\zeta_{3,x_j}}{(1-\zeta_3)}\right]\end{aligned}$$

As we only care about the $i-i$ pairs for the radial distribution,

$$\left(\frac{\partial g_{ii}^{hs}}{\partial x_j}\right)_{T,\rho,x_{s\neq j}} = \frac{\zeta_{3,x_j}}{(1-\zeta_3)^2} + \left(\frac{d_i}{2}\right)\left(\frac{3\zeta_{2,x_j}}{(1-\zeta_3)^2} + \frac{6\zeta_2\zeta_{3,x_j}}{(1-\zeta_3)^3}\right) + \left(\frac{d_i}{2}\right)^2\left(\frac{4\zeta_2\zeta_{2,x_j}}{(1-\zeta_3)^3} + \frac{6\zeta_2^2\zeta_{3,x_j}}{(1-\zeta_3)^4}\right)$$

Where

$$\zeta_{n,x_j} = \frac{\pi}{6}\rho m_j (d_j)^n$$

B.4.4.2 Dispersion Contribution

The residual dispersion contribution for the Helmholtz free energy is given by:

$$\begin{aligned}\left(\frac{\partial \tilde{a}^{disp}}{\partial x_j}\right)_{T,\rho,x_{s\neq j}} &= -2\pi\rho\left[I_{1,x_j}\overline{m^2\epsilon\sigma^3} + I_1\left(\overline{m^2\epsilon\sigma^3}\right)_{x_j}\right] \\ &- \pi\rho\left[\left(m_j C_1 I_2 + \overline{m}C_{1,x_j}I_2 + \overline{m}C_1 I_{2,x_j}\right)\overline{m^2\epsilon^2\sigma^3} + \overline{m}C_1 I_2\left(\overline{m^2\epsilon^2\sigma^3}\right)_{x_j}\right]\end{aligned}$$

where the other derivatives needed are:

$$\left(\overline{m^2\epsilon\sigma^3}\right)_{x_j} = 2m_j\sum_i x_i m_i\left(\frac{\epsilon_{ji}}{kT}\right)\sigma_{ji}^3$$

$$\left(\overline{m^2\epsilon^2\sigma^3}\right)_{x_j} = 2m_j\sum_i x_i m_i\left(\frac{\epsilon_{ji}}{kT}\right)^2\sigma_{ji}^3$$

$$C_{1,x_j} = C_2\zeta_{3,x_j} - C_1^2\left[m_j\frac{8\eta - 2\eta^2}{(1-\eta)^4} - m_j\frac{20\eta - 27\eta^2 + 12\eta^3 - 2\eta^4}{[(1-\eta)(2\eta)]^2}\right]$$

$$I_{1,x_j} = \sum_{i=0}^{6}\left[a_i(\overline{m})i\zeta_{3,x_j}\eta^{i-1} + a_{i,x_j}\eta^i\right]$$

$$I_{2,x_j} = \sum_{i=0}^{6}\left[b_i(\overline{m})i\zeta_{3,x_j}\eta^{i-1} + b_{i,x_j}\eta^i\right]$$

$$a_{i,x_j} = \frac{m_j}{\overline{m}^2}a_{1i} + \frac{m_j}{\overline{m}^2}\left(3 - \frac{4}{\overline{m}}\right)a_{2i}$$

$$b_{i,x_j} = \frac{m_j}{\overline{m}^2}b_{1i} + \frac{m_j}{\overline{m}^2}\left(3 - \frac{4}{\overline{m}}\right)b_{2i}$$

B.4.5 Second derivative of Helmholtz free energy with respect to density

From the definition of the compressibility factor,

$$\left(\frac{\partial Z}{\partial\rho}\right)_{T,\boldsymbol{x}} = \left(\frac{\partial\tilde{a}^{res}}{\partial\rho}\right)_{T,\boldsymbol{x}} + \rho\left(\frac{\partial^2\tilde{a}^{res}}{\partial\rho^2}\right)_{T,\boldsymbol{x}}$$

Then

$$\rho^2\left(\frac{\partial^2\tilde{a}^{res}}{\partial\rho^2}\right)_{T,\boldsymbol{x}} = \rho Z_\rho + \rho\left(\frac{\partial\tilde{a}^{res}}{\partial\rho}\right)_{T,\boldsymbol{x}}$$

Where

$$\rho\frac{\partial Z}{\partial\rho}\Big|_{T,\mathbf{x}} = \frac{\partial Z^{hc}}{\partial\eta}\Big|_{T,\mathbf{x}} + \eta\frac{\partial Z^{disp}}{\partial\eta}\Big|_{T,\mathbf{x}}$$

Following *Are safe results obtained when the PC-SAFT equation of state is applied to ordinary pure chemicals?* we have the density derivative of the compressibility factor.

B.4.5.1 Chain Contribution

$$\left(\frac{\partial Z^{hc}}{\partial\eta}\right)_{T,\mathbf{x}} = \overline{m}\left(\frac{\partial Z^{hs}}{\partial\eta}\right)_{T,\mathbf{x}} - \sum_i x_i(m_i - 1)\left(\frac{\partial K_{ii}}{\partial\eta}\right)_{T,\mathbf{x}}$$

Where

$$\left(\frac{\partial g_{ii}^{hs}}{\partial\eta}\right)_{T,\boldsymbol{x}} = \frac{\rho}{\eta}\left(\frac{\partial g_{ii}^{hs}}{\partial\rho}\right)_{T,\boldsymbol{x}}$$

$$K'_{0,ii} = \left(\frac{\partial K_{0,ii}}{\partial\eta}\right)_{T,\boldsymbol{x}}$$
$$= \frac{1+\eta}{(1-\eta)^3} + 3\left(\frac{d_i}{2}\right)\frac{2\zeta_2(\eta+2) + \zeta_{2,\eta}(1-\eta^2)}{(1-\eta)^4}$$
$$+ 2\left(\frac{d_i}{2}\right)^2\zeta_2\frac{3\zeta_2(\eta+3) - 2\zeta_{2,\eta}(\eta^2+\eta-2)}{(1-\eta)^5}$$

$$K_{ii} = \frac{K_{0,ii}}{g_{ii}^{hs}}$$

Where

$$K_{0,ii} = \rho \left(\frac{\partial g_{ii}^{hs}}{\partial \rho} \right)_{T,\boldsymbol{x}}$$

for the half-sphere contribution:

$$\left(\frac{\partial Z^{hs}}{\partial \eta} \right)_{T,\boldsymbol{x}} = \frac{1}{(1-\eta)^2} + \frac{3\zeta_1\zeta_2}{\zeta_0 \eta} \frac{1+\eta}{(1-\eta)^3} + \frac{6}{(1-\eta)^4} \frac{\zeta_2^3}{\zeta_0 \zeta_3}$$

$$\zeta_{n,\eta} = \frac{\pi}{6} \left(\frac{\partial \rho}{\partial \eta} \right)_{T,\boldsymbol{x}} \sum_{i=1}^{n_c} x_i m_i d_i^n$$

Where

$$\left(\frac{\partial \rho}{\partial \eta} \right)_{T,\boldsymbol{x}} = \frac{6}{\pi} \left(\sum_i x_i m_i d_i^3 \right)^{-1} = \frac{\rho}{\eta}$$

B.4.5.2 Dispersion contribution

Regarding the dispersion contribution:

$$\left(\frac{\partial Z^{disp}}{\partial \eta} \right)_{T,\backslash pmbx} = -2\pi \overline{m^2 \epsilon \sigma^3} \left[\frac{\rho}{\eta} \frac{\partial (\eta I_1)}{\partial \eta} + \rho \frac{\partial^2 (\eta I_1)}{\partial \eta^2} \right] - \pi \overline{m} \overline{m^2 \epsilon^2 \sigma^3} \frac{\rho}{\eta} \left[C_1 \frac{\partial (\eta I_2)}{\partial \eta} + C_2 \eta I_2 \right) + \rho \left(C_1 \frac{\partial^2 (\eta I_2)}{\partial \eta^2} + 2C_2 \frac{\partial (\eta I_2)}{\partial \eta} + \eta I_2 \frac{\partial C_2}{\partial \eta} \right)$$

Where

$$\frac{\partial^2 (\eta I_1)}{\partial \eta^2} = \sum_{i=0}^{6} a_i i \, (i+1) \eta^{i-1}$$

$$\frac{\partial^2 (\eta I_2)}{\partial \eta^2} = \sum_{i=0}^{6} b_i i \, (i+1) \eta^{i-1}$$

$$\frac{\partial C_2}{\partial \eta} = \frac{\partial^2 C_1}{\partial \eta^2} = -2C_1 C_2 Q - C_1^2 \frac{\partial Q}{\partial \eta}$$

$$\frac{\partial Q}{\partial \eta} = \frac{-12\overline{m}(\eta^2 - 6\eta - 5)}{(1-\eta)^6} + \frac{6(\overline{m}-1)(\eta^4 + 8\eta^3 - 48\eta^2 + 80\eta - 44)}{[(1-\eta)(2-\eta)]^4}$$

B.4.6 Second derivative of Helmholtz free energy with respect to mole fraction

Where the general expression reads

$$\left(\frac{\partial^2 \tilde{a}^{res}}{\partial x_k\, \partial x_j}\right)_{T,\rho,x_{s\neq k,j}} = \left(\frac{\partial^2 \tilde{a}^{hc}}{\partial x_k\, \partial x_j}\right)_{T,\rho,x_{s\neq j,k}} + \left(\frac{\partial^2 \tilde{a}^{disp}}{\partial x_k\, \partial x_j}\right)_{T,\rho,x_{s\neq j,k}}$$

B.4.6.1 Hard-Chain Reference Contribution

The residual hard-chain contribution is given by:

$$\left(\frac{\partial^2 \tilde{a}^{hc}}{\partial x_k\, \partial x_j}\right)_{T,\rho,x_{s\neq j,k}}$$
$$= m_k\left(\tilde{a}^{hs}\right)_{x_j} + m_j\left(\tilde{a}^{hs}\right)_{x_k} + \overline{m}\left(\tilde{a}^{hs}\right)_{x_j,x_k} - \left(m_j - 1\right)\frac{\left(g_{jj}^{hs}\right)_{x_k}}{g_{jj}^{hs}} - \left(m_k - 1\right)\frac{\left(g_{kk}^{hs}\right)_{x_j}}{g_{kk}^{hs}}$$
$$- \sum_i x_i (m_i - 1)\left[\frac{\left(g_{ii}^{hs}\right)_{x_k,x_j}}{g_{ii}^{hs}} - \frac{\left(g_{ii}^{hs}\right)_{x_j}\left(g_{ii}^{hs}\right)_{x_k}}{\left(g_{ii}^{hs}\right)^2}\right]$$

As $\left(\tilde{a}^{hs}\right)_{x_i}$ depends on nine parameters $\left(\zeta_n, \zeta_{n,x_i}, \tilde{a}^{hs}\right)$, the chain rule can be used to obtain its derivative:

$$\frac{\partial}{\partial \mathrm{x_j}}\left(\frac{\partial \tilde{\mathrm{a}}^{\mathrm{hs}}}{\partial \mathrm{x_k}}|_{\mathrm{T,\rho,x_{s\neq k}}}\right)_{\mathrm{T,\rho,x_{s\neq j}}}$$
$$= \frac{\partial\left(\tilde{\mathrm{a}}^{\mathrm{hs}}\right)_{\mathrm{x_k}}}{\partial \tilde{\mathrm{a}}^{\mathrm{hs}}}\frac{\partial \tilde{\mathrm{a}}^{\mathrm{hs}}}{\partial \mathrm{x_j}}|_{\mathrm{T,\rho,x_{s\neq j}}} + \sum_{\mathrm{n=0}}^{3}\frac{\partial\left(\tilde{\mathrm{a}}^{\mathrm{hs}}\right)_{\mathrm{x_k}}}{\partial \zeta_{\mathrm{n}}}\frac{\partial \zeta_{\mathrm{n}}}{\partial \mathrm{x_j}}|_{\mathrm{T,\rho,x_{s\neq j}}} + \sum_{\mathrm{n=0}}^{3}\frac{\partial\left(\tilde{\mathrm{a}}^{\mathrm{hs}}\right)_{\mathrm{x_k}}}{\partial \zeta_{\mathrm{n,x_k}}}\cancel{\frac{\partial \zeta_{\mathrm{n,x_k}}}{\partial \mathrm{x_j}}}|_{\mathrm{T,\rho,x_{s\neq j}}}$$

Where

$$\frac{\partial\left(\tilde{a}^{hs}\right)_{x_k}}{\partial \tilde{a}^{hs}} = \frac{-(\zeta_0)_{x_k}}{\zeta_0}$$

$$\frac{\partial\left(\tilde{a}^{hs}\right)_{x_k}}{\partial \zeta_0} = \frac{\zeta_{0,x_k}}{\zeta_0^2}\tilde{a}^{hs} + \frac{\zeta_{3,x_k}}{\zeta_0(1-\zeta_3)}$$
$$+ \frac{1}{\zeta_0^2}\left[-\frac{3\zeta_1\zeta_{2,x_k} + 3\zeta_{1,x_k}\zeta_2}{1-\zeta_3} + \ln(1-\zeta_3)\left(\zeta_{0,x_k} + \frac{2\zeta_2^3\zeta_{3,x_k} - 3\zeta_2^2\zeta_3\zeta_{2,x_k}}{\zeta_3^3}\right)\right.$$
$$\left. - \frac{\zeta_{3,x_k}(\zeta_0 - \zeta_2^3/\zeta_3^2)}{1-\zeta_3} - \frac{3\zeta_2^2\zeta_{2,x_k}}{\zeta_3(1-\zeta_3)^2} - \frac{3\zeta_1\zeta_2\zeta_{3,x_k}}{(1-\zeta_3)^2} - \frac{\zeta_2^3\zeta_{3,x_k}(3\zeta_3 - 1)}{\zeta_3^2(1-\zeta_3)^3}\right]$$

$$\frac{\partial\left(\tilde{a}^{hs}\right)_{x_k}}{\partial \zeta_1} = \frac{1}{\zeta_0}\left[\frac{3\zeta_{2,x_k}}{1-\zeta_3} + \frac{3\zeta_2\zeta_{3,x_k}}{(1-\zeta_3)^2}\right]$$

$$\frac{\partial\left(\tilde{a}^{hs}\right)_{x_k}}{\partial \zeta_2} = \frac{-1}{\zeta_0}\left[-\frac{3\zeta_{1,x_k}}{1-\zeta_3} + \frac{1}{\zeta_3^3}\ln(1-\zeta_3)\left(6\zeta_2^2\zeta_{3,x_k} - 6\zeta_2\zeta_{2,x_k}\zeta_3\right) - \frac{3\zeta_1\zeta_{3,x_k}}{(1-\zeta_3)^2} + \frac{3\zeta_2^2\zeta_{3,x_k}}{\zeta_3^2(1-\zeta_3)}\right.$$
$$\left. - \frac{6\zeta_2\zeta_{2,x_k}}{\zeta_3(1-\zeta_3)^2} - \frac{3\zeta_2^2\zeta_{3,x_k}(3\zeta_3 - 1)}{\zeta_3^2(1-\zeta_3)^3}\right]$$

$$\frac{\partial\left(\tilde{a}^{hs}\right)_{x_k}}{\partial\zeta_3}=\frac{-1}{\zeta_0}\left[\frac{-1}{1-\zeta_3}\left(\zeta_{0,x_k}+\frac{1}{\zeta_3^3}\left(2\zeta_2^3\zeta_{3,x_k}-3\zeta_2^2\zeta_{2,x_k}\zeta_3\right)\right)\right.$$
$$-\ln(1-\zeta_3)\left(\frac{3\zeta_2^2\zeta_{2,x_k}}{\zeta_3^3}+\frac{3}{\zeta_3^4}\left(2\zeta_2^3\zeta_{3,x_k}-3\zeta_2^2\zeta_{2,x_k}\zeta_3\right)\backslash bigg\right)-\frac{3\zeta_1\zeta_{2,x_k}+3\zeta_{1,x_k}\zeta_2}{(1-\zeta_3)^2}$$
$$-\frac{\zeta_{3,x_k}}{(1-\zeta_3)^2}\left(\zeta_0-\frac{\zeta_2^3}{\zeta_3^2}\right)-\frac{6\zeta_2^2\zeta_{2,x_k}}{\zeta_3(1-\zeta_3)^3}+\frac{3\zeta_2^2\zeta_{2,x_k}}{\zeta_3^2(1-\zeta_3)^2}-\frac{2\zeta_2^3\zeta_{3,x_k}}{\zeta_3^3(1-\zeta_3)}-\frac{3\zeta_2^3\zeta_{3,x_k}}{\zeta_3^2(1-\zeta_3)^3}$$
$$\left.-\frac{6\zeta_1\zeta_2\zeta_{3,x_k}}{(1-\zeta_3)^3}-\frac{3\zeta_2^3\zeta_{3,x_k}(3\zeta_3-1)}{\zeta_3^2(1-\zeta_3)^4}+\frac{2\zeta_2^3\zeta_{3,x_k}(3\zeta_3-1)}{\zeta_3^3(1-\zeta_3)^3}\right]$$

The radial distribution, $\left(g_{ii}^{hs}\right)_{x_k}$ depends on four parameters $\left(\zeta_2,\zeta_3,\zeta_{2,\mathrm{x_k}},\zeta_{3,\mathrm{x_k}}\right)$, so using the chain rule:

$$\frac{\partial\left(\mathrm{g_{ii}^{hs}}\right)_{\mathrm{x_k}}}{\partial\mathrm{x_j}}|_{\mathrm{T,\rho,x_{s\neq j}}}=\sum_{\mathrm{n=2}}^{3}\frac{\partial\left(\mathrm{g_{ii}^{hs}}\right)_{\mathrm{x_k}}}{\partial\zeta_{\mathrm{n}}}\frac{\partial\zeta_{\mathrm{n}}}{\partial\mathrm{x_j}}|_{\mathrm{T,\rho,x_{s\neq j}}}+\sum_{n=2}^{3}\frac{\partial\left(g_{ii}^{hs}\right)_{x_k}}{\partial\zeta_{n,x_k}}\cancel{\frac{\partial\zeta_{n,x_k}}{\partial x_j}}|_{T,\rho,x_{s\neq j}}$$

$$\frac{\partial\left(g_{ii}^{hs}\right)_{x_k}}{\partial\zeta_2}=\left(\frac{d_i}{2}\right)^2\left(\frac{4\zeta_{2,x_k}}{(\eta-1)^3}-\frac{12\zeta_2\zeta_{3,x_k}}{(\eta-1)^4}\right)-\frac{3d_i\zeta_{3,x_k}}{(\eta-1)^3}$$

$$\frac{\partial\left(g_{ii}^{hs}\right)_{x_k}}{\partial\zeta_3}=\left(\frac{d_i}{2}\right)^2\left(\frac{12\zeta_2\zeta_{2,x_k}}{(\eta-1)^4}-\frac{24\zeta_2^2\zeta_{3,x_k}}{(\eta-1)^5}\right)-\frac{d_i}{2}\left(\frac{6\zeta_{2,x_k}}{(\eta-1)^3}-\frac{18\zeta_2\zeta_{3,x_k}}{(\eta-1)^4}\right)-\frac{2\zeta_{3,x_k}}{(\zeta_3-1)^3}$$

B.4.6.2 Dispersion Contribution

Regarding the derivative of the dispersion term $\left(\tilde{a}^{disp}\right)_{x_i}$, it depends on ρ, I_1, I_2, I_{1,x_i}, I_{2,x_i}, $\overline{m^2\epsilon\sigma^3}$, $\overline{m^2\epsilon^2\sigma^3}$, $\left(\overline{m^2\epsilon\sigma^3}\right)_{x_i}$, $\left(\overline{m^2\epsilon^2\sigma^3}\right)_{x_i}$, $\overline{m}$, C_1 and C_{1,x_i}, applying then the chain rule:

$$\frac{\partial\left(\tilde{a}^{disp}\right)_{x_k}}{\partial x_j}|_{T,\rho,x_{s\neq j}}$$
$$=\frac{\partial\left(\tilde{a}^{disp}\right)_{x_k}}{\partial I_1}\frac{\partial I_1}{\partial x_j}|_{T,\rho,x_{s\neq j}}+\frac{\partial\left(\tilde{a}^{disp}\right)_{x_k}}{\partial I_2}\frac{\partial I_2}{\partial x_j}|_{T,\rho,x_{s\neq j}}+\frac{\partial\left(\tilde{a}^{disp}\right)_{x_k}}{\partial I_{1,x_k}}\frac{\partial I_{1,x_k}}{\partial x_j}|_{T,\rho,x_{s\neq j}}$$
$$+\frac{\partial\left(\tilde{a}^{disp}\right)_{x_k}}{\partial I_{2,x_k}}\frac{\partial I_{2,x_k}}{\partial x_j}|_{T,\rho,x_{s\neq j}}+\frac{\partial\left(\tilde{a}^{disp}\right)_{x_k}}{\partial\overline{m^2\epsilon\sigma^3}}\frac{\partial\overline{m^2\epsilon\sigma^3}}{\partial x_j}|_{T,\rho,x_{s\neq j}}$$
$$+\frac{\partial\left(\tilde{a}^{disp}\right)_{x_k}}{\partial\overline{m^2\epsilon^2\sigma^3}}\frac{\partial\overline{m^2\epsilon^2\sigma^3}}{\partial x_j}|_{T,\rho,x_{s\neq j}}+\frac{\partial\left(\tilde{a}^{disp}\right)_{x_k}}{\partial\left(\overline{m^2\epsilon\sigma^3}\right)_{x_k}}\frac{\partial\left(\overline{m^2\epsilon\sigma^3}\right)_{x_k}}{\partial x_j}|_{T,\rho,x_{s\neq j}}$$
$$+\frac{\partial\left(\tilde{a}^{disp}\right)_{x_k}}{\partial\left(\overline{m^2\epsilon^2\sigma^3}\right)_{x_k}}\frac{\partial\left(\overline{m^2\epsilon^2\sigma^3}\right)_{x_k}}{\partial x_j}|_{T,\rho,x_{s\neq j}}+\frac{\partial\left(\tilde{a}^{disp}\right)_{x_k}}{\partial\overline{m}}\frac{\partial\overline{m}}{\partial x_j}|_{T,\rho,x_{s\neq j}}$$
$$+\frac{\partial\left(\tilde{a}^{disp}\right)_{x_k}}{\partial C_1}\frac{\partial C_1}{\partial x_j}|_{T,\rho,x_{s\neq j}}+\frac{\partial\left(\tilde{a}^{disp}\right)_{x_k}}{\partial C_{1,x_k}}\frac{\partial C_{1,x_k}}{\partial x_j}|_{T,\rho,x_{s\neq j}}$$

Where each derivative

$$\frac{\partial\left(\tilde{a}^{disp}\right)_{x_k}}{\partial I_1} = -2\pi\rho\left(\overline{m^2\epsilon\sigma^3}\right)_{x_k}$$

$$\frac{\partial\left(\tilde{a}^{disp}\right)_{x_k}}{\partial I_2} = -\pi\rho\overline{m^2\epsilon^2\sigma^3}\left(m_k C_1 + \overline{m}C_{1,x_k}\right) - \pi\rho\left(\overline{m^2\epsilon^2\sigma^3}\right)_{x_k}\overline{m}C_1$$

$$\frac{\partial\left(\tilde{a}^{disp}\right)_{x_k}}{\partial I_{1,x_k}} = -2\pi\rho\overline{m^2\epsilon\sigma^3}$$

$$\frac{\partial\left(\tilde{a}^{disp}\right)_{x_k}}{\partial I_{2,x_k}} = -\pi\rho\overline{m}C_1\overline{m^2\epsilon^2\sigma^3}$$

$$\frac{\partial\left(\tilde{a}^{disp}\right)_{x_k}}{\partial\overline{m^2\epsilon\sigma^3}} = -2\pi\rho I_{1,x_k}$$

$$\frac{\partial\left(\tilde{a}^{disp}\right)_{x_k}}{\partial\overline{m^2\epsilon^2\sigma^3}} = -\pi\rho\left(m_k C_1 I_2 + \overline{m}C_{1,x_k}I_2 + \overline{m}C_1 I_{2,x_k}\right)$$

$$\frac{\partial\left(\tilde{a}^{disp}\right)_{x_k}}{\partial\left(\overline{m^2\epsilon\sigma^3}\right)_{x_k}} = -2\pi\rho I_1$$

$$\frac{\partial\left(\tilde{a}^{disp}\right)_{x_k}}{\partial\left(\overline{m^2\epsilon^2\sigma^3}\right)_{x_k}} = -\pi\rho\overline{m}C_1 I_2$$

$$\frac{\partial\left(\tilde{a}^{disp}\right)_{x_k}}{\partial\overline{m}} = -\pi\rho\left(C_{1,x_k}I_2 + C_1 I_{2,x_k}\right)\overline{m^2\epsilon^2\sigma^3} - \pi\rho C_1 I_2\left(\overline{m^2\epsilon^2\sigma^3}\right)_{x_k}$$

$$\frac{\partial\left(\tilde{a}^{disp}\right)_{x_k}}{\partial C_1} = -\pi\rho\left(m_k I_2 + \overline{m}I_{2,x_k}\right)\overline{m^2\epsilon^2\sigma^3} - \pi\rho\overline{m}I_2\left(\overline{m^2\epsilon^2\sigma^3}\right)_{x_k}$$

$$\frac{\partial\left(\tilde{a}^{disp}\right)_{x_k}}{\partial C_{1,x_k}} = -\pi\rho\overline{m}I_2\overline{m^2\epsilon^2\sigma^3}$$

And the other derivatives are given by:

$$\frac{\partial \mathrm{I}_{1,\mathrm{x_k}}}{\partial \mathrm{x_j}}\mathrm{T},\rho,\mathrm{x_{s\neq j}} = \sum_{\mathrm{i}=0}^{6}\left[a_{i,x_j}i\zeta_{3,x_k}\eta^{i-1} + a_i i\cancel{\left(\frac{\partial\zeta_{3,x_k}}{\partial x_j}\right)_{T,\rho,x_{s\neq j}}}\eta^{i-1} + a_i i\zeta_{3,x_k}(i-1)\eta^{i-2}\zeta_{3,x_j} + \left(\frac{\partial a_{i,x_k}}{\partial x_j}\right)_{T,\rho,x_{s\neq j}}\eta^i + a_{i,x_k}i\eta^{i-1}\zeta_{3,x_j}\right]$$

Where

$$\left(\frac{\partial a_{i,x_k}}{\partial x_j}\right)_{T,\rho,x_{s\neq j}} = \frac{-2m_k m_j}{\overline{m}^3}a_{1i} - \frac{2m_k m_j}{\overline{m}^3}\left(3 - \frac{4}{\overline{m}}\right)a_{2i} + \frac{m_k}{\overline{m}^2}\left(\frac{4m_j}{\overline{m}^2}\right)a_{2i}$$

$$\frac{\partial I_{2,x_k}}{\partial x_j}|_{T,\rho,x_{s\neq j}} = \sum_{i=0}^{6}\left[b_{i,x_j} i\zeta_{3,x_k}\eta^{i-1} + b_i i\cancel{\left(\frac{\partial \zeta_{3,x_k}}{\partial x_j}\right)_{T,\rho,x_{s\neq j}}}\eta^{i-1} + b_i i\zeta_{3,x_k}(i-1)\eta^{i-2}\zeta_{3,x_j} + \left(\frac{\partial b_{i,x_k}}{\partial x_j}\right)_{T,\rho,x_{s\neq j}}\eta^i + b_{i,x_k} i\eta^{i-1}\zeta_{3,x_j}\right]$$

$$\left(\frac{\partial b_{i,x_k}}{\partial x_j}\right)_{T,\rho,x_{s\neq j}} = \frac{-2m_k m_j}{\overline{m}^3} b_{1i} - \frac{2m_k m_j}{\overline{m}^3}\left(3 - \frac{4}{\overline{m}}\right) b_{2i} + \frac{m_k}{\overline{m}^2}\left(\frac{4m_j}{\overline{m}^2}\right) b_{2i}$$

$$\frac{\partial\left(\overline{m^2\epsilon\sigma^3}\right)_{x_k}}{\partial x_j}|_{T,\rho,x_{s\neq j}} = 2m_k m_j\left(\frac{\epsilon_{kj}}{k_B T}\right)\sigma_{kj}^3$$

$$\frac{\partial\left(\overline{m^2\epsilon^2\sigma^3}\right)_{x_k}}{\partial x_j}|_{T,\rho,x_{s\neq j}} = 2m_k m_j\left(\frac{\epsilon_{kj}}{k_B T}\right)^2\sigma_{kj}^3$$

$$\begin{aligned}\left(\frac{\partial C_{1,x_k}}{\partial x_j}\right)_{T,\rho,x_{s\neq j}} &= \left(\frac{\partial C_2}{\partial x_j}\right)_{T,\rho,x_{s\neq j}}\zeta_{3,x_k} \\ &- 2C_1\left(\frac{\partial C_1}{\partial x_j}\right)_{T,\rho,x_{s\neq j}}\left[m_k\frac{8\eta-2\eta^2}{(1-\eta)^4} - m_k\frac{20\eta-27\eta^2+12\eta^3-2\eta^4}{(1-\eta)^2(2-\eta)^2}\right] \\ &- C_1^2 m_k\left[\frac{2(-2\eta^4+12\eta^3-27\eta^2+20\eta)}{(1-\eta)^2(\eta-2)^3} + \frac{4(8\eta-2\eta^2)}{(1-\eta)^5} - \frac{4\eta-8}{(1-\eta)^4}\right. \\ &\left. - \frac{2(-2\eta^4+12\eta^3-27\eta^2+20\eta)}{(1-\eta)^3(\eta-2)^2} + \frac{8\eta^3-36\eta^2+54\eta-20}{(1-\eta)^2(\eta-2)^2}\right]\zeta_{3,x_j}\end{aligned}$$

B.4.7 Cross derivative of Helmholtz free energy with respect to molar fraction and density

From the definition of compressibility factor, we have that

$$(\tilde{a}^{res})_{\rho,x_j} = \frac{Z_{x_j}}{\rho}$$

Where

$$\left.\frac{\partial Z}{\partial x_j}\right|_{T,\rho,x_{s\neq j}} = \left.\frac{\partial Z^{hc}}{\partial x_j}\right|_{T,\rho,x_{s\neq j}} + \left.\frac{\partial Z^{disp}}{\partial x_j}\right|_{T,\rho,x_{s\neq j}}$$

B.4.7.1 Chain contribution of the compressibility factor

$$\begin{aligned}\left.\frac{\partial Z^{hc}}{\partial x_j}\right|_{T,\rho,x_{s\neq j}} &= m_j Z^{hs} + \overline{m}\left.\frac{\partial Z^{hs}}{\partial x_j}\right|_{T,\rho,x_{s\neq j}} - (m_j-1)\left(g_{jj}^{hs}\right)^{-1}\rho\frac{\partial g_{jj}^{hs}}{\partial\rho} \\ &- \sum_i x_i(m_i-1)\left[\frac{\frac{\partial}{\partial x_j}\left(\rho\frac{\partial g_{ii}^{hs}}{\partial\rho}\right)}{g_{ii}^{hs}} - \frac{\frac{\partial g_{ii}^{hs}}{\partial x_j}\rho\frac{\partial g_{ii}^{hs}}{\partial\rho}}{\left(g_{ii}^{hs}\right)^2}\right]\end{aligned}$$

Regarding the Hard-Sphere contribution of the compressibility factor,

$$\left.\frac{\partial Z^{hs}}{\partial x_j}\right|_{T,\rho,x_{s\neq j}} = \sum_{n=0}^{3} \frac{\partial Z^{hs}}{\partial \zeta_n} \frac{\partial \zeta_n}{\partial x_j}_{T,\rho,x_{s\neq j}}$$

Where

$$\frac{\partial Z^{hs}}{\partial \zeta_0} = \frac{-3\zeta_1\zeta_2}{\zeta_0^2(1-\zeta_3)^2} + \frac{\zeta_3\zeta_2^3 - 3\zeta_2^3}{\zeta_0^2(1-\zeta_3)^3}$$

$$\frac{\partial Z^{hs}}{\partial \zeta_1} = \frac{3\zeta_2}{\zeta_0(1-\zeta_3)^2}$$

$$\frac{\partial Z^{hs}}{\partial \zeta_2} = \frac{3\zeta_1}{\zeta_0(1-\zeta_3)^2} + \frac{3\zeta_2^2(3-\zeta_3)}{\zeta_0(1-\zeta_3)^3}$$

$$\frac{\partial Z^{hs}}{\partial \zeta_3} = \frac{1}{(1-\zeta_3)^2} + \frac{6\zeta_1\zeta_2}{\zeta_0(1-\zeta_3)^3} + \frac{\zeta_2^3(8-2\zeta_3)}{\zeta_0(1-\zeta_3)^4}$$

Regarding the derivatives of the radial distribution g_{ii}^{hs}, the term $\left(\rho\frac{\partial g_{ii}^{hs}}{\partial \rho}\right)_{T,\rho,x_{s\neq j}}$ depends on the abbreviations ζ_n therefore applying again the chain rule:

$$\frac{\partial}{\partial x_j}\left(\rho\frac{\partial g_{ii}^{hs}}{\partial \rho}\right)_{T,\rho,x_{s\neq j}} = \sum_{n=0}^{3} \quad \frac{\partial}{\partial \zeta_n}\left(\rho\frac{\partial g_{ii}^{hs}}{\partial \rho}\right)\cdot\frac{\partial \zeta_n}{\partial x_j}_{T,\rho,x_{s\neq j}}$$

where the first term is given by

$$\frac{\partial}{\partial \zeta_0}\left(\rho\frac{\partial g_{ii}^{hs}}{\partial \rho}\right) = \frac{\partial}{\partial \zeta_1}\left(\rho\frac{\partial g_{ii}^{hs}}{\partial \rho}\right) = 0$$

$$\frac{\partial}{\partial \zeta_2}\left(\rho\frac{\partial g_{ii}^{hs}}{\partial \rho}\right) = \frac{d_i}{2}\left(\frac{3}{(1-\zeta_3)^2} + \frac{6\zeta_3}{(1-\zeta_3)^3}\right) + \frac{d_i^2\zeta_3}{2}\left(\frac{4}{(1-\zeta_3)^3} + \frac{6\zeta_3}{(1-\zeta_3)^4}\right)$$

$$\frac{\partial}{\partial \zeta_3}\left(\rho\frac{\partial g_{ii}^{hs}}{\partial \rho}\right) = \frac{-1}{(1-\zeta_3)^2} - \frac{3d_i\zeta_2 - 2}{(1-\zeta_3)^3} - \frac{3d_i\zeta_2(d_i\zeta_2 - 6)}{2(1-\zeta_3)^4} + \frac{6d_i^2\zeta_2^2}{(1-\zeta_3)^5}$$

B.4.7.2 Dispersion contribution of the compressibility factor

$$\begin{aligned}\frac{\partial Z^{disp}}{\partial x_j} = &-2\pi\rho\overline{m^2\epsilon\sigma^3}\frac{\partial}{\partial x_j}\left(\frac{\partial(\eta I_1)}{\partial \eta}\right) - 2\pi\rho\frac{\partial(\eta I_1)}{\partial \eta}\frac{\partial\overline{m^2\epsilon\sigma^3}}{\partial x_j} - \pi\rho\frac{\partial\overline{m}}{\partial x_j}\left[C_1\frac{\partial(\eta I_2)}{\partial \eta} + C_2\eta I_2\right]\overline{m^2\epsilon^2\sigma^3} \\ &- \pi\rho\overline{m}\left[\frac{\partial(\eta I_2)}{\partial \eta}\frac{\partial C_1}{\partial x_j} + C_1\frac{\partial}{\partial x_j}\left(\frac{\partial(\eta I_2)}{\partial \eta}\right)\right]\overline{m^2\epsilon^2\sigma^3} \\ &- \pi\rho\overline{m}\left[\frac{\partial C_2}{\partial x_j}\eta I_2 + C_2\eta\frac{\partial I_2}{\partial x_j}\right]\overline{m^2\epsilon^2\sigma^3} - \pi\rho\overline{m}\left[C_1\frac{\partial(\eta I_2)}{\partial \eta} + C_2\eta I_2\backslash bigg\right]\frac{\partial\overline{m^2\epsilon^2\sigma^3}}{\partial x_j}\end{aligned}$$

All the unknowns in the previous equation are given below:

$$\frac{\partial C_2}{\partial x_j}|_{T,\rho,x_{s\neq j}} = \frac{\partial}{\partial x_j}\left(\frac{\partial C_1}{\partial \eta}\right)_{T,\rho,x_{s\neq j}} = \frac{\partial^2 C_1}{\partial \eta^2}\left(\frac{\partial \eta}{\partial x_j}\right)_{T,\rho,x_{s\neq j}} + m_j\frac{\partial^2 C_1}{\partial \eta\,\partial\overline{m}}$$

$$\frac{\partial}{\partial x_j}\left(\frac{\partial(\eta I_1)}{\partial \eta}\right)|_{T,\rho,x_{s\neq j}} = \sum_{i=0}^{6}\left[\frac{\partial a_i}{\partial x_j}|_{T,\rho,x_{s\neq j}}(i+1)\eta^i + a_i(\overline{m})(i+1)i\eta^{i-1}\frac{\partial \zeta_3}{\partial x_j}|_{T,\rho,x_{s\neq j}}\right]$$

$$\frac{\partial}{\partial x_j}\left(\frac{\partial(\eta I_2)}{\partial \eta}\right)|_{T,\rho,x_{s\neq j}} = \sum_{i=0}^{6}\left[\frac{\partial b_i}{\partial x_j}|_{T,\rho,x_{s\neq j}}(i+1)\eta^i + b_i(\overline{m})(i+1)i\eta^{i-1}\frac{\partial \zeta_3}{\partial x_j}|_{T,\rho,x_{s\neq j}}\right]$$

Lastly

$$\frac{\partial C_1}{\partial \overline{m}} = -C_1^2\left[\frac{8\eta - 2\eta^2}{(1-\eta)^4} + \frac{20\eta - 27\eta^2 + 12\eta^3 - 2\eta^4}{[(1-\eta)(2-\eta)]^2}\right]$$

$$\frac{\partial^2 C_1}{\partial \eta\, \partial \overline{m}} = 2\frac{C_2}{C_1}\frac{\partial C_1}{\partial \overline{m}} - C_1^2\left[\frac{-4\eta^2 + 20\eta + 8}{(1-\eta)^5} - \frac{2\eta^3 + 12\eta^2 - 48\eta + 40}{(1-\eta)^3(2-\eta)^3}\right]$$

Appendix C

C.1 PC-SAFT parameters for thermodynamic and thermophysical properties

PC-SAFT parameters

	m (-)	σ (Å)	ε/k_B (K)
n-octadecane	7.438	3.948	254.90
n-hexadecane	6.669	3.944	253.59
heptamethylnonane	5.603	4.164	266.46
1-methylnaphthalene	3.422	3.901	337.14
1,2,3,4-tetrahydronaphthalene	3.088	3.996	337.46
trans-decalin	3.291	4.067	307.98
n-butylcyclohexane	3.682	4.036	282.41
1,2,4-trimethylbenzene	3.610	3.749	284.25

Ideal gas coefficients

	A	B	C	D	ΔH_{ref} [kJ/kg]
n-octadecane	-13.474	1.71384	$-9.554*10^{-4}$	$2.03*10^{-7}$	-414.83
n-hexadecane	-11.656	1.52384	$-8.466*10^{-4}$	$1.792*10^{-7}$	-373.59
heptamethylnonane	-86.757	1.90728	$-1.3652*10^{-3}$	$3.944*10^{-7}$	-405.10
1-methylnaphthalene	-58.16	0.90672	$-6.7548*10^{-4}$	$2.014*10^{-7}$	116.94
1,2,3,4-tetrahydronaphthalene	-87.11	0.9832	$-7.1356*10^{-4}$	$2.06*10^{-7}$	27.63
trans-decalin	-127.17	1.2172	$-7.75*10^{-4}$	$1.868*10^{-7}$	-182.42
n-butylcyclohexane	-71.807	1.07592	$-6.012*10^{-4}$	$1.174*10^{-7}$	-213.32
1,2,4-trimethylbenzene	-10.6	0.66096	$-3.6292*10^{-4}$	$7.16*10^{-8}$	-13.94

Entropy scaling parameters for viscosity

	A^{μ}	B^{μ}	C^{μ}	D^{μ}
n-octadecane	-0.94240	-4.2086	-0.92723	-0.2241
n-hexadecane	-0.89303	-3.9704	-0.84192	-0.1992
heptamethylnonane	-0.57516	-3.2643	-0.75823	-0.1992
1-methylnaphthalene	-0.59115	-2.7895	-0.58370	-0.1370
1,2,3,4-tetrahydronaphthalene	-0.50055	-2.6232	-0.44389	-0.1245
trans-decalin	-0.29640	-2.5604	-0.24863	-0.1245
n-butylcyclohexane	-0.58564	-2.8879	-0.41966	-0.1245
1,2,4-trimethylbenzene	-0.72078	-2.6213	-0.56599	-0.1121

Entropy scaling parameters for thermal conductivity

	A^{λ}	B^{λ}	C^{λ}	D^{λ}
n-octadecane	0	-0.40156	1.98005	0
n-hexadecane	0.36701	-0.52738	1.15300	0
heptamethylnonane	0.36701	-0.52738	1.15300	0
1-methylnaphthalene	0.51308	-0.57468	0.67839	-0.06761
1,2,3,4-tetrahydronaphthalene	0.51308	-0.57468	0.67839	-0.06761
trans-decalin	0.51308	-0.57468	0.67839	-0.06761
n-butylcyclohexane	0.51308	-0.57468	0.67839	-0.06761
1,2,4-trimethylbenzene	0	-0.45935	1.44014	0

Publications

- **Journal publications (newest fist)**
  1. Koukouvinis, P., **Vidal-Roncero, A.**, Rodriguez, C., Gavaises, M. and Pickett, L., 'High pressure/high temperature multiphase simulations of dodecane injection to nitrogen: Application on ECN Spray-A'. Fuel, 275, p.117871, 2020. https://doi.org/10.1016/j.fuel.2020.117871
  2. **Vidal, A.,** Koukouvinis, P., and Gavaises, M. 'Vapor-liquid equilibrium calculations at specified composition, density and temperature with the perturbed chain statistical associating fluid theory (PC-SAFT) equation of state. Fluid Phase Equilibria', 112661, 2020. https://doi.org/10.1016/j.fluid.2020.112661
  3. Rodriguez, C., **Vidal, A.**, Koukouvinis, P., Gavaises, M., and McHugh, M. A. 'Simulation of transcritical fluid jets using the PC-SAFT EoS', Journal of Computational Physics, 374, 444–468, 2018. https://doi.org/10.1016/j.jcp.2018.07.030
  4. **Vidal, A.,** Rodriguez, C., Koukouvinis, P., Gavaises, M., and McHugh, M. A. 'Modelling of Diesel fuel properties through its surrogates using Perturbed-Chain, Statistical Associating Fluid Theory', International Journal Engine Research, 2018 https://doi.org/10.1177/1468087418801712

- **Pending publication**
  5. **Vidal, A.**, Kolovos, K., Gold, M. Pearson, R., Koukouvinis, P. and Gavaises, M. 'Preferential cavitation and friction-induced heating of multi-component Diesel fuel surrogates up to 450MPa', submitted to *International Journal of Heat and Mass Transfer, May 2020*
  6. Konstantinos Kolovos, Nikolaos Kyriazis, Phoevos Koukouvinis, **Alvaro Vidal** 'Large-eddy simulation of friction heating and turbulent cavitating flow in a Diesel injector including needle movement', to be submitted to international Journal Engine Research, September 2020

- **Conference publications (newest fist)**
  1. Koukouvinis, P., **Vidal-Roncero, A.**, Rodriguez, C., Gavaises, M. and Pickett, L. 'Enhancing the predictive capabilities for high P/T fuel sprays; non-ideal thermodynamic modelling using PC-SAFT', ERCOFTAC Non-Ideal CFD (NICFD)*, 2020*
  2. **Vidal Roncero, A.,** Koukouvinis, F. and Gavaises, M. 'On the effect of realistic multicomponent diesel surrogates on cavitation and in-nozzle flow', IMechE Conference on Fuel Injection Systems: engines, 4-5 Dec 2018, London, UK.
  3. **Vidal Roncero, A**., Rodriguez, C., Koukouvinis, P., and Gavaises, M. 'Effect of realistic multicomponent diesel surrogates on predicted in-nozzle flow and cavitation', ICLASS 2018, 22-26 Jul 2018, Chicago, USA.
  4. Rodriguez, C., **Vidal, A.**, Koukouvinis, P., and Gavaises, M. 'Supercritical and transcritical real-fluid mixing using the PC-SAFT EOS' 28th European conference on Liquid Atomization and Spray Systems', ILASS Europe. Editorial Universitat Politècnica de València. 7-9 Sept 2017. https://doi.org/10.4995/ILASS2017.2017.5000

References

1. Mueller, C. J.; Cannella, W. J.; Bays, J. T.; Bruno, T. J.; DeFabio, K.; Dettman, H. D.; Gieleciak, R. M.; Huber, M. L.; Kweon, C.-B.; McConnell, S. S.; Pitz, W. J.; Ratcliff, M. A., Diesel Surrogate Fuels for Engine Testing and Chemical-Kinetic Modeling: Compositions and Properties. *Energy & Fuels* **2016,** *30*, 1445-1461.
2. Lemmon, E. W.; Huber, M. L.; McLinden, M. O., NIST Standard Reference Database 23: Reference Fluid Thermodynamic and Transport Properties-REFPROP. 9.0. *NIST* **2010**.
3. Schaschke, C.; Fletcher, I.; Glen, N., Density and Viscosity Measurement of Diesel Fuels at Combined High Pressure and Elevated Temperature. *Processes* **2013,** *1* (2), 30-48.
4. Schaschke, C.; Fletcher, I.; Glen, N., Density and viscosity measurement of diesel fuels at combined high pressure and elevated temperature. *Processes* **2013,** *1*, 30–48.
5. Mueller, C. J.; Cannella, W. J.; Bays, J. T.; Bruno, T. J.; DeFabio, K.; Dettman, H. D.; Gieleciak, R. M.; Huber, M. L.; Kweon, C.-B.; McConnell, S. S., Diesel surrogate fuels for engine testing and chemical-kinetic modeling: Compositions and properties. *Energy & Fuels* **2016,** *30*, 1445–1461.
6. Wu, X.; Li, C.; Jia, W., An improved viscosity model based on Peng-Robinson equation of state for light hydrocarbon liquids and gases. *Fluid Phase Equilibria* **2014,** *380*, 147-151.
7. Liang, X.; Yan, W.; Thomsen, K.; Kontogeorgis, G. M., On petroleum fluid characterization with the PC-SAFT equation of state. *Fluid Phase Equilibria* **2014,** *375*, 254-268.
8. Cox, K. R.; Chapman, W. G., The Properties of Gases and Liquids, 5th Edition By Bruce E. Poling (University of Toledo), John M. Prausnitz (University of California at Berkeley), and John P. O'Connell (University of Virginia). McGraw-Hill: New York. 2001. 768 pp. $115.00. ISBN 0-07. *Journal of the American Chemical Society* **2001,** *123* (27), 6745-6745.
9. UNEP *The Emissions Gap Report. United Nations Environment Programme, Nairobi, page XIV and XV*; 2018.
10. ExxonMobil *OUTLOOK FOR ENERGY: A PERSPECTIVE TO 2040*; 2019.
11. Lemaire, R.; Faccinetto, A.; Therssen, E.; Ziskind, M.; Focsa, C.; Desgroux, P., Experimental comparison of soot formation in turbulent flames of Diesel and surrogate Diesel fuels. *Proceedings of the Combustion Institute* **2009,** *32*, 737-744.
12. Ribeiro, N. M.; Pinto, A. C.; Quintella, C. M.; Rocha, G. O.; Teixeira, L. S. G.; Guarieiro, L. l. L. N.; Carmo Rangel, M.; Veloso, M. C. C.; Rezende, M. J. C.; Cruz, R. S.; Oliveira, A. M.; Torres, E. A.; Andrade, J. B., The Role of Additives for Diesel and Diesel Blended (Ethanol or Biodiesel) Fuels: A Review. *Energy & Fuels* **2007,** *21*, 2433-2445.
13. Han, Z.; Uludogan, A.; Hampson, G. J.; Reitz, R. D. In *Mechanism of Soot and NOx Emission Reduction Using Multiple-injection in a Diesel Engine*, SAE Technical Paper Series, SAE International: 1996.
14. Pickett, L. M.; Siebers, D. L., Soot in diesel fuel jets: effects of ambient temperature, ambient density, and injection pressure. *Combustion and Flame* **2004,** *138*, 114-135.
15. Gavaises, M., Flow in valve covered orifice nozzles with cylindrical and tapered holes and link to cavitation erosion and engine exhaust emissions. *International Journal of Engine Research* **2008,** *9*, 435-447.
16. Payri, R.; Salvador, F. J.; García, A.; Gil, A., Combination of visualization techniques for the analysis of evaporating diesel sprays. *Energy and Fuels* **2012,** *26* (9), 5481-5490.
17. Schmidt, D. P.; Corradini, M. L., The internal flow of diesel fuel injector nozzles: A review. *International Journal of Engine Research* **2001,** *2*, 1-22.

18. Manin, J.; Bardi, M.; Pickett, L. M.; Payri, R., Boundary condition and fuel composition effects on injection processes of high-pressure sprays at the microscopic level. *International Journal of Multiphase Flow* **2016,** *83*, 267-278.
19. Yuan, W.; Schnerr, G. H., Numerical Simulation of Two-Phase Flow in Injection Nozzles: Interaction of Cavitation and External Jet Formation. *Journal of Fluids Engineering* **2003,** *125*, 963.
20. Sou, A.; Hosokawa, S.; Tomiyama, A., Effects of cavitation in a nozzle on liquid jet atomization. *International Journal of Heat and Mass Transfer* **2007,** *50*, 3575-3582.
21. Faeth, G. M.; Hsiang, L.-P.; Wu, P.-K., Structure and breakup properties of sprays. *International Journal of Multiphase Flow* **1995,** *21*, 99-127.
22. Suh, H. K.; Lee, C. S., Effect of cavitation in nozzle orifice on the diesel fuel atomization characteristics. *International Journal of Heat and Fluid Flow* **2008,** *29*, 1001-1009.
23. Payri, R.; Molina, S.; Salvador, F. J.; Gimeno, J., A study of the relation between nozzle geometry, internal flow and sprays characteristics in diesel fuel injection systems. *KSME International Journal* **2004,** *18*, 1222-1235.
24. Payri, R.; Salvador, F. J.; Gimeno, J.; Zapata, L. D., Diesel nozzle geometry influence on spray liquid-phase fuel penetration in evaporative conditions. *Fuel* **2008,** *87* (7), 1165-1176.
25. Tat, M. E.; Van Gerpen, J. H.; Soylu, S.; Canakci, M.; Monyem, A.; Wormley, S., The speed of sound and isentropic bulk modulus of biodiesel at 21°C from atmospheric pressure to 35 MPa. *Journal of the American Oil Chemists' Society* **2000,** *77* (3), 285-289.
26. Hoekman, S. K.; Robbins, C., Review of the effects of biodiesel on NOx emissions. *Fuel Processing Technology* **2012,** *96*, 237-249.
27. Lapuerta, M. n.; Armas, O.; Rodr??guez-Fern??ndez, J., Effect of biodiesel fuels on diesel engine emissions. *Progress in Energy and Combustion Science* **2008,** *34* (2), 198-223.
28. Wei, M.; Li, S.; Xiao, H.; Guo, G., Combustion performance and pollutant emissions analysis using diesel/gasoline/iso-butanol blends in a diesel engine. *Energy Conversion and Management* **2017,** *149*, 381-391.
29. Lemaire, R.; Faccinetto, A.; Therssen, E.; Ziskind, M.; Focsa, C.; Desgroux, P., Experimental comparison of soot formation in turbulent flames of Diesel and surrogate Diesel fuels. *Proceedings of the Combustion Institute* **2009,** *32 I* (1), 737-744.
30. Luning Prak, D. J.; Alexandre, S. M.; Cowart, J. S.; Trulove, P. C., Density, viscosity, speed of sound, bulk modulus, surface tension, and flash point of binary mixtures of n -dodecane with 2,2,4,6,6-pentamethylheptane or 2,2,4,4,6,8,8-heptamethylnonane. *Journal of Chemical and Engineering Data* **2014,** *59* (4), 1334-1346.
31. Nayyar, A.; Sharma, D.; Soni, S. L.; Mathur, A., Characterization of n-butanol diesel blends on a small size variable compression ratio diesel engine: Modeling and experimental investigation. *Energy Conversion and Management* **2017,** *150*, 242-258.
32. Nabi, M. N.; Zare, A.; Hossain, F. M.; Bodisco, T. A.; Ristovski, Z. D.; Brown, R. J., A parametric study on engine performance and emissions with neat diesel and diesel-butanol blends in the 13-Mode European Stationary Cycle. *Energy conversion and management* **2017,** *148*, 251-259.
33. Mueller, C. J.; Cannella, W. J.; Bruno, T. J.; Bunting, B.; Dettman, H. D.; Franz, J. A.; Huber, M. L.; Natarajan, M.; Pitz, W. J.; Ratcliff, M. A.; Wright, K., Methodology for formulating diesel surrogate fuels with accurate compositional, ignition-quality, and volatility characteristics. *Energy and Fuels* **2012,** *26* (6), 3284-3303.
34. Prak, D. J. L.; Morris, R. E.; Cowart, J. S.; Hamilton, L. J.; Trulove, P. C., Density, viscosity, speed of sound, bulk modulus, surface tension, and flash point of direct sugar to hydrocarbon diesel (DSH-76) and binary mixtures of N -hexadecane and 2,2,4,6,6-pentamethylheptane. *Journal of Chemical and Engineering Data* **2013,** *58* (12), 3536-3544.
35. Srivastava, S. P.; Hancs??k, J., Fuels and Fuel-Additives. *Fuels and Fuel-Additives* **2014**, 1-364.
36. Lemmon, E. W.; Huber, M. L., Thermodynamic properties of n-dodecane. *Energy and Fuels* **2004,** *18* (4), 960-967.

37. Gieleciak, R. *Gc×Gc Studies of Palette Compounds Used in the Next Generation of Diesel Fuel Surrogate Blends*; 2016.
38. Theodorakakos, A.; Strotos, G.; Mitroglou, N.; Atkin, C.; Gavaises, M., Friction-induced heating in nozzle hole micro-channels under extreme fuel pressurisation. *Fuel* **2014,** *123* (x), 143-150.
39. Strotos, G.; Koukouvinis, P.; Theodorakakos, A.; Gavaises, M.; Bergeles, G., Transient heating effects in high pressure Diesel injector nozzles. *International Journal of Heat and Fluid Flow* **2015,** *51*, 257-267.
40. Strotos, G.; Malgarinos, I.; Nikolopoulos, N.; Gavaises, M., Predicting the evaporation rate of stationary droplets with the VOF methodology for a wide range of ambient temperature conditions. *International Journal of Thermal Sciences* **2016,** *109*, 253-262.
41. Mithun, M.-G.; Koukouvinis, P.; Gavaises, M., Numerical simulation of cavitation and atomization using a fully compressible three-phase model. *Physical Review Fluids* **2018,** *3* (6), 064304.
42. Kolev, N. I., Multiphase Flow Dynamics 4 - Turbulence, gas absorption and release, diesel fuel properties. **2010**.
43. Lemmon, E. W.; Huber, M. L.; McLinden, M. O., NIST reference fluid thermodynamic and transport properties–REFPROP. Version: 2002.
44. Sudiro, M.; Bertucco, A., Production of synthetic gasoline and diesel fuel by alternative processes using natural gas and coal: Process simulation and optimization. *Energy* **2009,** *34* (12), 2206-2214.
45. Huber, M., NIST thermophysical properties of hydrocarbon mixtures database (SUPERTRAPP). *NIST Standard Reference Database* **2003,** *4*.
46. Lin, R.; Tavlarides, L. L., Thermophysical properties needed for the development of the supercritical diesel combustion technology: Evaluation of diesel fuel surrogate models. *The Journal of Supercritical Fluids* **2012,** *71*, 136-146.
47. Stamataki, S.; Tassios, D., Performance of cubic EoS at high pressures. *Oil & Gas Science and Technology* **1998,** *53*, 367-377.
48. Pedersen, K. S.; Milter, J.; Sørensen, H., Cubic Equations of State Applied to HT/HP and Highly Aromatic Fluids. *SPE Journal* **2004,** *9* (October 2003), 186-192.
49. Gross, J.; Sadowski, G., Perturbed-chain SAFT: An equation of state based on a perturbation theory for chain molecules. *Industrial & engineering chemistry research* **2001,** *40*, 1244-1260.
50. Kontogeorgis, G. M.; Folas, G. K., *Thermodynamic models for industrial applications: from classical and advanced mixing rules to association theories. Appendix A*. John Wiley & Sons: 2009.
51. Tihic, A.; Kontogeorgis, G. M.; von Solms, N.; Michelsen, M. L.; Constantinou, L., A Predictive Group-Contribution Simplified PC-SAFT Equation of State: Application to Polymer Systems. *Industrial & Engineering Chemistry Research* **2008,** *47* (15), 5092-5101.
52. de Villiers, A. J.; Schwarz, C. E.; Burger, A. J.; Kontogeorgis, G. M., Evaluation of the PC-SAFT, SAFT and CPA equations of state in predicting derivative properties of selected non-polar and hydrogen-bonding compounds. *Fluid Phase Equilibria* **2013,** *338*, 1-15.
53. Leekumjorn, S.; Krejbjerg, K., Phase behavior of reservoir fluids: Comparisons of PC-SAFT and cubic EOS simulations. *Fluid Phase Equilibria* **2013,** *359*, 17–23.
54. Peng, D.-Y.; Robinson, D. B., A new two-constant equation of state. *Industrial & Engineering Chemistry Fundamentals* **1976,** *15*, 59-64.
55. Soave, G., Equilibrium constants from a modified Redlich-Kwong equation of state. *Chemical Engineering Science* **1972,** *27*, 1197-1203.
56. Yan, W.; Varzandeh, F.; Stenby, E. H., PVT modeling of reservoir fluids using PC-SAFT EoS and Soave-BWR EoS. *Fluid Phase Equilibria* **2015,** *386*, 96-124.
57. Burgess, W. A.; Tapriyal, D.; Morreale, B. D.; Soong, Y.; Baled, H. O.; Enick, R. M.; Wu, Y.; Bamgbade, B. A.; McHugh, M. A., Volume-translated cubic EoS and PC-SAFT density models and a

free volume-based viscosity model for hydrocarbons at extreme temperature and pressure conditions. *Fluid Phase Equilibria* **2013,** *359*, 38–44.
58. Schou Pedersen, K.; Hasdbjerg, C. In *PC-SAFT equation of state applied to petroleum reservoir fluids*, SPE Annual Technical Conference and Exhibition, 2007.
59. Gord, M. F.; Roozbahani, M.; Rahbari, H. R.; Hosseini, S. J. H., Modeling thermodynamic properties of natural gas mixtures using perturbed-chain statistical associating fluid theory. *Russian Journal of Applied Chemistry* **2013,** *86*, 867–878.
60. Panuganti, S. R.; Vargas, F. M.; Gonzalez, D. L.; Kurup, A. S.; Chapman, W. G., PC-SAFT characterization of crude oils and modeling of asphaltene phase behavior. *Fuel* **2012,** *93*, 658–669.
61. Zúñiga-Hinojosa, M. A.; Justo-García, D. N.; Aquino-Olivos, M. A.; Román-Ramírez, L. A.; García-Sánchez, F., Modeling of asphaltene precipitation from n-alkane diluted heavy oils and bitumens using the PC-SAFT equation of state. *Fluid Phase Equilibria* **2014,** *376*, 210–224.
62. Arya, A.; Liang, X.; Von Solms, N.; Kontogeorgis, G. M., Modeling of Asphaltene Onset Precipitation Conditions with Cubic Plus Association (CPA) and Perturbed Chain Statistical Associating Fluid Theory (PC-SAFT) Equation of States.
63. Nascimento, F. P.; Costa, G. M. N.; Melo, S. A. B. V., A comparative study of CPA and PC-SAFT equations of state to calculate the asphaltene onset pressure and phase envelope. *Fluid Phase Equilibria* **2019,** *494*, 74-92.
64. Zhao, Y.; Dong, X.; Zhong, Q.; Zhang, H.; Li, H.; Shen, J.; Gong, M., Modeling Vapor Liquid Phase Equilibrium for CxHy CxHyFz Using Peng–Robinson and Perturbed-Chain SAFT. *Industrial & Engineering Chemistry Research* **2017,** *56*, 7384-7389.
65. Carneiro, A. P.; Held, C.; Rodríguez, O.; Sadowski, G.; Macedo, E. A., Solubility of Sugars and Sugar Alcohols in Ionic Liquids: Measurement and PC-SAFT Modeling. *The Journal of Physical Chemistry B* **2013,** *117*, 9980-9995.
66. Abolala, M.; Peyvandi, K.; Varaminian, F.; Hashemianzadeh, S. M., A comprehensive description of single-phase and VLE properties of cryogenic fluids using molecular-based equations of state. *Fluid Phase Equilibria* **2019,** *494*, 143-160.
67. Diamantonis, N. I.; Boulougouris, G. C.; Mansoor, E.; Tsangaris, D. M.; Economou, I. G., Evaluation of Cubic, SAFT, and PC-SAFT Equations of State for the Vapor–Liquid Equilibrium Modeling of CO2 Mixtures with Other Gases. *Industrial & Engineering Chemistry Research* **2013,** *52*, 3933-3942.
68. Rodriguez, C.; Koukouvinis, P.; Gavaises, M., Simulation of supercritical diesel jets using the PC-SAFT EoS. *The Journal of Supercritical Fluids* **2019,** *145*, 48-65.
69. Vidal, A.; Koukouvinis, P.; Gavaises, M. In *On the effect of realistic multicomponent diesel surrogates on cavitation and in-nozzle flow*, IMechE, 2018.
70. Polívka, O.; Mikyška, J., Compositional modeling in porous media using constant volume flash and flux computation without the need for phase identification. *Journal of Computational Physics* **2014**, 149-169.
71. Jindrová, T., *Computational methods in thermodynamics of multicomponent mixtures.* Master degree thesis, Czech Technical University in Prague: 2013.
72. Michelsen, M. L., The isothermal flash problem. Part I. Stability. *Fluid Phase Equilibria* **1982,** *9*, 1-19.
73. Nichita, D. V.; de-Hemptinne, J.-C.; Gomez, S., Isochoric Phase Stability Testing for Hydrocarbon Mixtures. *Petroleum Science and Technology* **2009,** *27*, 2177-2191.
74. Levy, A. V.; Gómez, S., The tunneling method applied to global optimization. *Numerical optimization* **1985,** *1981*, 213-244.
75. Mikyška, J.; Firoozabadi, A., A new thermodynamic function for phase-splitting at constant temperature, moles, and volume. *AIChE Journal* **2010,** *57*, 1897-1904.
76. Jindrová, T.; Mikyška, J., General algorithm for multiphase equilibria calculation at given volume, temperature, and moles. *Fluid Phase Equilibria* **2015,** *393*, 7-25.

77. Nichita, D. V., New unconstrained minimization methods for robust flash calculations at temperature, volume and moles specifications. *Fluid Phase Equilibria* **2018,** *466*, 31-47.
78. Paterson, D.; Michelsen, M. L.; Yan, W.; Stenby, E. H., Extension of modified RAND to multiphase flash specifications based on state functions other than (T,P). *Fluid Phase Equilibria* **2018,** *458*, 288-299.
79. Tang, X.; Gross, J., Renormalization-group corrections to the perturbed-chain statistical associating fluid theory for binary mixtures. *Industrial and Engineering Chemistry Research* **2010**, 9436-9444.
80. Bymaster, A.; Emborsky, C.; Dominik, A.; Chapman, W. G., Renormalization-group corrections to a perturbed-chain statistical associating fluid theory for pure fluids near to and far from the critical region. *Industrial and Engineering Chemistry Research* **2008**, 6264-6274.
81. García-Sánchez, F.; Schwartzentruber, J.; Ammar, M. N.; Renon, H., Modeling of multiphase liquid equilibria for multicomponent mixtures. *Fluid phase equilibria* **1996,** *121*, 207-225.
82. Schnabel, R. B.; Eskow, E., A Revised Modified Cholesky Factorization Algorithm. *SIAM Journal on Optimization* **1999,** *9*, 1135-1148.
83. Jindrová, T.; Mikyška, J., Fast and robust algorithm for calculation of two-phase equilibria at given volume, temperature, and moles. *Fluid Phase Equilibria* **2013,** *353*, 101-114.
84. von Solms, N.; Michelsen, M. L.; Kontogeorgis, G. M., Computational and Physical Performance of a Modified PC-SAFT Equation of State for Highly Asymmetric and Associating Mixtures. *Industrial & Engineering Chemistry Research* **2003**, 1098-1105.
85. Reid, B.; Gavaises, M.; Mitroglou, N.; Hargrave, G.; Garner, C.; Long, E.; McDavid, R., On the formation of string cavitation inside fuel injectors. *Experiments in fluids* **2014,** *55* (1), 1662.
86. Vera-Tudela, W.; Haefeli, R.; Barro, C.; Schneider, B.; Boulouchos, K., An experimental study of a very high-pressure diesel injector (up to 5000 bar) by means of optical diagnostics. *Fuel* **2020,** *275*, 117933.
87. Yuan, W., Modeling and computation of unsteady cavitation flows in injection nozzles. *MÃcanique & Industries* **2001,** *2*, 383-394.
88. Battistoni, M.; Som, S.; Longman, D. E., Comparison of Mixture and Multifluid Models for In-Nozzle Cavitation Prediction. *Journal of Engineering for Gas Turbines and Power* **2014,** *136*, 061506.
89. Habchi, C.; Dumont, N.; Simonin, O., Multidimentional Simulation of Cavitating Flows in Diesel Injectors by a Homogeneous Mixture Modeling Approach. *Atomization and Sprays* **2008,** *18*, 129-162.
90. Lindau, J. W.; Kunz, R. F.; Boger, D. A.; Stinebring, D. R.; Gibeling, H. J., High Reynolds Number, Unsteady, Multiphase CFD Modeling of Cavitating Flows. *Journal of Fluids Engineering* **2002,** *124*, 607.
91. Singhal, A. K.; Athavale, M. M.; Li, H.; Jiang, Y., Mathematical Basis and Validation of the Full Cavitation Model. *Journal of Fluids Engineering* **2002,** *124*, 617.
92. Karrholm, F. P.; Weller, H.; Nordin, N. In *Modelling Injector Flow Including Cavitation Effects for Diesel Applications*, Volume 2: Fora, Parts A and B, ASME: 2007.
93. Koukouvinis, P.; Naseri, H.; Gavaises, M., Performance of turbulence and cavitation models in prediction of incipient and developed cavitation. *International Journal of Engine Research* **2017,** *18* (4), 333-350.
94. Koukouvinis, P.; Gavaises, M. In *Simulation of throttle flow with two phase and single phase homogenous equilibrium model*, Journal of Physics: Conference Series, IOP Publishing: 2015; p 012086.
95. Karathanassis, I.; Trickett, K.; Koukouvinis, P.; Wang, J.; Barbour, R.; Gavaises, M., Illustrating the effect of viscoelastic additives on cavitation and turbulence with X-ray imaging. *Scientific reports* **2018,** *8* (1), 1-15.
96. Karathanassis, I. K.; Koukouvinis, P.; Kontolatis, E.; Lee, Z.; Wang, J.; Mitroglou, N.; Gavaises, M., High-speed visualization of vortical cavitation using synchrotron radiation. *Journal of Fluid Mechanics* **2018,** *838*, 148-164.

97. Brunhart, M.; Soteriou, C.; Daveau, C.; Gavaises, M.; Koukouvinis, P.; Winterbourn, M., Cavitation erosion risk indicators for a thin gap within a diesel fuel pump. *Wear* **2020,** *442*, 203024.
98. Cristofaro, M.; Edelbauer, W.; Koukouvinis, P.; Gavaises, M., Influence of Diesel Fuel Viscosity on Cavitating Throttle Flow Simulations under Erosive Operation Conditions. *ACS omega* **2020,** *5* (13), 7182-7192.
99. Örley, F.; Hickel, S.; Schmidt, S. J.; Adams, N. A., Large-Eddy Simulation of turbulent, cavitating fuel flow inside a 9-hole Diesel injector including needle movement. *International Journal of Engine Research* **2017,** *18* (3), 195-211.
100. Kolev, N., *Multiphase Flow Dynamics 3: Turbulence, Gas Absorption and Release, Diesel Fuel Properties.* Springer Verlag Berlin Heidelberg: 2002.
101. Park, S. H.; Suh, H. K.; Lee, C. S., Effect of Bioethanol-Biodiesel Blending Ratio on Fuel Spray Behavior and Atomization Characteristics. *Energy & Fuels* **2009,** *23*, 4092-4098.
102. Park, S. H.; Kim, S. H.; Lee, C. S., Mixing Stability and Spray Behavior Characteristics of Diesel-Ethanol-Methyl Ester Blended Fuels in a Common-Rail Diesel Injection System. *Energy & Fuels* **2009,** *23*, 5228-5235.
103. Yang, S.; Habchi, C., Real-fluid phase transition in cavitation modeling considering dissolved non-condensable gas. *Physics of Fluids* **2020,** *32* (3), 032102.
104. Toth, S. L., Experimental study of droplet vaporization and combustion of diesel, biodiesel and their blends in a turbulent environment at elevated pressure and temperature conditions. **2014**.
105. Zhang, L.; Kong, S. C., High-pressure vaporization modeling of multi-component petroleum-biofuel mixtures under engine conditions. *Combustion and Flame* **2011,** *158* (9), 1705-1717.
106. Strotos, G.; Gavaises, M.; Theodorakakos, A.; Bergeles, G., Numerical investigation of the evaporation of two-component droplets. *Fuel* **2011,** *90* (4), 1492-1507.
107. Cristofaro, M.; Edelbauer, W.; Koukouvinis, P.; Gavaises, M., A numerical study on the effect of cavitation erosion in a diesel injector. *Applied Mathematical Modelling* **2020,** *78*, 200-216.
108. Caupin, F.; Stroock, A. D., The stability limit and other open questions on water at negative pressure. *Liquid Polymorphism: Advances in Chemical Physics* **2013,** *152*, 51-80.
109. Trevena, D., Cavitation and the generation of tension in liquids. *Journal of Physics D: Applied Physics* **1984,** *17* (11), 2139.
110. Schnerr, G. H.; Sauer, J., Physical and Numerical Modeling of Unsteady Cavitation Dynamics. *Fourth International Conference on Multiphase Flow* **2001,** (May 2001), 1-12.
111. Singhal, A. K.; Athavale, M. M.; Li, H.; Jiang, Y., Mathematical Basis and Validation of the Full Cavitation Model. *Journal of Fluids Engineering* **2002,** *124* (3), 617-617.
112. Zwart, P. J.; Gerber, A. G.; Belamri, T. In *A two-phase flow model for predicting cavitation dynamics*, Fifth international conference on multiphase flow, Yokohama, Japan, 2004.
113. Naseri, H.; Trickett, K.; Mitroglou, N.; Karathanassis, I.; Koukouvinis, P.; Gavaises, M.; Barbour, R.; Diamond, D.; Rogers, S. E.; Santini, M., Turbulence and Cavitation Suppression by Quaternary Ammonium Salt Additives. *Scientific reports* **2018,** *8* (1), 1-15.
114. Dumond, J.; Magagnato, F.; Class, A., Stochastic-field cavitation model. *Physics of Fluids* **2013,** *25* (7), 073302.
115. Wang, C.; Moro, A.; Xue, F.; Wu, X.; Luo, F., The influence of eccentric needle movement on internal flow and injection characteristics of a multi-hole diesel nozzle. *International Journal of Heat and Mass Transfer* **2018,** *117*, 818-834.
116. Nurick, W. H., Orifice Cavitation and Its Effect on Spray Mixing. *Journal of Fluids Engineering* **1976,** *98*, 681.
117. Gavaises, M.; Andriotis, A.; Papoulias, D.; Mitroglou, N.; Theodorakakos, A., Characterization of string cavitation in large-scale Diesel nozzles with tapered holes. *Physics of Fluids* **2009,** *21*, 052107.
118. Mitroglou, N.; McLorn, M.; Gavaises, M.; Soteriou, C.; Winterbourne, M., Instantaneous and ensemble average cavitation structures in Diesel micro-channel flow orifices. *Fuel* **2014,** *116*, 736-742.

119. Mitroglou, N.; Gavaises, M., Mapping of cavitating flow regimes in injectors for medium-/heavy-duty diesel engines. *International Journal of Engine Research* **2013,** *14* (6), 590-605.
120. Mitroglou, N.; Gavaises, M., Cavitation inside Real-Size Fully Transparent Fuel Injector Nozzles and Its Effect on Near-Nozzle Spray Formation. *Proc. ofWorkshop on Droplet Impact Phenomena and Spray Investigations (DIPSI), University of Bergamo, Italy* **2011**.
121. Santos, E. G.; Shi, J.; Gavaises, M.; Soteriou, C.; Winterbourn, M.; Bauer, W., Investigation of cavitation and air entrainment during pilot injection in real-size multi-hole diesel nozzles. *Fuel* **2020,** *263*, 116746.
122. Gold, M.; Pearson, R.; Turner, J.; Sykes, D.; Stetsyuk, V.; De Sercey, G.; Crua, C.; Koukouvinis, F.; Gavaises, M., Simulation and Measurement of Transient Fluid Phenomena within Diesel Injection. *SAE Technical Papers* **2019,** *2019*, 0066.
123. Puduppakkam, K.; Naik, C.; Meeks, E.; Krenn, C.; Kroiss, R.; Gelbmann, J.; Pessl, G. *Predictive combustion and emissions simulations for a high performance diesel engine using a detailed fuel combustion model*; 0148-7191; SAE Technical paper: 2014.
124. Wertheim, M. S., Fluids with highly directional attractive forces. I. Statistical thermodynamics. *Journal of statistical physics* **1984,** *35*, 19-34.
125. Wertheim, M. S., Fluids with highly directional attractive forces. II. Thermodynamic perturbation theory and integral equations. *Journal of statistical physics* **1984,** *35*, 35-47.
126. Wertheim, M. S., Fluids with highly directional attractive forces. III. Multiple attraction sites. *Journal of statistical physics* **1986,** *42*, 459-476.
127. Wertheim, M. S., Fluids with highly directional attractive forces. IV. Equilibrium polymerization. *Journal of statistical physics* **1986,** *42*, 477-492.
128. Lorentz, H., Ueber die Anwendung des Satzes vom Virial in der kinetischen Theorie der Gase. *Annalen der physik* **1881,** *248* (1), 127-136.
129. Tapriyal, D.; Enick, R.; McHugh, M.; Gamwo, I.; Morreale, B., High Temperature , High Pressure Equation of State Density Correlations and Viscosity Correlations. *National Energy Technology Laboratory* **2012,** (July), 1-98.
130. Zúñiga-Hinojosa, M. A.; Justo-García, D. N.; Aquino-Olivos, M. A.; Román-Ramírez, L. A.; García-Sánchez, F., Modeling of asphaltene precipitation from n-alkane diluted heavy oils and bitumens using the PC-SAFT equation of state. *Fluid Phase Equilibria* **2014,** *376*, 210-224.
131. Justo-García, D. N.; García-Sánchez, F.; Romero-Martínez, A. n.; Díaz-Herrera, E.; Juaristi, E. In *Isothermal Multiphase Flash Calculations with the PC-SAFT Equation of State*, 2008; AIP: pp 195-214.
132. Baker, L. E.; Pierce, A. C.; Luks, K. D., Gibbs Energy Analysis of Phase Equilibria. *Society of Petroleum Engineers Journal* **1982,** *22*, 731-742.
133. Fletcher, R., *Practical methods of optimization*. John Wiley & Sons: 2013.
134. Baled, H. O.; Xing, D.; Katz, H.; Tapriyal, D.; Gamwo, I. K.; Soong, Y.; Bamgbade, B. A.; Wu, Y.; Liu, K.; McHugh, M. A.; Enick, R. M., Viscosity of n-hexadecane, n-octadecane and n-eicosane at pressures up to 243 MPa and temperatures up to 534 K. *Journal of Chemical Thermodynamics* **2014,** *72*, 108-116.
135. Lohrenz, J.; Bray, B. G.; Clark, C. R., Calculating viscosities of reservoir fluids from their compositions. *Journal of Petroleum Technology* **1964,** *16* (10), 1,171-1,176.
136. Quiñones-Cisneros, S. E.; Zéberg-Mikkelsen, C. K.; Fernández, J.; García, J., General friction theory viscosity model for the PC-SAFT equation of state. *AIChE Journal* **2006,** *52* (4), 1600-1610.
137. Llovell, F.; Marcos, R. M.; Vega, L. F., Free-volume theory coupled with soft-SAFT for viscosity calculations: Comparison with molecular simulation and experimental data. *Journal of Physical Chemistry B* **2013,** *117* (27), 8159-8171.
138. Yarranton, H.; Satyro, M., Expanded fluid-based viscosity correlation for hydrocarbons. *Industrial & engineering chemistry research* **2009,** *48* (7), 3640-3648.

139. Chung, T. H.; Ajlan, M.; Lee, L. L.; Starling, K. E., Generalized multiparameter correlation for nonpolar and polar fluid transport properties. *Industrial & Engineering Chemistry Research* **1988,** *27* (4), 671-679.
140. Pedersen, K. S.; Fredenslund, A., An improved corresponding states model for the prediction of oil and gas viscosities and thermal conductivities. *Chemical Engineering Science* **1987,** *42* (1), 182-186.
141. Lötgering-Lin, O.; Gross, J., Group Contribution Method for Viscosities Based on Entropy Scaling Using the Perturbed-Chain Polar Statistical Associating Fluid Theory. *Industrial and Engineering Chemistry Research* **2015,** *54* (32), 7942-7952.
142. Rosenfeld, Y., Relation between the transport coefficients and the internal entropy of simple systems. *Physical Review A* **1977,** *15*, 2545.
143. Chapman, S.; Cowling, T. G.; Burnett, D., *The mathematical theory of non-uniform gases: an account of the kinetic theory of viscosity, thermal conduction and diffusion in gases*. Cambridge university press: 1990.
144. Sauer, E.; Stavrou, M.; Gross, J., Comparison between a Homo- and a Heterosegmented Group Contribution Approach Based on the Perturbed-Chain Polar Statistical Associating Fluid Theory Equation of State. *Industrial & Engineering Chemistry Research* **2014,** *53* (38), 14854-14864.
145. Novak, L. T., Predicting natural gas viscosity with a mixture viscosity model for the entire fluid region. *Industrial & Engineering Chemistry Research* **2013,** *52*, 16014–16018.
146. Grunberg, L.; Nissan, A. H., Mixture law for viscosity. *Nature* **1949,** *164* (4175), 799-800.
147. Novak, L. T., Predicting Natural Gas Viscosity with a Mixture Viscosity Model for the Entire Fluid Region. *Industrial & Engineering Chemistry Research* **2013,** *52* (45), 16014-16018.
148. Liang, X.; Yan, W.; Thomsen, K.; Kontogeorgis, G. M., On petroleum fluid characterization with the PC-SAFT equation of state. *Fluid Phase Equilibria* **2014,** *375*, 254–268.
149. Burgess, W. A.; Tapriyal, D.; Morreale, B. D.; Soong, Y.; Baled, H. O.; Enick, R. M.; Wu, Y.; Bamgbade, B. A.; McHugh, M. A., Volume-translated cubic EoS and PC-SAFT density models and a free volume-based viscosity model for hydrocarbons at extreme temperature and pressure conditions. *Fluid Phase Equilibria* **2013,** *359*, 38-44.
150. Nocedal, J.; Wright, S., *Numerical Optimization*. Springer New York: 2006.
151. Mikyška, J.; Firoozabadi, A., Investigation of mixture stability at given volume, temperature, and number of moles. *Fluid Phase Equilibria* **2012,** *321*, 1-9.
152. Nichita, D. V., Fast and robust phase stability testing at isothermal-isochoric conditions. *Fluid Phase Equilibria* **2017,** *447*, 107-124.
153. Wilson, G. M. In *A modified Redlich-Kwong equation of state, application to general physical data calculations*, 65th National AIChE Meeting, Cleveland, OH, 1969; p 15.
154. Privat, R.; Gani, R.; Jaubert, J. N., Are safe results obtained when the PC-SAFT equation of state is applied to ordinary pure chemicals? *Fluid Phase Equilibria* **2010**, 76-92.
155. Press, W. H.; Flannery, B. P.; Teukolsky, S. A.; Vetterling, W. T.; Gould, H., Numerical Recipes, The Art of Scientific Computing. *American Journal of Physics* **1987,** *55*, 90-91.
156. Dahms, R. N.; Manin, J.; Pickett, L. M.; Oefelein, J. C., Understanding high-pressure gas-liquid interface phenomena in Diesel engines. *Proceedings of the Combustion Institute* **2013,** *34*, 1667-1675.
157. Mueller, C. J.; Cannella, W. J.; Bays, J. T.; Bruno, T. J.; DeFabio, K.; Dettman, H. D.; Gieleciak, R. M.; Huber, M. L.; Kweon, C.-B.; McConnell, S. S., Diesel surrogate fuels for engine testing and chemical-kinetic modeling: Compositions and properties. *Energy & Fuels* **2016,** *30*, 1445-1461.
158. Yarborough, L., Vapor-liquid equilibrium data for multicomponent mixtures containing hydrocarbon and nonhydrocarbon components. *Journal of Chemical & Engineering Data* **1972,** *17*, 129-133.
159. Kuenen, J. P., On Retrograde Condensation and the Critical Phenomena of Two Substances. *Commun. Phys. Lab U. Leiden* **1892**.

160. Liang, X., On the efficiency of PT Flash calculations with equations of state. *Computer Aided Chemical Engineering* **2018**, 859-864.
161. Chu, T.-C.; Chen, R. J. J.; Chappelear, P. S.; Kobayashi, R., Vapor-liquid equilibrium of methane-n-pentane system at low temperatures and high pressures. *Journal of Chemical & Engineering Data* **1976,** *21*, 41-44.
162. Garcia-Cordova, T.; Justo-Garcia, D. N.; Garcia-Flores, B. E.; Garcia-Sanchez, F., Vapor-Liquid Equilibrium Data for the Nitrogen - Dodecane System at Temperatures from (344 to 593) K and at Pressures up to 60 MPa. *Journal of Chemical & Engineering Data* **2011,** *56*, 1555-1564.
163. Gross, J.; Sadowski, G., Application of the perturbed-chain SAFT equation of state to associating systems. *Industrial and Engineering Chemistry Research* **2002**, 5510-5515.
164. Gross, J.; Vrabec, J., An equation-of-state contribution for polar components: Dipolar molecules. *AIChE Journal* **2006**, 1194-1204.
165. Gross, J., An equation-of-state contribution for polar components: Quadrupolar moleculesc. *AIChE Journal* **2005**, 2556-2568.
166. Shahriari, R.; Dehghani, M. R.; Behzadi, B., Thermodynamic modeling of aqueous ionic liquid solutions using PC-SAFT equation of state. *Industrial and Engineering Chemistry Research* **2012**, 10274-10282.
167. *OpenFOAM*, v2.4.
168. Koukouvinis, P.; Gavaises, M.; Supponen, O.; Farhat, M., Simulation of bubble expansion and collapse in the vicinity of a free surface. *Physics of Fluids* **2016,** *28* (5), 052103.
169. Payri, R.; Tormos, B.; Gimeno, J.; Bracho, G., The potential of Large Eddy Simulation (LES) code for the modeling of flow in diesel injectors. *Mathematical and Computer Modelling* **2010,** *52* (7-8), 1151-1160.
170. Nicoud, F.; Ducros, F., Subgrid-scale stress modelling based on the square of the velocity gradient tensor. *Flow, turbulence and Combustion* **1999,** *62* (3), 183-200.
171. Zhang, L.; He, Z.; Guan, W.; Wang, Q.; Som, S., Simulations on the cavitating flow and corresponding risk of erosion in diesel injector nozzles with double array holes. *International Journal of Heat and Mass Transfer* **2018,** *124*, 900-911.
172. Koukouvinis, P.; Gavaises, M.; Li, J.; Wang, L., Large Eddy Simulation of Diesel injector including cavitation effects and correlation to erosion damage. *Fuel* **2016,** *175*, 26-39.
173. Brusiani, F.; Falfari, S.; Pelloni, P., Influence of the Diesel injector hole geometry on the flow conditions emerging from the nozzle. *Energy Procedia* **2014,** *45*, 749-758.
174. Reid, B. A.; Hargrave, G. K.; Garner, C. P.; Wigley, G., An investigation of string cavitation in a true-scale fuel injector flow geometry at high pressure. *Physics of Fluids* **2010,** *22* (3), 031703.
175. Gross, J.; Sadowski, G., Perturbed-Chain SAFT: An Equation of State Based on a Perturbation Theory for Chain Molecules. *Industrial & Engineering Chemistry Research* **2001,** *40* (4), 1244-1260.
176. Kedrinskiy, V. K., *Hydrodynamics of Explosion: experiments and models*. Springer Science & Business Media: 2006.
177. Saurel, R.; Petitpas, F.; Abgrall, R., Modelling phase transition in metastable liquids: application to cavitating and flashing flows. *Journal of Fluid Mechanics* **2008,** *607*, 313-350.
178. Beattie, D.; Whalley, P., A simple two-phase frictional pressure drop calculation method. *International Journal of Multiphase Flow* **1982,** *8* (1), 83-87.
179. Hopp, M.; Gross, J., Thermal Conductivity of Real Substances from Excess Entropy Scaling Using PCP-SAFT. *Industrial and Engineering Chemistry Research* **2017,** *56* (15), 4527-4538.
180. Fortes Patella, R.; Choffat, T.; Reboud, J. L.; Archer, A., Mass loss simulation in cavitation erosion: Fatigue criterion approach. *Wear* **2013,** *300* (1-2), 205-215.
181. Brennen, C. E., *Cavitation and bubble dynamics*. 2013; p 1-249.